©Copyright 2025
Koshiro Yamaguchi

Reconfigurability, Tunability, and Controllability of Origami-based Mechanical Metamaterials

Koshiro Yamaguchi

A dissertation
submitted in partial fulfillment of the
requirements for the degree of

Doctor of Philosophy

University of Washington

2025

Reading Committee:

Marco Salviato, Chair

Jinkyu Yang

Ed Habtour

Mehran Masbahi

Program Authorized to Offer Degree:

Aeronautics & Astronautics

University of Washington

Abstract

Reconfigurability, Tunability, and Controllability of Origami-based Mechanical Metamaterials

Koshiro Yamaguchi

Chair of the Supervisory Committee:
Marco Salviato
Aeronautics & Astronautics

Mechanical metamaterials, materials with architecture-driven properties, hold promise for applications ranging from aerospace components to soft robotic devices. Yet these engineered structures often face challenges in practical applications due to costly fabrication and fixed, non-adjustable properties once made. Origami-inspired design offers a path to overcome these limitations: by folding flexible architectures, metamaterials can gain reconfigurability and tunable behavior. In this dissertation, we introduce technical approaches for assessing reconfigurability, tunability, and controllability of origami-based mechanical metamaterials, focusing on Tachi–Miura Polyhedron (TMP) and Miura-ori patterns as model systems. Our goal is to advance these metamaterials toward the vision of highly reconfigurable origami-based mechanical metamaterials; materials that can be reshaped or repurposed on demand.

To navigate the enormous design space of origami metamaterials, we develop a graph-based algorithm that systematically generates all geometrically valid TMP configurations. This approach avoids the combinatorial explosion that hampers brute-force searches, running roughly 20–100 times faster and enabling the analysis of much larger systems. By mapping the full range of configurations, our method also reveals highly heterogeneous, non-intuitive designs that would be impractical to discover otherwise.

Next, we demonstrate a post-fabrication programming technique to fine-tune the meta-

material's mechanical properties. By heating the TMP-based structures in a controlled manner, we reconfigure their internal folding geometry (zero-energy state) and achieve dramatic changes in stiffness and density. This thermomechanical tuning method increased the effective Young's modulus by approximately 60-fold and reduced the material's density by tenfold in experiments. Interestingly, we observed an unusual inverse correlation between stiffness and density, a beneficial trait for lightweight materials, and showed that Poisson's ratio can be adjusted from negative (auxetic) to positive values.

We also tackle the challenge of investigating the controllability of these compliant structures for deployment. Using a state-space model of a Miura-ori origami array, we analyze the system's controllability to determine where actuators should be placed for the most effective shape change. The optimal actuation scheme predicted by our model was validated experimentally, yielding a fourfold increase in deployment efficiency compared to the least effective actuator configuration. This result demonstrates that even highly flexible metamaterials can be efficiently deployed through intelligent control strategies.

Together, these advances establish a foundation for origami metamaterials that can be efficiently designed, adjusted on demand, and actively controlled as needed. By bridging geometric design, material tuning, and dynamic actuation, this work paves the way toward intelligent, adaptive origami-based structures with potential applications from aerospace and robotics to biomedical engineering.

TABLE OF CONTENTS

LIST OF FIGURES

LIST OF TABLES

ACKNOWLEDGMENTS

First, I would like to express my deepest gratitude to my advisor, Professor Jinkyu Yang, for his continuous guidance, support, and encouragement throughout my Ph.D. journey. His insightful ideas, high expectations, and patience have shaped both this dissertation and my approach to research and engineering. I am also sincerely grateful to the members of my doctoral committee, Professor Marco Salviato, Professor Mehran Mesbahi, Professor Ed Habtour, and Professor Jeffery Lipton, for their valuable feedback and thoughtful discussions. Their comments and suggestions greatly improved the quality and clarity of this work. I also thank Professor Hiromi Yasuda from the Japan Aerospace Exploration Agency for his mentorship in the early years of my graduate career. His guidance and example had a significant impact on how I think about research and scientific curiosity.

I would like to thank my colleagues and friends in the Department of Aeronautics & Astronautics at the University of Washington, as well as members of our research group, for the many discussions, experiments, and moments of support we shared.

Finally, I would like to thank my colleagues and mentors at Dassault Systèmes for their understanding and support while I was completing this dissertation in parallel with starting my professional career. Their flexibility and encouragement made balancing these responsibilities possible.

DEDICATION

To my family.

Chapter 1

INTRODUCTION

1.1 Background

Mechanical metamaterials offer unprecedented mechanical properties and rich functionalities due to the plentiful design freedom available within their architecture [1, 2, 3, 4]. Unlike conventional materials, which derive their mechanical characteristics from their constituent chemistry, metamaterials leverage carefully engineered geometry, often in the form of periodically arranged building blocks, to exhibit functionalities that are not found in nature. Among a variety of approaches to constructing metamaterials with such unique properties, lattice-based mechanical metamaterials are emerging concepts [5, 6, 7]. Their voluminous nature and extreme mechanical properties have the possibility to work as three-dimensional constructional elements of the mechanical system while achieving superior performance compared to conventional materials. Examples include metamaterials with negative elastic constant [5], labyrinthine acoustic metamaterials to slow down sound propagation [6], and 3D-printed lattices with both lightness and stiffness in an extreme range [7].

While their unique properties can be leveraged in multiple fields, such as mechanical, aerospace, and biomedical engineering, these metamaterials have challenges in terms of the cost of manufacturing and post-fabrication reconfigurability and tunability due to their complicated and unadjustable architecture. To overcome these challenges, various designs have been introduced in the realm of flexible mechanical metamaterials [8]. By embedding kinematic principles into a material's structure, the material's low-energy deformation pathways can be precisely controlled, allowing its macroscopic shape to follow the motion of the underlying mechanism. Examples include programmable flexible mechanical metamaterials with adjustable Poisson's ratio, Young's modulus, or negative thermal expansion coefficient

[9, 10, 11, 12], and shape-changing prismatic architected materials [13].

Origami, a type of art that involves folding a sheet of paper into various forms, has been contributing to this emerging platform to add the tunability of its shapes and mechanical properties [13, 14, 15, 16, 17, 18, 19]. Historically, the origami technique has been applied to space engineering [20, 21, 22], flexible medical stents [23], and flexible electronic devices [24] due to its space-saving nature in the folded state, which is highly beneficial to storing a large structure in a limited storage space. Recently, an extensive amount of research on origami-based metamaterials has been conducted to show their various characteristics in both mathematical and mechanical aspects [25, 26, 27, 28, 29, 30]. For example, they exhibit a versatile mechanical nature, such as a wide range of tunability in terms of their deployed surface area and cross-section [16, 20, 31, 32], Poisson's ratio [33], and stiffness [16, 34].

In recent years, the principles of origami have been extended to the realm of robotics, offering a transformative approach that decouples manufacturing complexity from design complexity [35]. This paradigm, which creates functional and reconfigurable three-dimensional structures by folding a single two-dimensional sheet, provides a physical pathway toward the ultimate goal of highly reconfigurable origami-based mechanical metamaterials; a material whose shape and stiffness can be programmed in response to external commands [36]. Spurred by advances in smart materials and fabrication, origami robotics has demonstrated its potential across diverse fields. For example, the scalability of origami and its compatibility with biocompatible materials have enabled devices for minimally invasive surgery [37] and ingestible robots that perform tasks like drug delivery or wound patching inside the body [38]. Furthermore, in the domain of soft robotics, it has produced robotic arms that mimic the complex, multi-degree-of-freedom motions of an octopus—including stretching, omnidirectional bending, and twisting—and "metamorphic robots" that gain new functionalities such as walking, rolling, and gliding [37, 39, 40, 41, 42]. These advanced examples point toward a trend moving beyond simple shape-changing to the integration of sensing, computation, and actuation into compliant materials for autonomous interaction with the environment. This rapid evolution brings to the forefront new challenges in the systematic

design and dynamic control of these complex systems, the very challenges this dissertation aims to address.

1.2 Purpose of this thesis

As outlined in the previous section, the principles of origami offer a promising avenue for designing metamaterials with tunable shapes and mechanical properties. However, to fully unlock their potential and realize the ultimate goal of achieving highly reconfigurable origami-based mechanical metamaterials, it is essential to establish a technical approach that integrates the aspects of design, post-fabrication adaptability, and dynamic control, which have largely been studied separately. Existing research tends to focus on these individual facets, lacking a holistic approach that unifies the field. This dissertation aims to establish such technical approaches by directly addressing three fundamental challenges that impede the realization of intelligent and adaptive material systems.

While most of the previous research works focus on the homogeneous arrangements of origami units and their intrinsic properties, the cross-linkage of heterogeneous origami cells and their effective global characteristics have been relatively unexplored. To fully explore the rich design space that origami-based metamaterials offer systematically, it is essential to address the heterogeneity and combinatorial problems of them. To overcome this problem, the combination of Tachi-Miura Polyhedron (TMP) and graph theory can serve as an ideal platform [17, 43, 44]. TMP is one of the origami-based mechanical metamaterials with bellow-like 3D unit cells constructed from 2D Miura-folding sheets. This TMP-based metamaterial features several mechanical characteristics, such as flat and rigid foldability, negative Poisson's ratio, multistability, and load-bearing capabilities. Graph theory is a field in discrete mathematics, which is used to represent pairwise relations between objects [45]. In this mathematical schematization, the objects are referred to as vertices, and the connected pairs of the objects are called edges. In diagrammatic ways, graphs are often represented with dots (or circles) for vertices and lines for edges. Generally, graphs are classified into two types: undirected graphs and directed graphs. The former have edges without direction (two-way

relationships), whereas the latter have edges with direction (one-way relationships). This simple-yet-efficient mathematical structure can be utilized to model various types of connections in general. Therefore, it has been applied to numerous systems, such as physical [46], biological [47], and information [48] ones.

Second, to tackle the issues of tunability and manufacturability, we aim to develop an engineering platform with the following features: (i) extensive and continuous design space, and post-fabrication tunability for three key mechanical properties — effective density, Poisson's ratio, and Young's modulus, (ii) the ability to easily predict these properties through analytical methods, and (iii) an efficient and straightforward fabrication of multi-cell 3D structures by simply joining layers, eliminating the need for cell-by-cell assembly. Specifically, to address the limitation of fixed post-fabrication properties, a thermomechanical treatment method is introduced for in-situ tuning of the metamaterial's static mechanical response. Through controlled heat processing of TMP structures, the material's zero-energy state is programmed, allowing for significant post-fabrication adjustments. Experimental validation demonstrates a remarkable tuning range, achieving an approximately 60-fold change in Young's modulus and a 10-fold change in effective density, while also revealing a unique and desirable inverse correlation between stiffness and density.

Third, despite the fast and rich advancement of origami robotics, understanding their transient dynamics and constructing control models remains a formidable task, primarily due to their innate flexibility stemming from their soft-bodied composition. To explore the dynamics of origami structures, several model-based and data-driven methods are proposed. For example, finite element model [49], bar-and-hinge model [30], deep learning [50], reservoir computing [51], and dynamic mode decomposition [52] are the notable ones. However, while these works focus on predicting and computing the dynamics of origami structures, the control method of origami is rather unexplored. Thus, to achieve precise control of the origami structures, we try to bridge the gap between the dynamics of origami and control theory. To this end, we propose a state-space representation of origami dynamics based on the bar-and-hinge model. The bar-and-hinge model is a reduced-order model to represent

the mechanics of origami structure [53, 54]. Unlike the finite element models, the bar-and-hinge model is computationally efficient and provides us with closed-form equations of the dynamics regarding particle masses. Based on the bar-and-hinge model, we can describe the dynamical system with a state-space representation. State-space representation is a mathematical technique for modeling a physical system with a combination of input, output, and variables correlated by first-order differential equations. By utilizing the state-space representation, we can obtain controllability, an important control characteristics of the system [55].

1.3 Organization of this thesis

The current dissertation is organized as follows: in Chapter 2, we investigate the reconfigurability of a tessellation of origami-based cellular structures composed of bellows-like unit cells, specifically the Tachi-Miura Polyhedron (TMP). One of the unique features of the TMP is that a single cell can take four different phases in a rigid-foldable manner. Therefore, the TMP tessellation can achieve various shapes out of one original assembly. To assess the geometrical validity of the astronomical number of origami phase combinations, we build a graph-theoretical framework to describe the connectivity of unit cells and to analyze the reconfigurability of the tessellations.

In Chapter 3, we investigate the reconfigurability and tunability of the tessellation of TMP. We utilize TMP's highly versatile phase-transforming and tessellating capabilities to design reconfigurable metamaterial architecture with tunable mechanical properties. The theoretical analyses and experiments with heat processing discover the wide range of the in-situ tunability of the metamaterial – specifically orders of magnitude change in effective density, Young's modulus, and Poisson's ratio – after its fabrication within the elastic deformation regime. We also witness a rather unique behavior of the inverse correlation between effective density and stiffness.

In Chapter 4, we investigate the controllability of an origami system composed of Miura-ori cells. We discretize the origami system into a network composed of interconnected particle

masses alongside bar and hinge elements. This yields a state-space representation of the system's dynamics, enabling us to obtain the system's controllability attributes. Informed by this computational framework, we explore strategies for finding the most efficient crease line for deployment with an actuator, both theoretically and experimentally. Lastly, in Chapter 5, we summarize the findings of the research presented in this dissertation and discuss an outlook on potential future directions.

Chapter 2

GRAPH-THEORETIC ESTIMATION OF RECONFIGURABILITY IN ORIGAMI-BASED METAMATERIALS

In this chapter, we address the combinatorial challenge of determining all valid geometric configurations in reconfigurable origami-based metamaterials, focusing on tessellations of Tachi-Miura Polyhedron (TMP) unit cells, each capable of assuming four distinct phases. To overcome the computational intractability of a brute-force search for large systems, we developed a graph-theoretical framework that represents the physical connectivity of the unit cells using graphs and adjacency matrices. This approach enables an efficient and systematic enumeration of all geometrically valid configurations, proving to be 20 to 100 times faster than conventional methods, and reveals an exponential growth in reconfigurability with the number of cells. Our primary contribution is a versatile computational methodology that serves as a systematic design tool for creating advanced mechanical metamaterials with tailored, highly heterogeneous properties. This establishes a foundation for designing complex, reconfigurable architected materials for diverse engineering applications, such as space engineering, where the flat-foldability is important [20] and biomechanical engineering, where the combination of positive and negative Poissonś ratio and a wide range of mechanical tunability are required [56]. This computational framework can also be applied to the various mechanical metamaterials to unlock their full potential [13, 14, 16, 28, 31, 57, 58].

2.1 TMP tessellation and its transformation

It is well known that TMP can take finite volume or be collapsed to zero volume during its folding process [44] (see “TMP” and “flat” state in Fig. 2.1). In this study, we also consider

two other geometries, so-called origami tube minus and origami tube plus, which can be generated from the flat state without deviating from the rigid-foldable assumption. Thus, in this study, we consider four possible states of unit cells: TMP, OT−, OT+, and Defect. Here, defect mode means the flat state, which does not occupy any volume.

Fig. 2.1(a) explains the components of TMPs with geometrical parameters (l, m, d, α). In Fig. 2.1(b), we see that the folding angle of blue and green creases decides the reconfigurable states of a unit cell. If blue (green) creases are folded flat, unit cells become OT+ (OT−). Fig. 2.1(c) shows the transition of the unit cell from the flat state to four reconfigurable states of TMP, OT+, OT−, and Defect. Fig. 2.1(d) and (e) depict those states and transformations between them for the 3D-rendered model and paper prototype, respectively.

The TMP cells can further be assembled into a tessellation in both horizontal and vertical manner as shown in Fig. 2.2(a), and it can have multiple cells with different states. For example, Figs. 2.2(b) and (c) show some exemplary configurations of the 3-by-3 tessellation in the 3D-rendered graphics and the corresponding paper prototype images. Here, TMP, OT−, and OT+ are represented by gray, blue, and red colors, respectively. By including the defect mode, we have four different states that can be assigned for each unit. Therefore, we can consider 4^n patterns of configurations within a n-cell tessellation. However, there exists a kinematic relationship between the adjoined TMP cells, and a large portion of the 4^n patterns are not valid. Fig. 2.3 illustrates this problem by using two-cell and three-cell tessellations. By simulating the stacking of unit cells, we can tell that some configurations are invalid due to the unmatching of the geometrical boundaries of the unit cells.

While we can achieve various shapes with this reconfigurable origami tessellation, it is hard to know the actual number of total configurations within a given size of tessellation. Considering all cases (e.g., $4^9 = 262{,}144$ for 3-by-3 TMP tessellations) and sorting out what are valid configurations one by one is computationally expensive and even impossible for a large tessellation using conventional computational power. To overcome this hurdle, we introduce the idea of a graph-theoretical framework to discover the possible configuration efficiently. With the aid of the graph representation of a reconfigurable origami tessellation

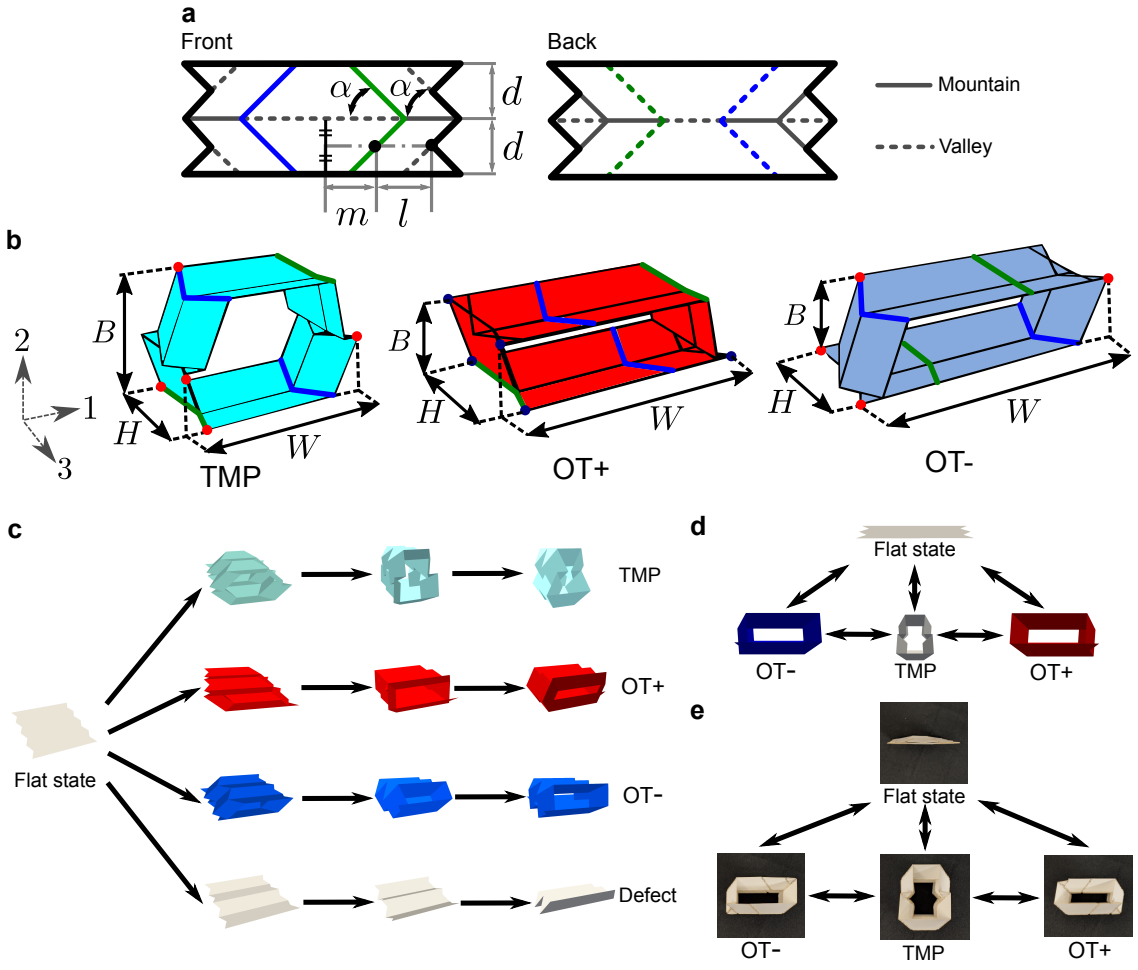

Figure 2.1: Folding behavior of a single Tachi-Miura Polyhedron (TMP) unit cell. **a**, crease patterns and geometrical parameters of two flat sheets composing the TMP. **b**, the folding angles of blue and green creases decide the reconfigurable states of a unit cell. When blue (green) creases are folded flat, the unit cell takes the OT+ (OT−) phase. Dimensions B, W, and H correspond to the width, breadth, and height of the structure, respectively. Also, axis numbers 1, 2, and 3 have the same direction as width, breadth, and height, respectively. **c**, 3D rendered images of the transition from the flat state to four reconfigurable states. **d**, 3D rendered images of a TMP unit cell with the initial flat state and the three reconfigurable states of TMP, OT+, and OT−. **e**, images of paper prototypes with corresponding configurations to **d**.

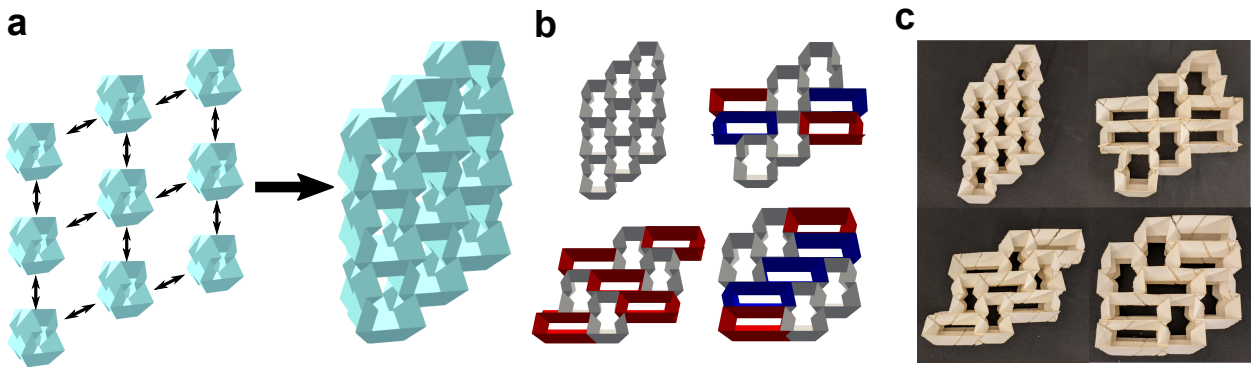

Figure 2.2: Connectivity of a 3-by-3 TMP tessellation and examples of its various configurations. **a**, 3D rendered images showing how a tessellation is built with the nine unit cells. Certain faces of unit cells are adjoined altogether to form one tessellation. **b**, 3D rendered images of the 3-by-3 tessellation with four different configurations. **c**, digital images of the paper prototypes corresponding to the four tessellations shown in **b**.

and adjacency matrix obtained from the graph information, we are able to calculate the total number of valid configurations systematically. In the following sections, we introduce the graph representation and adjacency matrices to assess the combinatorial problem of the TMPs.

2.2 Graph representation of TMP tessellation

Recently, several researchers have tackled tessellation-related problems for materials sciences with the aid of graph-theoretic techniques. Arkus et al. utilized graph-theoretic enumerations of adjacency matrices and distance matrices to find the finite sphere packings [59]. Vlassis et al. applied graphs and graph convolutional deep neural network for anisotropic hyperelasticity of polycrystal materials [60]. Herein, we further leverage this technology to investigate the reconfigurability of origami tessellations.

As a first step, we attempt to translate physical TMP tessellations to graph representations. This idea of extracting characteristic points from the geometry of an origami structure

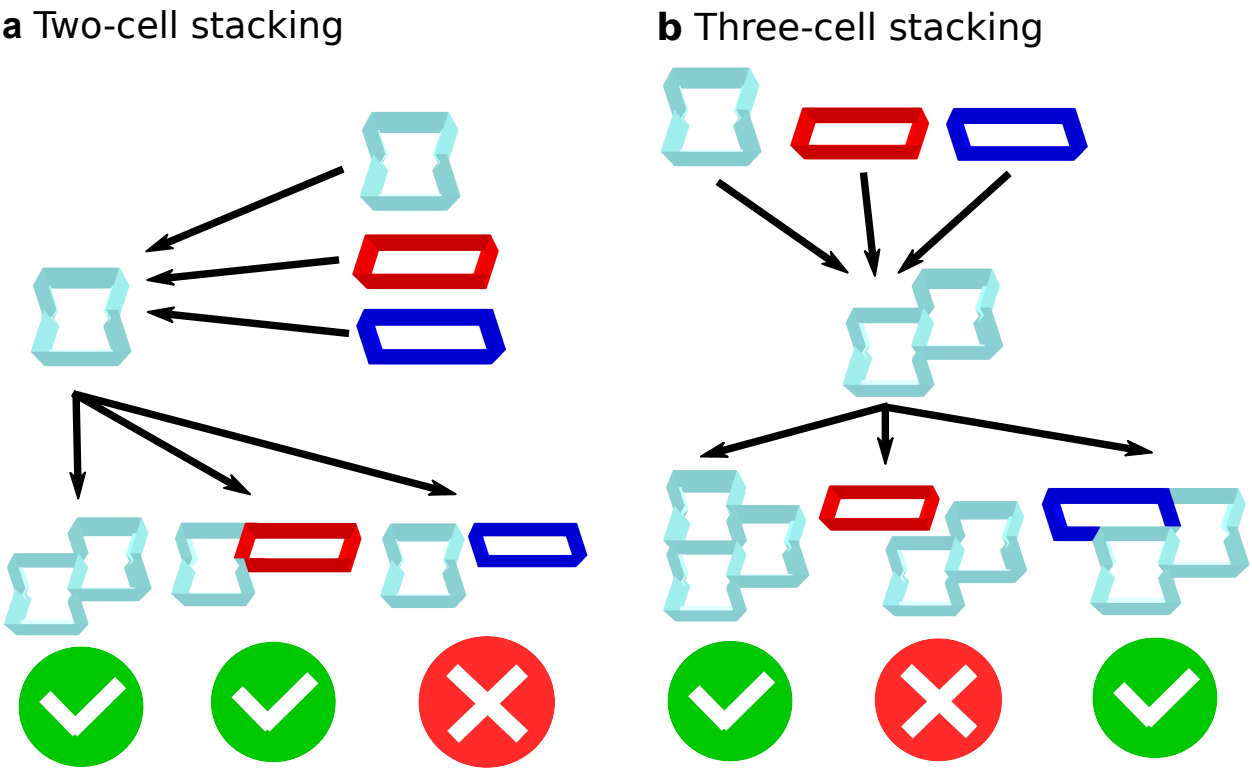

Figure 2.3: Geometrical validity check of the TMP tessellation. Cases of **a**, two-cell tessellations and **b**, three-cell tessellations. In **a**, one unit cell (TMP, OT+, or OT−) is attached to one TMP cell. The attachment of TMP and OT+ results in a valid configuration. However, we can see that the OT− tube does not fit with the upper-right side of the TMP cell. Likewise, cases of three-cell stacking in **b** show that the attachment of TMP and OT− to a two-TMP stacking brings the valid configuration, whereas the attachment of OT+ tube makes the tessellation invalid.

has been previously reported [61]. This simplification of origami-based metamaterials into the lattices of characteristic points shows a great advantage to understand and analyze origami-based metamaterials. Here, we utilize a similar process to schematize TMP tessellations as graph structures. Figs. 2.4(a) and (b) show how we define an undirected graph $G = (V, E)$ from a single unit cell and a tessellation, respectively. Here, vertices V represent the six major faces of a unit cell, and the edge set E consists of unordered pairs of vertices. The number of vertices is $|V| = 6n$, where n is the number of unit cells in a tessellation. The edge set counts the connections of faces both within one unit cell and between neighboring cells (see dashed and solid lines in Fig. 2.4). Then, we also define a subgraph $G' = (V', E')$ such that $V' \subseteq V$ and $E' \subseteq E$, where V' and E' represents the interconnections among the unit cells. For example, in Fig. 2.4(b) where we consider a 2 by 2 tessellation, we have $V' = \{1, 2, 7, 11, 12, 14, 15, 16, 22, 23\}$ and $E' = \{(1, 16), (2, 11), (7, 22), (12, 15), (14, 23)\}$.

Based on this graph representation, we utilize graph-theoretic enumeration of adjacency matrices. We introduce those definitions in the following. A tessellation of n unit cells can be described by an $|V| \times |V|$ adjacency matrix $\boldsymbol{A}$. This matrix is defined with the graph G and the subgraph G'. Therefore it details which vertices (faces in physical unit cells) are in contact: $\boldsymbol{A}_{ij} = 1$ if and only if $(u_i, u_j) \in E'$ and otherwise $\boldsymbol{A}_{ij} = 0$. This means that $\boldsymbol{A}_{ij} = 1$ if ith and jth faces are attached to each other, and $\boldsymbol{A}_{ij} = 0$ if they are not. It should be noted that each x-by-y tessellation has only one unique adjacency matrix – regardless of the phases of unit cells – because once we define the size of the tessellation and its arrangement, we also know which physical faces of unit cells to be connected to others. The illustration of the adjacency matrix is also shown in Fig. 2.4(b). Here, the dots denote the edge set E', which represents the adjoining of TMP faces.

2.3 Combinatorial search for valid configurations

To analyze the reconfigurability of the TMP tessellations, we utilize the aforementioned graph representation and algorithm. The reconfigurability can be quantified by the number of unique configurations that the tessellation can achieve. The search of valid configurations

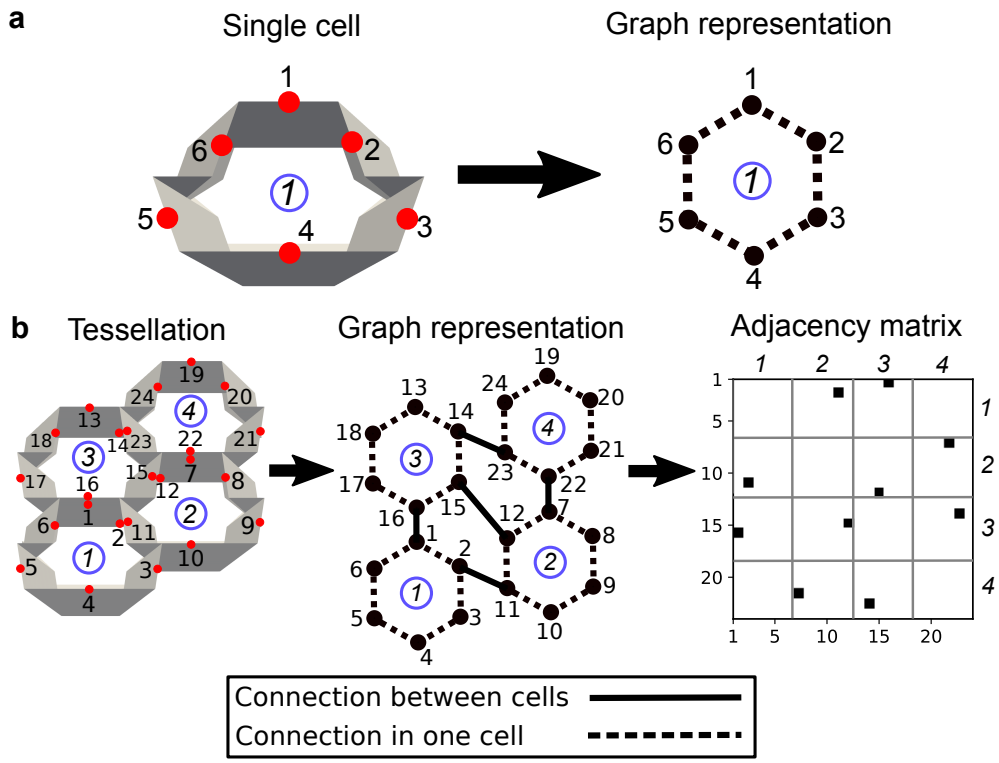

Figure 2.4: Examples of the graph representation for **a**, a single unit cell and **b**, a 2-by-2 tessellation. Red dots in **a** and **b** represent the midpoints of the major side edges of TMPs (adjacent red dots in **b** are actually overlapping). In a graph representation, those red dots are considered as nodes. Dashed lines in **a** and **b** mean the connection of the nodes within a unit cell. Solid lines in **b** mean the connection of the nodes between different unit cells. Italic numbers in blue circles denote the TMP unit cells, and upright numbers denote the middle points in physical TMPs and the corresponding nodes in the graph. In the illustration of the adjacency matrix, the left and bottom labels show the node numbers as represented in the graph. Likewise, right and top labels in italic numbers denote the TMP unit cells. Gray lines in the adjacency matrix show which part of the matrix corresponds to the TMP unit cell numbers. Dots in this adjacency matrix indicate the connected nodes, i.e., adjoined faces in the TMP tessellation.

consists of three steps: (i) definition of the size of tessellation, (ii) graph representation and graph-theoretic enumeration of the tessellation, and (iii) combinatorial search for valid configurations. First, we define the size and shape of the tessellation. Our graph-theoretic method is versatile and applicable to various types of tessellations. However, in order to make comparisons and measure the effectiveness of the unit cell number on the reconfigurability, we use a rectangular arrangement of X-by-Y tessellation, where X and Y are the number of unit cells in horizontal and vertical directions, respectively.

Secondly, we represent the tessellation via a graph and enumerate the information about the connection of the unit cells using an adjacency matrix. Again, the adjacency matrix is unique for each tessellation and immutable in the process of tessellation search. After establishing the information about tessellations, we move to the final step, which is the combinatorial search for valid configurations. In this step, we utilize the complete list of 3-cell configurations that are known a priori. It has 32 configurations as shown in Fig. 2.7, and we combine those 3-cell configurations to find configurations of larger tessellations.

The schematic illustration of the process of this combinatorial search is shown in Fig. 2.5. The top row shows the graphical evolution of the TMP tessellation, the middle row shows their graph representation, and the bottom panel explains how we use adjacency matrices for this search process. Italic numbers with red boxes show that unit cells have assignments of configurations, whereas italic numbers with no boxes show that those unit cells do not have assignments yet. By using this assignment information and adjacency matrix, we detect an unassigned unit cell that is adjacent to the assigned ones. Blue arrows and boxes in the matrix show the process of searching for an adjacent unit cell to assign. To begin the search, we allocate configurations to the three cells at the lower-left end. Then, based on the graph structure, we find an adjacent cell and assign a configuration to the adjacent one by looking up the list of the 3-cell configurations (see gray triangles in Fig. 2.5b). We repeat this process until all unit cells have configurations. Also, in this process, we check every one of the configurations in the list. Therefore, at the end of the process, we can count all valid configurations out of a given size of tessellation.

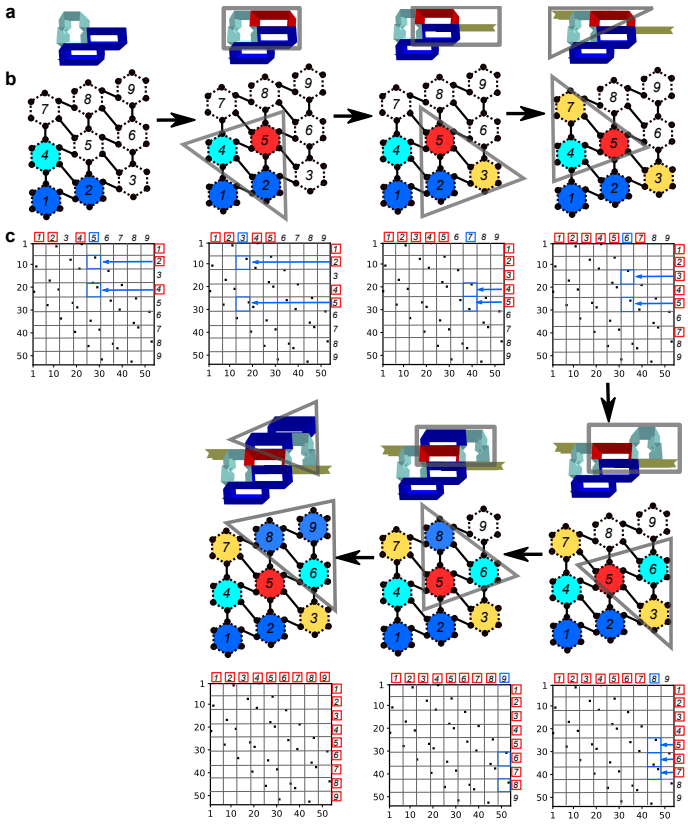

Figure 2.5: An example of discovering a valid configuration for the 3-by-3 tessellation with logistic illustrations of the computation processes using adjacency matrices. In **a** and **b**, cyan, red, blue, and yellow colors in the graph representation correspond to the TMP, OT+, OT−, and defect states of the unit cell, respectively. In **a**, 3d-rendered images represent the graphical process of building tessellations. Likewise, in **b**, the pictures of graphs with colored parts show the schematic process of the tessellation search. Three unit cells enclosed by gray lines in **a** and **b** indicate where the 3-cell configurations are referenced and adopted. In **c**, adjacency matrices are illustrated in the same way as Fig. 2.4(b). Italic numbers with red boxes show that unit cells have assignments of configurations, whereas italic numbers with no boxes show that those unit cells do not have assignments yet. Blue arrows and boxes in the matrix show the process of searching an adjacent unit cell to assign the proper unit cell configuration.

2.4 TMP configurations search via a brute-force method

In order to verify the result from our graph-theoretical method, we implement a brute-force method for smaller sizes of tessellations. Here, we examine the geometrical information of all 4^n candidates of configurations where n is the number of unit cells in a tessellation. In addition to the adjacency matrix we described in the previous section, we utilize the distance matrix to contain the information about geometry of the tessellation and to understand how the faces of the TMPs are attached to each other.

A distance matrix is a nonnegative, square, and symmetric matrix with elements corresponding to pairwise distance between the elements in a set. While several metrics can be used to build such matrix, here we refer Euclidean distance matrices as distance matrices. Here, the distance matrix is a $|V| \times |V|$ matrix $\boldsymbol{D}$, where $\boldsymbol{D}_{ij}$ is the element of $\boldsymbol{D}$. Consider a collection of $|V|$ points in a d-dimensional Euclidean space, assigned to the columns of matrix $\boldsymbol{X} \in \mathbb{R}^{d\times n}$, $\boldsymbol{X} = [\boldsymbol{x}_1, \boldsymbol{x}_2, ..., \boldsymbol{x}_n], \boldsymbol{x}_i \in \mathbb{R}^d$, and $\boldsymbol{x}_i$ is the position vector of edge V_i. As we define in the previous section, vertices V represents the six major faces of a unit cell and $|V| = 6n$ where n is the number of unit cells in a tessellation. Then, the squared distance d_{ij} between $\boldsymbol{x}_i$ and $\boldsymbol{x}_j$ is $d_{ij} = ||\boldsymbol{x}_i - \boldsymbol{x}_j||^2$ where $||\cdot||$ denotes the Euclidean norm.

For example, in Fig. 2.4(b), red dots represent the middle points of the major faces of the tessellations. Here, we can obtain positional vectors for each dots, from $\boldsymbol{x}_1$ to $\boldsymbol{x}_{24}$. Then, we can define the distance matrix $\boldsymbol{D}$ as a 24×24 matrix. For each element of $\boldsymbol{D}$, we get $\boldsymbol{D}_{11} = ||\boldsymbol{x}_1 - \boldsymbol{x}_1||^2 = 0$, $\boldsymbol{D}_{12} = ||\boldsymbol{x}_1 - \boldsymbol{x}_2||^2$, ... , $\boldsymbol{D}_{2424} = ||\boldsymbol{x}_{24} - \boldsymbol{x}_{24}||^2$. Based on the adjacency matrix and distance matrix, we can set up criteria about the validity of the configurations. The condition is $\boldsymbol{D}_{ij} = 0$ for all i and j where $\boldsymbol{A}_{ij} = 1$. This means that those vertices logically attached together ($\boldsymbol{A}_{ij} = 1$) have to be physically in contact ($\boldsymbol{D}_{ij} = 0$) too.

The schematic illustration of this brute-force method is also shown in Fig. 2.6. By utilizing this method, we verify that the number of valid configuration up to 4-by-4 tessellations matches the results from the efficient method. Also, this brute-force method verifies the list of 3-cell tessellations in Fig. 2.7. These 3-cell tessellations are the fundamental building

blocks for any size of TMP tessellations and therefore it is important to verify all of them by using this method.

2.5 Mechanical properties of TMP tessellations

In this section, we describe the folding behavior of the TMP structures based on the folding angles along the crease lines. (mention about figures) We can define three folding angles as θ_M, θ_S, and θ_G as shown in Fig. 2.8. Those angles also satisfy the following relationships:

$$\tan\frac{\theta_G}{2} = \tan\alpha\cos\theta_M \tag{2.1}$$

$$\sin\frac{\theta_G}{2} = \sin\alpha\cos\theta_S \tag{2.2}$$

where α is an angle between main (horizontal) and sub (inclined) crease lines as shown in Fig. 2.8(a). We can also derive the width (W), breadth (B), and height (H) of the unit cell of each state:

$$\begin{aligned} B_{tmp} &= 2m\sin\theta_G + d\cos\theta_M \\ W_{tmp} &= 2l + \frac{d}{\tan\alpha} + 2m\cos\theta_G \\ H_{tmp} &= Nd\sin\theta_M \end{aligned} \tag{2.3}$$

$$\begin{aligned} B_{otp} &= m\sin\theta_G \\ W_{otp} &= 2l + m(1+\cos\theta_G) \\ H_{otp} &= Nd\sin\theta_M \end{aligned} \tag{2.4}$$

$$\begin{aligned} B_{otm} &= m\sin\theta_G \\ W_{otm} &= 2l + m(1+\cos\theta_G) \\ H_{otm} &= Nd\sin\theta_M \end{aligned} \tag{2.5}$$

$$\begin{aligned} B_{def} &= 0 \\ W_{def} &= 2l + 2m + \frac{d}{\tan\alpha} \\ H_{def} &= Nd\sin\theta_M \end{aligned} \tag{2.6}$$

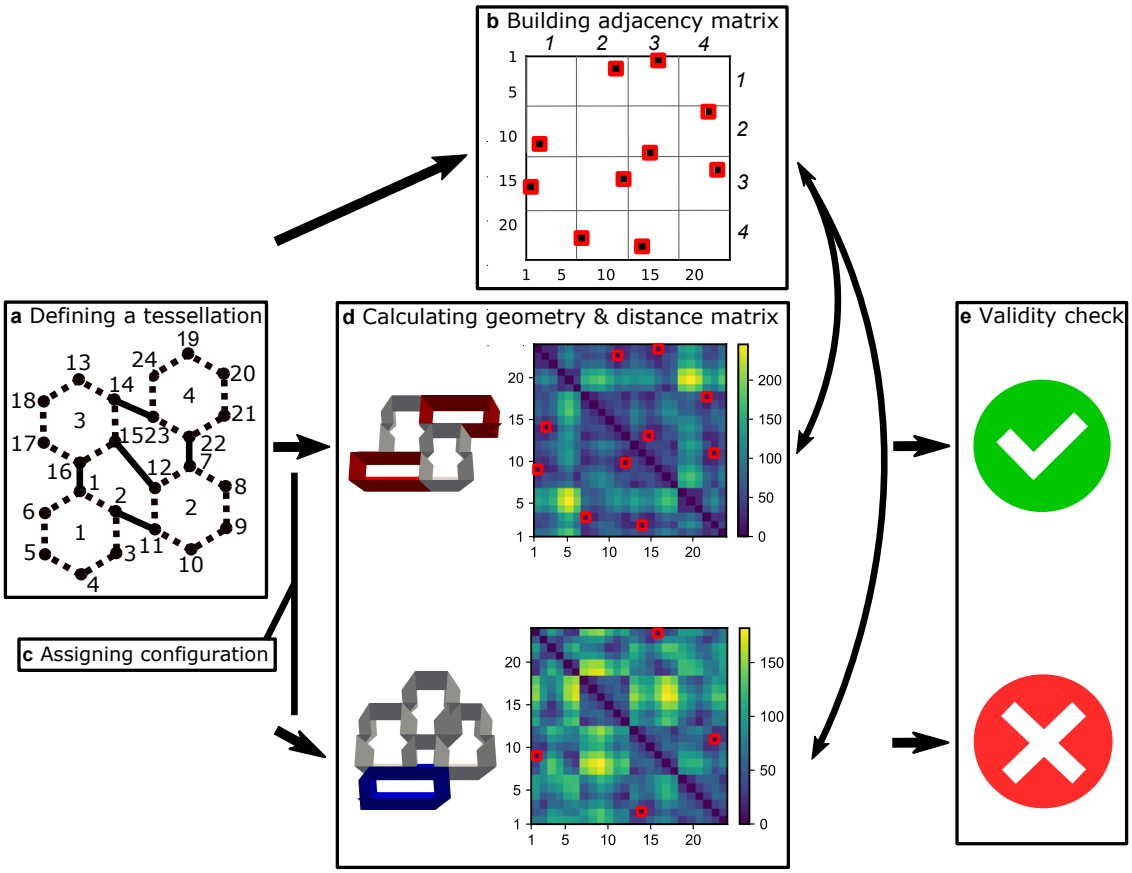

Figure 2.6: Process of the search for valid configurations. **a**, the graph representation of 2-by-2 tessellations. **b**, a plot of a adjacency matrix. Black dots with red peripheries shows the elements of the value of 1 (nodes are connected in the subgraph G'). **c**, assigning configurations (TMP, RP, LP, or Flat) for each unit cell. **d**, the computation of geometry for each unit cell and the plot of distance matrices. Left images show the 3D rendering of the 2-by-2 tessellation after assigning configurations. Right images are the plot of distance matrices. Black dots with red peripheries shows the elements of the value of 0 (middle points are connected in the physical space). **e**, the result of the validity check for the configuration we assigned. If the distance matrix has entries of zero in the same position as the adjacency matrix has entries of one, we can classify a configuration as valid.

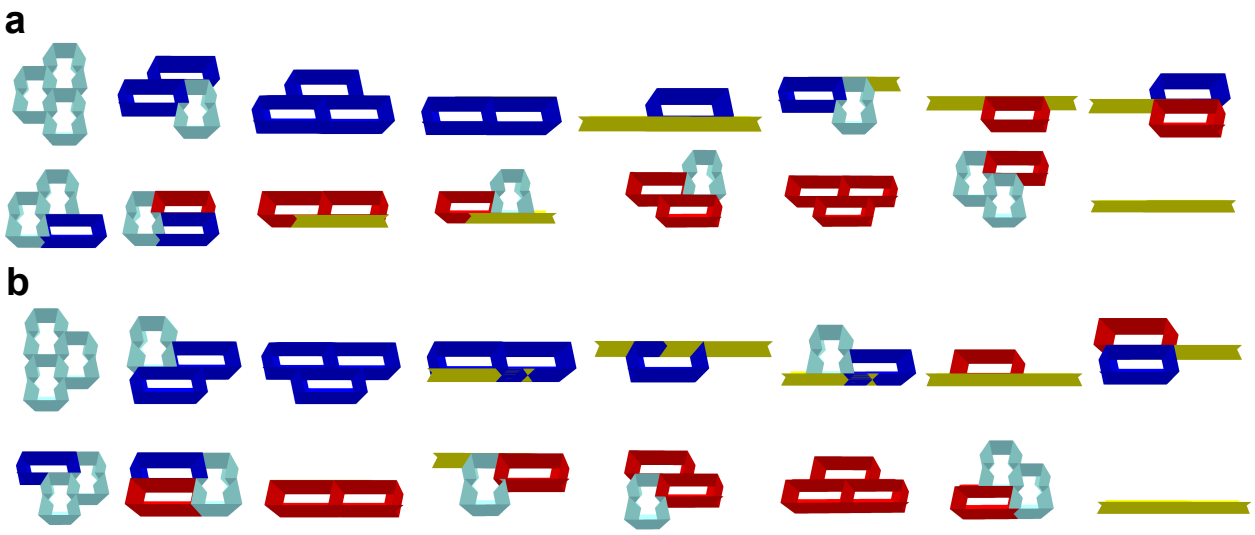

Figure 2.7: A collection of 3-cell tessellations. **a**, tessellations that have two cells on the right side. **b**, tessellations that have two cells on the left side.

where the direction of B, W, H are shown in Fig. 2.8. Each subscript tmp, otp, otm, and def corresponds to four state of TMPs: TMP, Origami Tube +, Origami tube −, and Defect. With the analysis of dimensions of unit cells, we can obtain the cross-sectional area A that is enclosed by a unit cell.

$$\begin{aligned} A_{tmp} &= 2m(2l + m\cos\theta_G)\sin\theta_G \\ A_{otp} &= A_{otm} = m(2l + m)\sin\theta_G \\ A_{def} &= 0 \end{aligned} \tag{2.7}$$

By summing up the cross-sectional area, the total cross-sectional area in the direction of height (3-axis) A_3 can be expressed as follows:

$$A_3 = N_{tmp}A_{tmp} + N_{otp}A_{otp} + N_{otm}A_{otm} \tag{2.8}$$

where N_{tmp}, N_{otp}, N_{otm} are the number of unit cells with TMP state, origami tube +, and origami tube −, respectively. We also define the number of defect cells as N_{def}, resulting the total number of unit cells $N_{cell} = N_{tmp} + N_{otp} + N_{otm} + N_{def}$. Based on these dimensions of

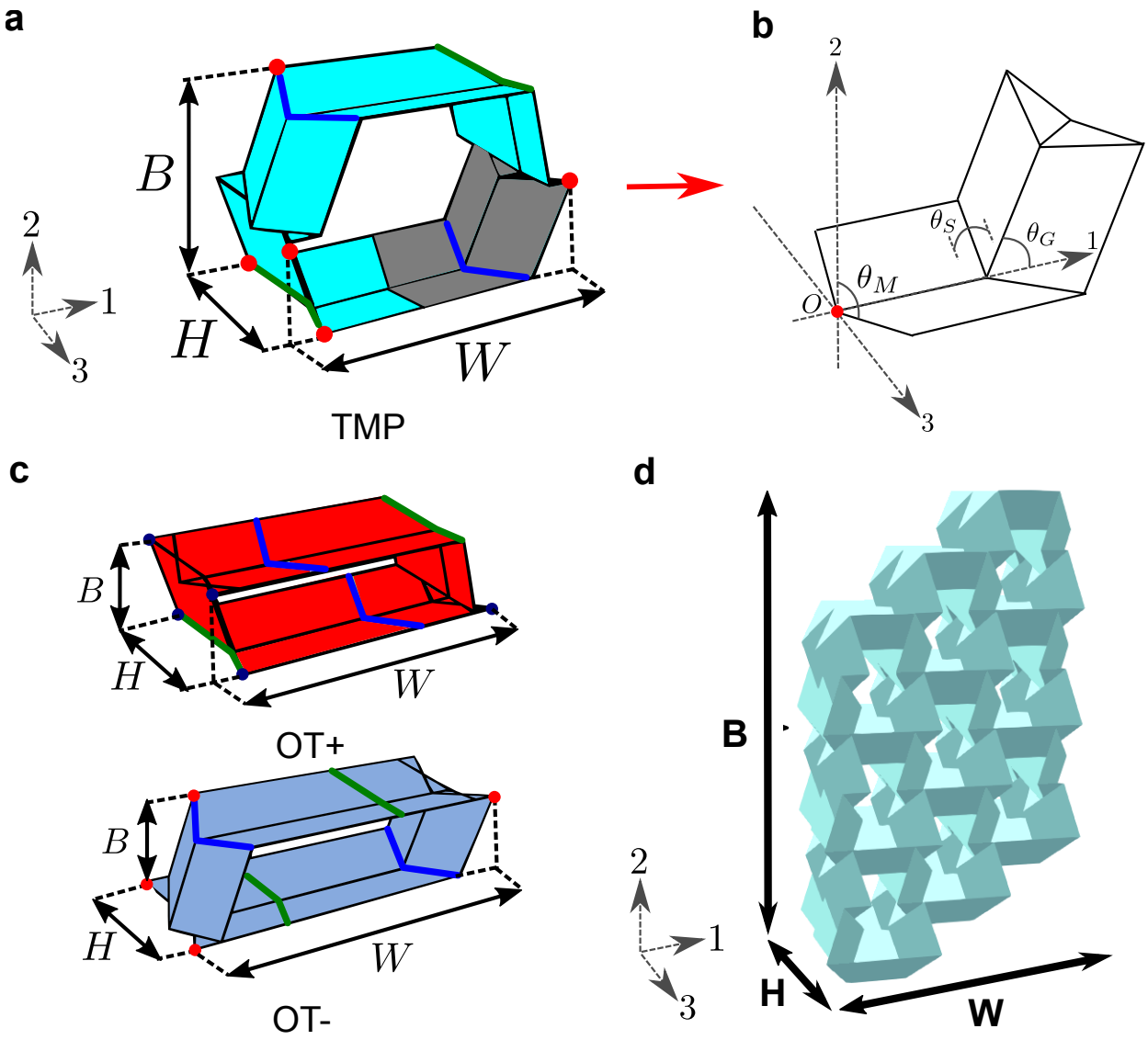

Figure 2.8: Definitions of dimensions and folding angles of a TMP unit cell and a tessellation. **a**, a TMP unit cell. **b**, a Miura-ori unit cell that corresponds the gray area in **a**. **c**, OT+ and OT− unit cells. **d**, a TMP tessellation. Dimensions B, W, and H correspond to the width, breadth, and height of the structure, respectively. Also, axis numbers 1, 2, and 3 have the same direction as width, breadth, and height, respectively.

unit cells, we can express the sizes of four tessellations in Fig. 2.8 as follows:

$$\begin{aligned} B^{(1)} &= 8m\sin\theta_G \\ W^{(1)} &= 8l + \frac{d}{\tan\alpha} + m + 4m\cos\theta_G \\ H^{(1)} &= Nd\sin\theta_M \end{aligned} \tag{2.9}$$

$$\begin{aligned} B^{(2)} &= 4m\sin\theta_G \\ W^{(2)} &= 8l + 2m + 4m\cos\theta_G \\ H^{(2)} &= Nd\sin\theta_M \end{aligned} \tag{2.10}$$

$$\begin{aligned} B^{(3)} &= 6m\sin\theta_G \\ W^{(3)} &= 8l + 2m + 2m\cos\theta_G \\ H^{(3)} &= Nd\sin\theta_M \end{aligned} \tag{2.11}$$

$$\begin{aligned} B^{(4)} &= 5m\sin\theta_G \\ W^{(4)} &= 8l + 3m + \frac{d}{\tan\alpha} + 2m\cos\theta_G \\ H^{(4)} &= Nd\sin\theta_M \end{aligned} \tag{2.12}$$

where the superscript (1), (2), (3), and (4) correspond to the case 1 to 4 in Fig. 2.11, respectively. With the definitions of dimensions, we can analyze the Poissonś ratio of the tessellations. Here, the definitions of the Poissonś ratio are as follows:

$$\begin{aligned} \nu_{HB} &= -\frac{(dB/B)}{(dH/H)} \\ \nu_{HW} &= -\frac{(dW/W)}{(dH/H)} \end{aligned} \tag{2.13}$$

The Poissonś ratio can be derived analytically or numerically. The results are shown in Fig. 2.11. Besides the geometrical features of TMPs, we can also model the mechanical properties of TMPs. To this end, we assume that the structures are consist of rigid plates and linear torsional springs along the crease lines [1]. With this assumption, we can apply the principle of the virtual work as follows:

$$F_i\delta u_i = 2L_M M_M \delta\theta_M + 2L_S M_S \delta\theta_S \tag{2.14}$$

where L is the total length of the crease lines and M is the bending moment along the crease lines per unit length. The subscripts M and S denote the main (horizontal) crease lines and sub (inclined) crease lines, respectively. The subscript $i = 1, 2, 3$ indicates the direction of the axis. The total length of the crease line of TMP tessellations are obtained as follows:

$$L_M = N_{cell}(N-1)\left(4l + 4m + \frac{2d}{\tan\alpha}\right) \tag{2.15}$$

$$L_S = \frac{8N_{tmp}Nd}{\sin\alpha} + \frac{6(N_{otp} + N_{otm})Nd}{\sin\alpha} \tag{2.16}$$

Based on the aforementioned assumption, we can express the bending moment as $M = 2k_\theta(\theta - \theta_0)$ where k_θ is a spring constant and θ_0 is an initial angle. Here, we investigate the mechanical response of the height direction (3-axis). The displacement of this direction u_3 is defined as $u_3 = H_0 - H$ where H_0 is the initial height. The variation of the displacement δu_3 is as follows:

$$\delta u_3 = -Nd\cos\theta_M \delta\theta_M \tag{2.17}$$

Then, we get the following equation of normalized version of force F_3':

$$F_3' = \frac{F_3}{k_\theta L_M/d} = -\frac{4}{N\cos\theta_M}\left\{(\theta_M - \theta_M^{(0)}) + \frac{L_s}{L_M}(\theta_S - \theta_S^{(0)})\frac{\cos^3\frac{\theta_G}{2}\sin\theta_M}{\cos\alpha\sin\theta_S}\right\} \tag{2.18}$$

where the superscript (0) denotes the initial folding angle. With this normalized force and the cross-sectional area enclosed by the whole structure of a TMP tessellation, we can define stress within the tessellation. Also, we can define strain along 3-axis (Height). The strain and stress are expressed as follows:

$$\epsilon_3 = \frac{u_3}{H_0} \tag{2.19}$$

$$\sigma_3' = \frac{F_3'}{A_3} \tag{2.20}$$

The stress-strain relationship for four cases of TMP tessellations are shown in Fig. 2.11. Based on the stress-strain relationship, we can obtain Youngś modulus. We use the stress value at the 2% strain and calculate the slope between two values as follows:

$$E_3' = \frac{\sigma_3'}{\epsilon_3|_{2\%}} \tag{2.21}$$

2.6 Results and discussion

2.6.1 Estimation and growth of reconfigurability

We start discussing the number and growth of reconfigurability by changing the size of tessellations. The result of the search for the number of valid configurations with 14 different tessellation sizes is summarized in Figs. 2.9(a) and (b) for selected results and Table 2.1 for all results. To verify the result from our graph-theoretical method, we also implement a brute-force method for smaller sizes of tessellations as explained in the previous section. We start to examine the unique configurations with 2-by-2 tessellations with the total number of four unit cells. We then enlarge the size of the tessellation by adding a row or a column of unit cells up to 49 unit cells in total. If we follow the brute-force method for this number of unit cells, we have to investigate $4^{49} \approx 10^{29}$ candidates of configurations that are almost impossible to examine even with the aid of high-performance computers. Fig. 2.9(c) shows the comparison of computation time between brute-force and graph-based methods. In terms of computation time, our graph-based method is generally 20 to 100 times faster than the brute-force method to search configurations from 2-by-2 to 5-by-5 tessellations with a personal desktop computer. Therefore, by utilizing our method, we achieve a substantial amount of efficiency in estimating the reconfigurability of the origami-based metamaterials.

As we increase the size of the tessellation, we see that the number of unique configurations increases exponentially for X-by-2 and 2-by-Y cases where X and Y are the number of horizontal and vertical stacking, respectively. For an N-by-N tessellation where N is for both horizontal and vertical numbers, we see that the rate of increase decays gradually. Furthermore, we observe that the rate of increase in the number differs by the direction of adding a new column or row (horizontally or vertically). Adding a column of unit cells to the tessellation doubles the unique configurations to the original one, whereas adding a row quadruples them. In Fig. 2.10, we show an example of adding a row or a column to the 2-by-2 tessellation. While we obtain two different configurations in Fig. 2.10(b) for 3-by-2 tessellation, we can achieve four configurations for 2-by-3 tessellations in Fig. 2.10(c). We

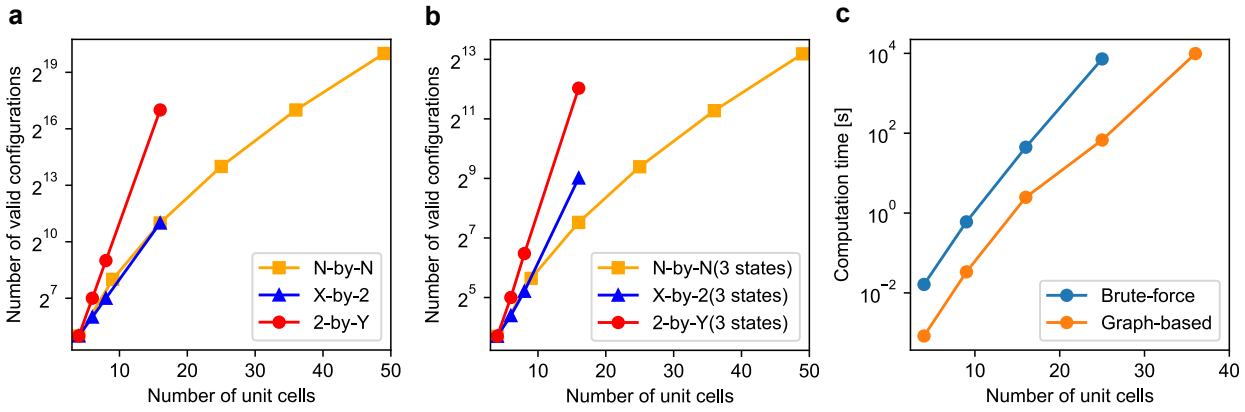

Figure 2.9: The number of valid configurations and computation time for each tessellation size. **a**, 14 results of counting valid configurations with four configurations (TMP, OT+, OT-, and Defect) based on the categorization of N-by-N, X-by-2, and 2-by-Y tessellations where X, Y, and N are the number of horizontal and vertical stackings of the tessellation. **b**, 14 results of counting valid configurations with three configurations (OT+/OT−/Defect, TMP/OT+/Defect, TMP/OT−/Defect, and TMP/OT+/OT−). Each three-state configuration has the same number of valid configurations. Other results and exact numbers are shown in Table 2.1. **c**, a comparison of computation time between brute-force and graph-based methods. The results of 2-by-2, 3-by-3, 4-by-4, and 5-by-5 tessellations are used for the brute-force method. Besides those tessellations, an additional result of 6-by-6 tessellations is shown for the graph-based method.

observe this difference is caused by the direction of the phase transition of unit cells. Since the transition among TMP, OT+, and OT− is lateral movement, the column-wise attachment of unit cells is more bound to the existing tessellations than the row-wise attachment. Actually, a column-wise attachment involves only TMP and OT+ in Fig. 2.10(b). However, a row-wise addition includes TMP, OT+, OT−, and defects in Fig. 2.10(c).

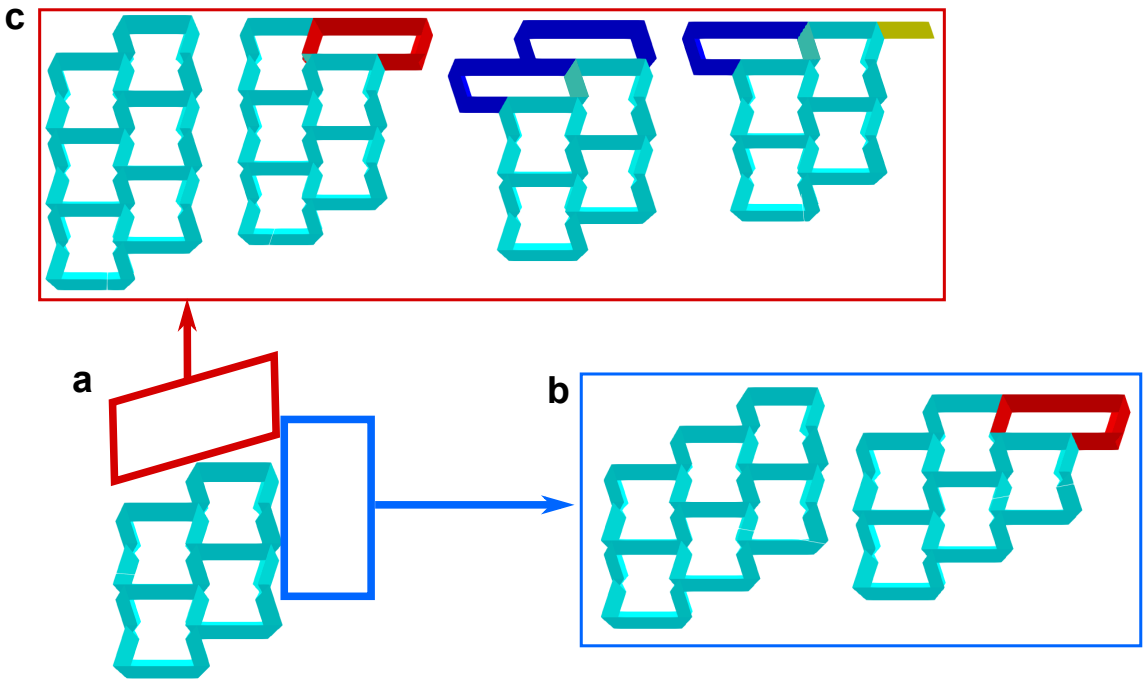

Figure 2.10: **a**, an image of a 2-by-2 tessellation with four TMPs. Red box shows the position where the unit cells are attached to build 2-by-3 tessellations. Likewise, blue box shows the position for 3-by-2 tessellations. **b**, 3-by-2 valid tessellations that are emerged from a 2-by-2 tessellation with four TMPs shown in **a**. **c**, 2-by-3 valid tessellations that are emerged from a 2-by-2 tessellation with four TMPs shown in **a**. In both **b** and **c**, these tessellations are the only ones that can emerge from the 2-by-2 tessellation in **a**. Cyan, red, blue, and yellow colors in the 3D rendered images correspond to the TMP, OT+, OT−, and defect states of the unit cell, respectively.

Returning to Fig. 2.9(a), the red line connects the results from 2-by-2, 2-by-3, 2-by-4, and 2-by-8 tessellations. Likewise, the blue line connects the results from 2-by-2, 3-by-2, 4-by-2, and 8-by-2 tessellations. Both lines show linear growth in $\log_2$ scale along the y-axis because there is a pattern for the growth of the unique configurations, as we state previously. The yellow line shows the results up to 7-by-7 tessellations. Since these results are from the combinations of the horizontal and vertical increments, the increase rate is not constant.

Table 2.1 also includes the number of unique configurations only with three states (OT+/OT-/Defect, TMP/OT+/Defect, TMP/OT-/Defect, and TMP/OT+/OT-) and the rate of increase of the number of configurations from using three states to four states. Here, each combination of three states (OT+/OT-/Defect, TMP/OT+/Defect, TMP/OT-/Defect, and TMP/OT+/OT-) has the same number of valid configurations and is summarized in Fig. 2.9(b). The comparison with the four states indicates that each TMP state equally contributes to the excessive growth of reconfigurability. However, one of the advantages of inducing defect states is that we can achieve an enormous variety of reconfigurable shapes without incurring volume increases. Based on the graph-theoretic evaluations, we confirm that the increase of the phase number from three to four contributes directly to the surge of the overall variety of the tessellations.

Table 2.1: Number of unique configurations for various tessellation sizes.

Size	4 states	3 states	Increase	Size	4 states	3 states	Increase
2-by-2	32	13	146%	3-by-4	1024	120	753%
3-by-2	64	21	205%	4-by-4	2048	184	1013%
2-by-3	128	32	300%	8-by-2	2048	517	296%
4-by-2	128	37	246%	2-by-8	131072	4181	3035%
2-by-4	512	89	475%	5-by-5	16383	672	2338%
3-by-3	256	50	412%	6-by-6	131072	2480	5185%
4-by-3	512	82	524%	7-by-7	1048576	9312	11160%

2.6.2 Highly heterogeneous configurations

Now we discuss some examples of configurations we discover in the search process. Figs. 2.11(a)-(d) show the four examples of anomalous configurations in 4-by-4 tessellations. Each configuration consists of four different states (TMP, OT+, OT−, and Defect), and the composition of the states is highly mixed and distributed within the tessellation. For example, a tessellation in Fig. 2.11(a) consists of six TMPs, two OT+, six OT−, and two Defects. We again note in passing that unlike normal configurations that have a homogeneous occurrence of deformation states, such heterogeneous configurations composed of a variety of the different states are hard to be discovered by human heuristics.

In addition to the heterogeneity of the configurations, we find that they have tunability in terms of Poisson's ratio and mechanical properties. Here, we examine two Poissonś ratios ν_{HB} and ν_{HW} defined as follows:

$$\nu_{HB} = -\frac{dB/B}{dH/H}, \quad \nu_{HW} = -\frac{dW/W}{dH/H}. \tag{2.22}$$

Revisit Fig. 2.1(b) for the definitions of H and B. Fig. 2.11(e) shows the change of Poisson's ratio ν_{HB} from the folding angle of 0° to 90°. Throughout the folding stage, ν_{HB} becomes both positive and negative (auxetic). While ν_{HB} is identical for all cases in Fig. 2.11(e), Poisson's ratio ν_{HW} in Fig. 2.11(f) is different for each configuration and always negative. These results suggest that we can tune one Poisson's ratio while keeping a property in another direction. Besides, the stress-strain relationships are shown in Fig. 2.11(g) where we define a cross-sectional area as the area occupied by the tessellations. Here, stress is obtained by using normalized force F'. Base on this result, we can obtain normalized Youngś modulus of the direction of height (3-axis) E'_3 at 2% strain for each configuration defined as follows:

$$E'_3 = \frac{\sigma'_3}{\epsilon_3|_{2\%}} \tag{2.23}$$

For case 1 to 4 in Fig. 2.11, the values are 2.13×10^{-3}, 2.55×10^{-3}, 2.19×10^{-3}, and 2.67×10^{-3}, respectively. We note that those values are calculated using normalized force; therefore, they

do not have dimensions, and we can apply the material properties once we decide on the material to use for the manufacturing.

We further extend this result to see if they can simulate specific geometries because such reconfigurability is one of the essential aspects when we utilize these mechanical metamaterials for engineering applications. To assess how much the tessellation's reconfigurability contributes to the ability to simulate the real-life objects, we examine cross-sections of 4-by-4 tessellations and compare them with some images in Fig. 2.12. The result of simulating mechanical properties and the various types of geometries (chair, buffalo, boot, and boat) suggests that this platform of TMP tessellations has great potential to satisfy the mechanical and geometrical requirements for various engineering applications. Furthermore, this rich versatility of TMP tessellations manifests the importance of efficient methods to find valid configurations because it contributes not only to the fundamental problems of mathematical/geometrical combinations but also to the design of advanced mechanical metamaterials.

2.6.3 Cross-sectional similarity to real-life objects

In the previous sections, we find that TMP tessellations have reconfigurability to a great extent. Here, we introduce some of the configurations whose cross sections have similarities to real-life objects. Fig. 2.12 shows voxel-art-like cross sections of 4-by-4 TMP tessellations that resemble a chair, buffalo, boot, and boat. While they only have 16 unit cells, these results imply that the rich reconfigurability of TMP tessellation can be engineered to meet the complex geometric design requirements for actual engineering use by increasing the number of unit cells in a tessellation.

2.7 Conclusion

In this study, we have demonstrated a graph-theoretical approach to discover the valid configurations of TMP tessellations. Given the challenges of combinatorial problems of origami-based mechanical metamaterials, we have built a computationally efficient framework to account for a complete set of reconfigurable shapes of the TMP tessellations. To this end,

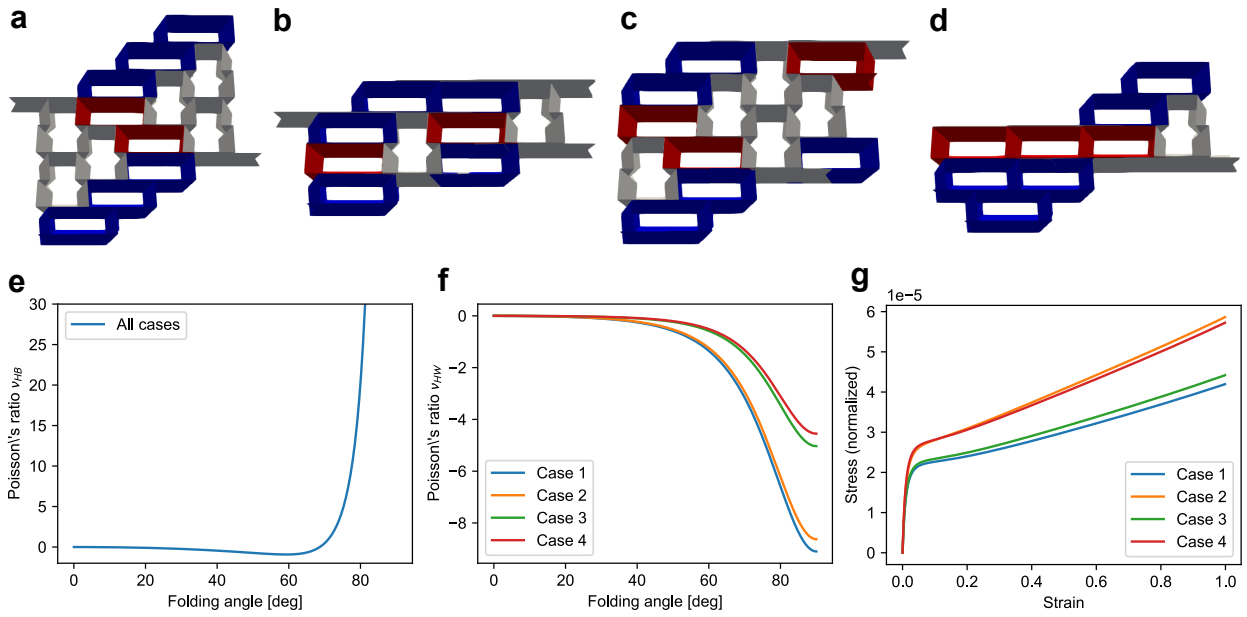

Figure 2.11: Examples of heterogeneous configurations in 4-by-4 tessellations and their Poisson's ratio and mechanical responses. **a**, a configuration consisting of 6 TMPs, 2 OT+, 6 OT−, and 2 defects (Case 1). **b**, a configuration consisting of 2 TMPs, 2 OT+, 5 OT−, and 7 defects (Case 2). **c**, a configuration consisting of 5 TMPs, 3 OT+, 5 OT−, and 3 defects (Case 3). **d**, a configuration consisting of 1 TMP, 3 OT+, 5 OT−, and 7 defects (Case 4). **e**, Poisson's ratio between height and breadth directions. For all cases, Poisson's ratio ν_{HB} is identical. **f**, Poisson's ratio ν_{HW} between height and width directions. **g**, Stress-strain relationship of four cases. Here, stresses are calculated with normalized forces.

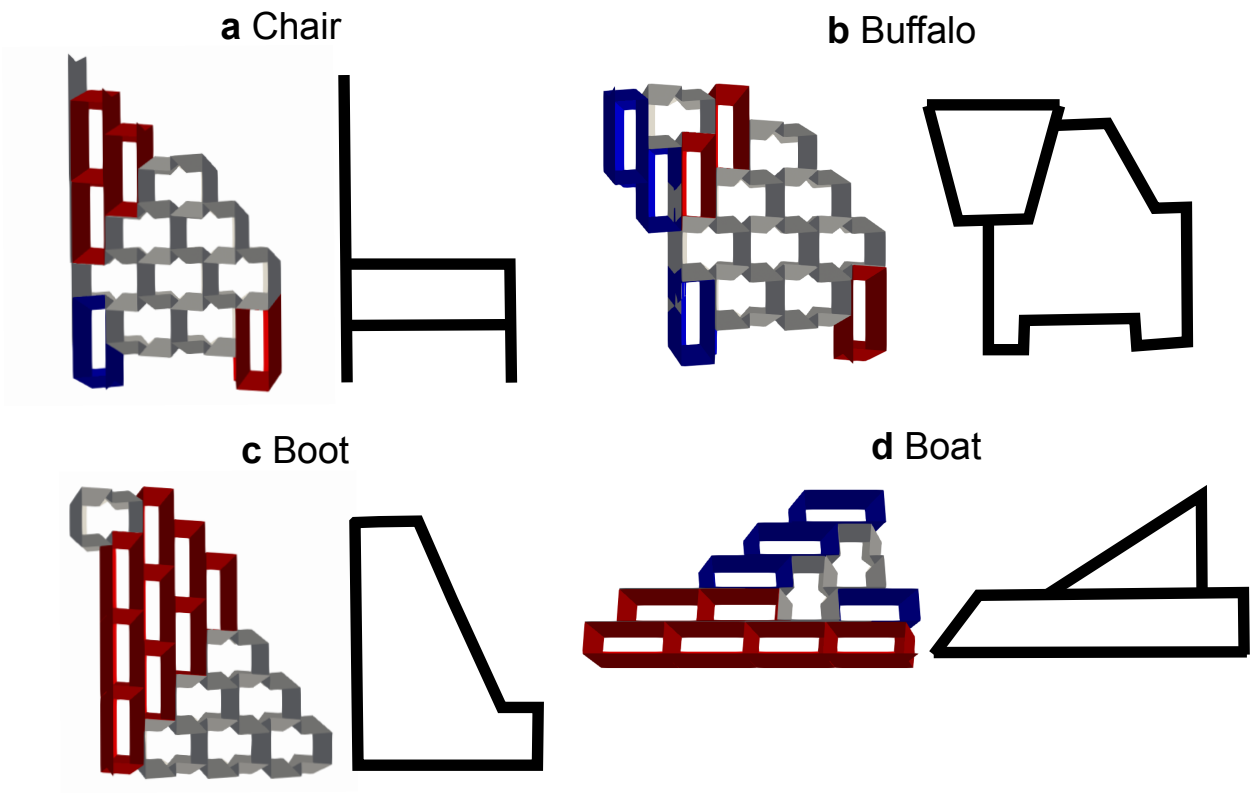

Figure 2.12: Voxel-art configs in 4by4. In **a**, **b**, **c**, and **d**, each picture of 4-by-4 tessellations has corresponding images of chair, buffalo, boot, and boat, respectively. Pictures in **a**, **b**, and **c** are rotated by 90 degrees.

we have enumerated the information about the connections of the TMP unit cells using adjacency matrices. One of the unique features of this versatile graph-theoretical approach is that it has the possibility to be applied for designing various types of mechanical metamaterials. This simple approach of using adjacency matrices has proposed an efficient method to describe and analyze the tessellation of the mechanical metamaterials. The result of the aforementioned analysis indicates that the TMP tessellations have an abundance of reconfigurability owing to the heterogeneity of the TMP cells and their versatile connectivity. Besides, the analysis of mechanical properties, such as Poisson's ratio and elastic modulus, suggests that the various configurations of the tessellations yield a wide range of design space. Such reconfigurability can be exponentially improved by adopting a larger number of TMP cells in the tessellation, and the exact number of possible configurations has been calculated by the proposed graph-theoretic method in an accurate and efficient manner.

Given the simplicity of this framework, the graph-based approach can be applied to the other types of the tessellations of mechanical metamaterials (e.g., metal-organic hinged cube tessellation [62], voxelated mechanical metamaterials [14, 63], and other origami lattices in 2D or 3D settings [18, 19, 31, 64, 65]) by building graph representations for each architecture of mechanical metamaterials and by understanding the connections within the tessellations. For instance, 3D stacked miura-ori variant mechanical metamaterials [19] have multistability in their unit cells that is similar to TMP unit cells. Furthermore, they can form tessellations. Therefore, there is a rich reconfigurability, and the analysis using this graph-based framework can be highly useful. Also, the ability to simulate the various mechanical responses, shapes and morphologies suggest the possibility of answering the following question; given the target geometry and properties we want to achieve, can we dial-in the local phases in unit cells and find the optimal metamaterial configurations globally? This can be assessed by utilizing the graph-theoretical framework developed herein and combining it with combinatorial optimization techniques.

2.8 Author contributions

This chapter is based on the paper: K. Yamaguchi, H. Yasuda, K. Tsujikawa, T. Kunimine, J. Yang, "Graph-theoretic estimation of reconfigurability in origami-based metamaterials," Materials & Design 213 (2021) 110343 [66]. K.Y, H.Y, K.T, T.K, and J.Y conceived the idea of this project. The numerical studies and writing the original draft were carried out by K.Y. K.Y, H.Y, T.K, and J.Y contributed to the review and editing of the manuscript. J.Y supervised the project. All authors contributed to the paper with valuable inputs.

Chapter 3

POST-FABRICATION TUNING OF MECHANICAL METAMATERIALS BASED ON TACHI-MIURA POLYHEDRON

In the previous chapter (Ch. 2), we focused primarily on the schematic and combinatorial aspects of the design space for origami-based mechanical metamaterials. While understanding this rich geometrical complexity is crucial, a thorough investigation of the material's mechanical properties is also necessary to fully leverage its capabilities for engineering applications. Therefore, this chapter demonstrates a method for achieving extensive post-fabrication tunability in a three-dimensional, origami-based mechanical metamaterial composed of Tachi-Miura Polyhedron (TMP) tessellations [17, 66, 67, 68]. We introduce an efficient, honeycomb-inspired fabrication technique and utilize a heat-processing method to controllably alter the structure's natural, zero-energy posture after it has been built. Through a combination of mechanical modeling [44] and experimental validation, we show that this tuning allows for orders-of-magnitude changes in key mechanical properties, including a 60-fold variation in Young's modulus and a 10-fold variation in effective density, all from a single manufactured sample. We also document a unique inverse correlation where stiffness increases as density decreases and visualize this extensive, anisotropic design space using novel three-dimensional Ashby charts [69]. Our main contribution is a practical and predictable framework for creating adaptable metamaterials whose mechanical properties can be actively tuned in-situ to meet changing functional demands, paving the way for advanced, lightweight, and reconfigurable engineering systems.

3.1 Prototype Fabrication

3.1.1 Construction of a TMP unit cell

A TMP unit cell is composed of two flat-foldable origami sheets, featuring four adjustable geometric design parameters (l, m, d, α) as illustrated in Fig. 3.1(a). By assigning appropriate folding directions (mountain or valley) to these origami sheets and combining them, a unit cell can be formed, as seen in Fig. 3.1(b). The dimensions of a unit cell, such as breadth, height, and width, can be defined and calculated in terms of the aforementioned geometrical parameters under the rigid foldability assumption [44]. Additionally, folding angles θ_m, θ_s, and θ_g as indicated in the Miura-ori subset (see the inset of Fig. 3.1(b)) can be established to describe the folding state (posture) of TMP. Owing to the nature of the origami sheet components, a TMP unit cell can exhibit two flat-folded states ($\theta_m = 0°$ and $\theta_m = 90°$) and a wide range of dimensional variations in a transient state, as demonstrated in Fig. 3.1(c). Detailed kinematic analysis of a TMP unit cell can be found in the next Section.

3.1.2 TMP folding angles and geometries

We obtain the relationship of the three folding angles of the Tachi-Miura Polyhedron (TMP) unit cell. The design parameters of the unit cell (l, m, d, α) are represented in Fig. 3.2(a) with two sheets of Miura-folding components. These components construct a TMP unit cell as shown in Fig. 3.2(b). Here, to define the folding angles, we utilize the quarter part of the unit cell presented as a grey-colored area of Fig. 3.2(b). The folding angles θ_m, θ_s, and θ_g as shown in Fig. 3.2(c). Based on the rigid origami theory and the geometry of the Miura-folding, we obtain the relationships among the three angles as follows [1]:

$$\begin{aligned} \tan\frac{\theta_g}{2} &= \tan\alpha\cos\theta_m \\ \sin\frac{\theta_g}{2} &= \sin\alpha\cos\theta_s \end{aligned} \tag{3.1}$$

To address the dimensions of TMP tessellations, we start with expressing the dimension of a TMP unit cell. First, we analyze the minimal component of a Miura-ori unit to obtain the

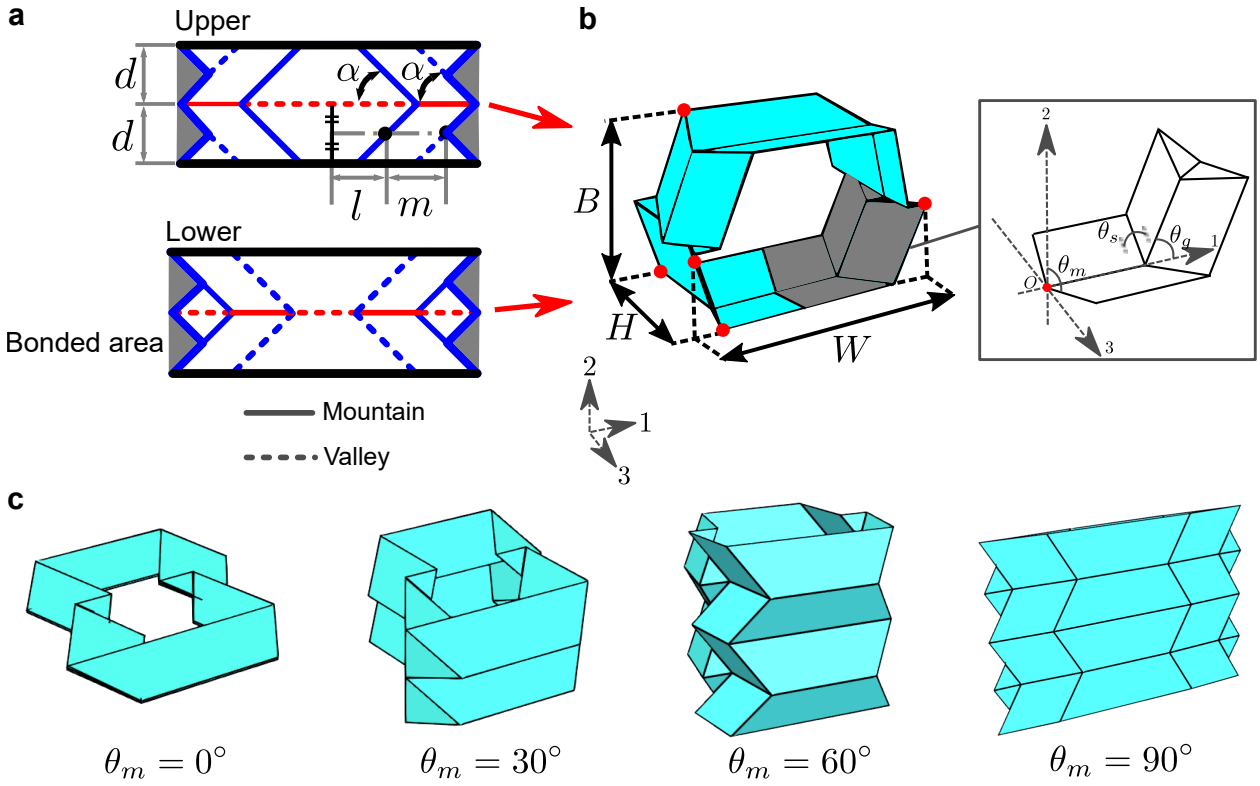

Figure 3.1: A unit cell of Tachi-Miura Polyhedron. **a**, the definition of crease patterns and geometrical parameters of two flat-foldable sheets composing the TMP. Red and blue lines represent the main (horizontal) and sub (inclined) crease lines, respectively. Grey-colored areas represent the bonding region to construct a unit cell. **b**, a unit cell of Tachi-Miura Polyhedron composed of two origami sheets. Dimensions B, W, and H correspond to the width, breadth, and height of the structure, respectively. The inset in **b** is a Miura-folding unit cell that corresponds to the gray area in **b**. **c**, folding process of a TMP unit cell. Each picture corresponds to folding angles $\theta_m = 0°$, $\theta_m = 30°$, $\theta_m = 60°$, and $\theta_m = 90°$, from left to right.

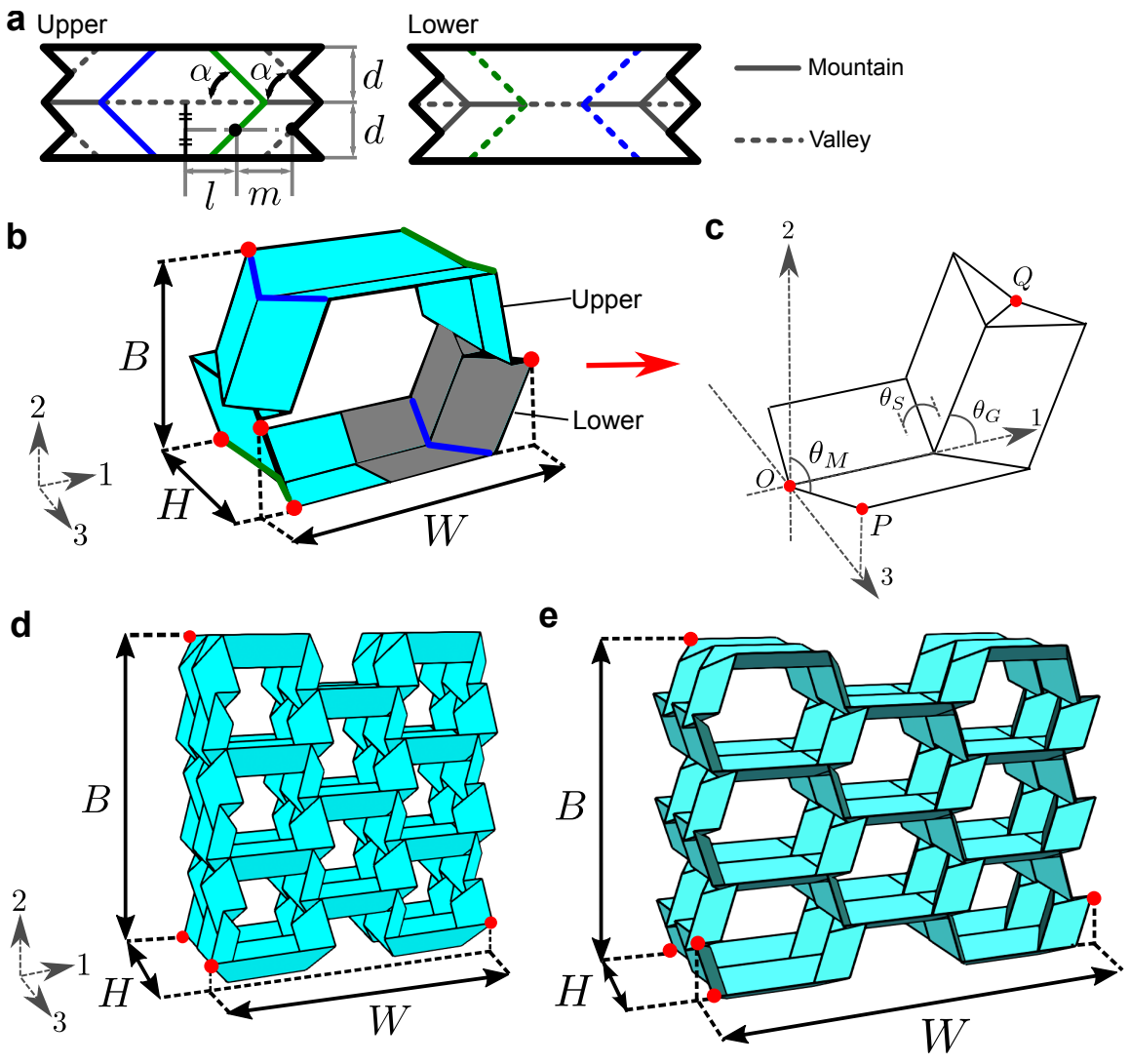

Figure 3.2: Definition of reconfigurable Tachi-Miura Polyhedron (TMP) unit cell. **a**, the definition of crease patterns and geometrical parameters of two flat-foldable sheets composing the TMP. **b**, Dimensions B, W, and H correspond to the width, breadth, and height of the structure, respectively. Also, axis numbers 1, 2, and 3 have the same direction as width, breadth, and height, respectively. **c**, a Miura-ori unit cell that corresponds to the gray area in **a**. **d** and **e**, Dimensions of TMP tessellations with different phases of folding.

position vector $\overrightarrow{OQ} = \mathbf{q}$ and $\overrightarrow{OP} = \mathbf{p}$ from the origin as shown in Fig. 3.2(c).

$$\mathbf{q} = \begin{bmatrix} l + \frac{d}{2\tan\alpha} + m\cos\theta_g \\ m\sin\theta_g \\ 0 \end{bmatrix} \tag{3.2}$$

$$\mathbf{p} = \begin{bmatrix} 0 \\ 0 \\ d\sin\theta_m \end{bmatrix} \tag{3.3}$$

Regarding the aforementioned position vectors and the symmetries of the unit cell, we obtain the dimension of a TMP unit cell as follows:

$$\begin{aligned} B_{unit} &= m\sin\theta_g \\ H_{unit} &= Nd\sin\theta_m \\ W_{unit} &= 2l + \frac{d}{\tan\alpha} + 2m\cos\theta_g \end{aligned} \tag{3.4}$$

where N_H represents the number of layers in the height direction. The dimensions of a TMP tessellation can be obtained based on the dimensions of a unit cell. Fig. 3.2(d) and (e) show the two phases of the folding process of a TMP tessellation and associating dimensions. Here, the definition of width changes in the process of folding since the pair of vertices that has the longest distance changes. Therefore, in the case of an 8-cell tessellation, we obtain the following equations for the dimensions of a TMP tessellation.

$$\begin{aligned} B &= 2N_B m\sin\theta_g + d\cos\theta_m \\ H &= N_H d\sin\theta_m \\ W &= \max\left(N_W\left(2l - \frac{d}{\tan\alpha}\right) - 2(N_W - 1)m\cos\theta_g, 2N_W l + (N_W + 1)m\cos\theta_g + \frac{d}{\tan\alpha}\right) \end{aligned} \tag{3.5}$$

The parameters $N_B = 3$ and $N_W = 3$ represent the number of unit cells in the direction of breadth or width, respectively. Here, due to the switch of the pair of vertices that takes the longest distance width-wise, the measurement of width is the longer value between the

two definitions. Examples of this change of the definition of width are shown in Fig. 3.3(a) and (b). This non-smooth switching of the measurement of width yields the discontinuity in Poisson's ratio ν_{HW} and ν_{BW}.

Based on the analysis of the geometry of a TMP unit cell as shown in Fig. 3.3(c), we can obtain the cross-sectional area of the unit cell.

$$A_{unit} = 2m \sin\theta_g (2l + m\cos\theta_g) \tag{3.6}$$

The cross-sectional area A of the tessellation of TMP unit cells is the multiplication of A_{unit}. Therefore, we obtain the analytical expression as follows:

$$A = N_{cell} A_{unit} = 2N_{cell} m \sin\theta_g (2l + m\cos\theta_g) \tag{3.7}$$

where $N_{cell} = N_B N_W - (N_W - 1)/2$ represents the number of the unit cells within the tessellation.

3.1.3 Strategies to construct a TMP tessellation

In this section, we explore approaches to manufacturing a prototype of a TMP tessellation. Prior research on TMP tessellation employs a cell-by-cell manufacturing technique, in which each fabricated unit cell is combined to form a tessellation [17], as depicted schematically in Fig. 3.4(a). This method has its own merits, such as the modular construction of the structure. However, it necessitates the production of multiple TMP unit cells and results in increased manufacturing time and redundant materials at the interfacial walls between the cells. Thus, to attain manufacturing efficiency, we adopt a method inspired by the fabrication process of honeycomb structures, where corrugated sheets are connected [70]. Previous work on honeycomb-inspired origami structures demonstrates its efficiency in terms of manufacturing [71, 72]. In this study, we expand the concept of honeycomb-inspired origami structures for the efficient fabrication of TMP-based mechanical metamaterials.

To this end, it is preferable to fabricate large portions of the origami structure, corrugate, and assemble them collectively. Fig. 3.4(b) presents schematic illustrations of a layer-by-layer

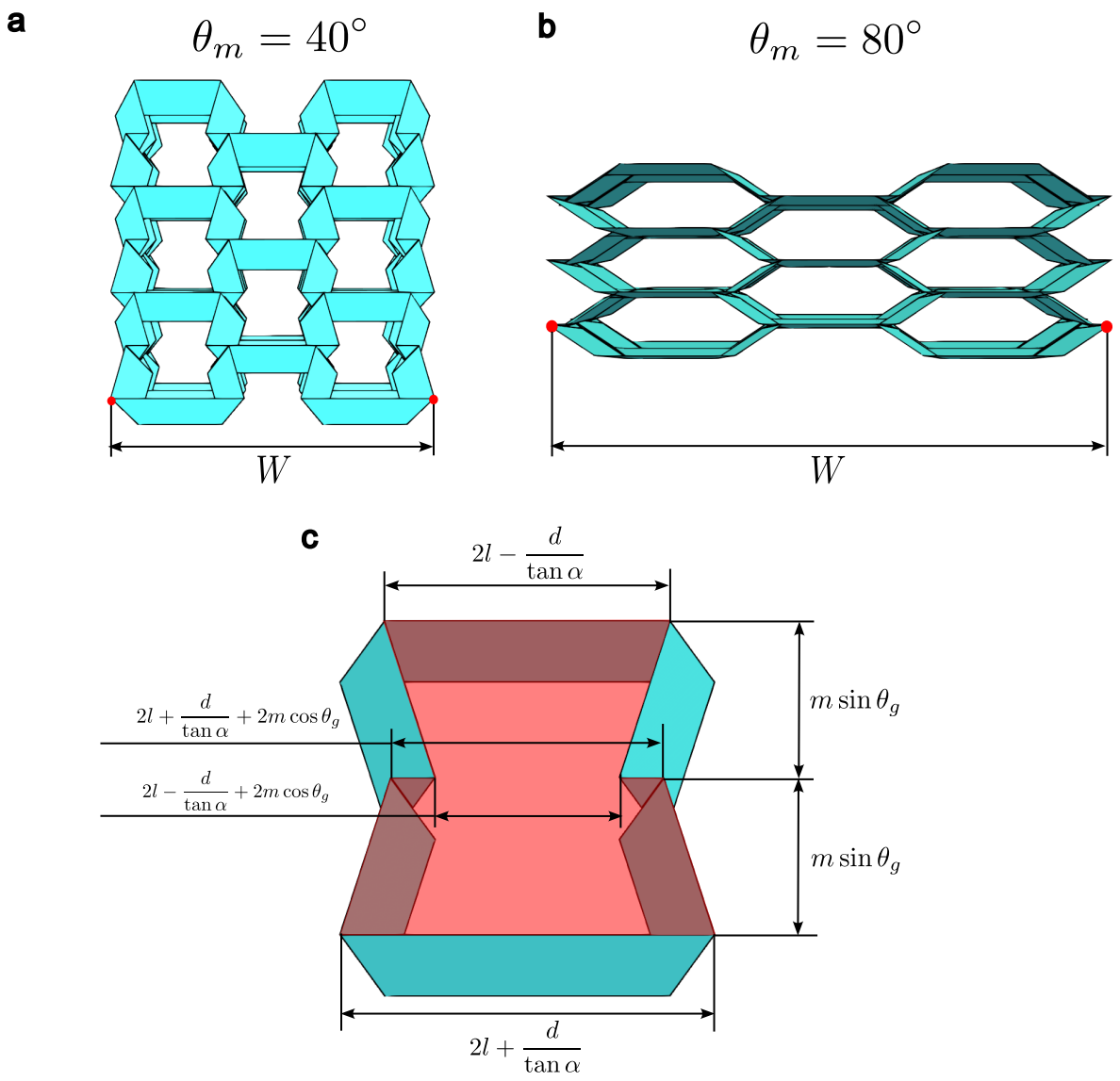

Figure 3.3: Details of the geometry of a TMP unit cell. **a** and **b**, the switch of the measurement of width depending on the folding angle. **a**, a case with a smaller folding angle. **b**, a case with a larger folding angle. **c**, a cross-sectional area of a TMP unit cell. Red-colored area depicts the cross-sectional area, and the associated dimensions are presented.

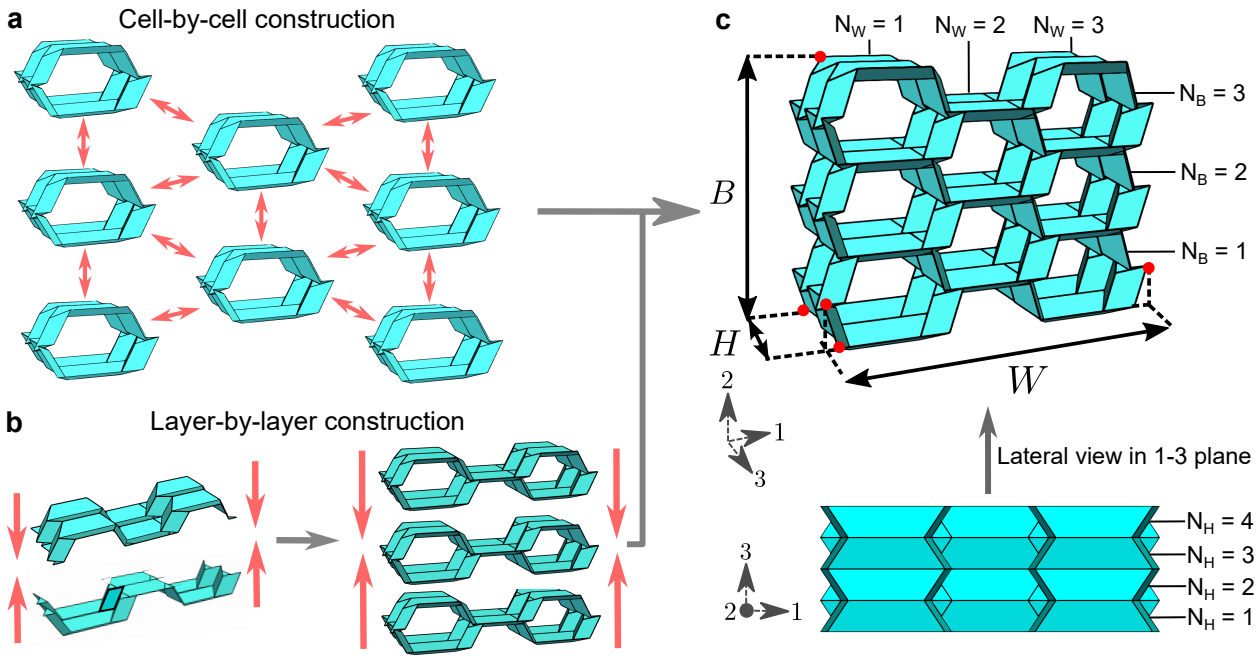

Figure 3.4: A tessellation of Tachi-Miura Polyhedron. **a**, a schematic illustration of a cell-by-cell construction of a TMP tessellation. **b**, a schematic illustration of a layer-by-layer construction of a TMP tessellation. **c**, a TMP tessellation. Dimensions B, W, and H correspond to the width, breadth, and height of the structure, respectively. Also, axis numbers 1, 2, and 3 have the same direction as width, breadth, and height, respectively. N_B and N_W represent the number of unit cells in the direction of breadth and width, respectively. The inset of **c** shows the lateral view of the tessellation in the 1-3 plane. N_H represents the number of layers of the tessellation in 3-direction.

manufacturing process. In Fig. 3.4(b), two long origami sheets are attached, forming a lateral layer of a tessellation. Subsequently, multiple lateral layers are combined to create a tessellation. Theoretically, both cell-by-cell (Fig. 3.4(a)) and layer-by-layer (Fig. 3.4(b)) construction techniques can yield a tessellation with the same configuration (Fig. 3.4(c)). However, these two configurations will differ in terms of the materials consumed. For example, all interfacial walls in cell-by-cell construction would require double layers, while only horizontal walls will be double-layered in the layer-by-layer construction. We will account for such geometrical features when we analyze the TMP tessellations mathematically in Section 3.2.

3.1.4 Manufacturing of a TMP tessellation

Building upon the previously mentioned layer-based fabrication of a TMP tessellation, we propose an efficient manufacturing method for constructing a tessellation using polyethylene terephthalate (PET) sheets. PET sheets maintain crease lines effectively and exhibit greater resistance to moisture and fatigue effects compared to paper. Fig. 3.5(a) displays a sample origami sheet employed to construct a TMP tessellation. The PET sheets are cut using a laser cutting machine (Universal Laser Systems) and assembled with instant adhesive (Loctite 431). As a result of the manufacturing process discussed in the prior section, Fig. 3.5(a) presents a TMP tessellation comprising six origami sheets. These long sheets form a tessellation containing eight unit cells.

In Fig. 3.5(a), red and blue lines represent PET sheets bent downwards and upwards, respectively. As noted earlier, the horizontal facets in the tessellation exhibit double wall thickness due to PET sheet attachment, while the slanted ones maintain a single thickness of the material. Such a variation in the wall thickness implies the difference in the torsional stiffness of the creases. The mathematical model developed in Section 3.3 accounts for such TMP tessellation configurations.

Analogous to a unit cell, a TMP tessellation also demonstrates considerable shape variation by altering the folding angle, as illustrated in Fig. 3.5(b). Each image in Fig. 3.5(b)

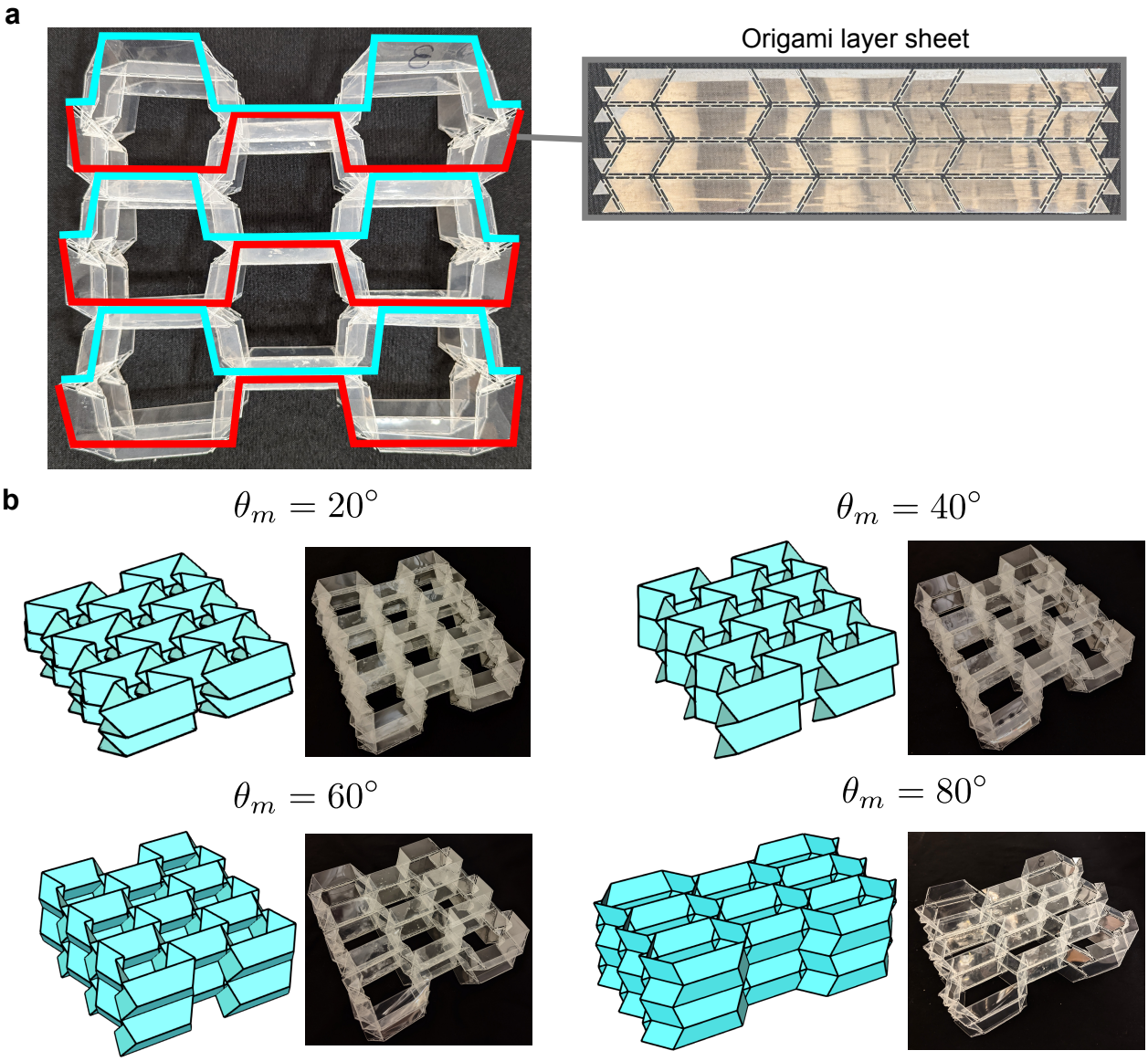

Figure 3.5: Manufactured prototype of a TMP tessellation. **a**, a TMP tessellation made of six PET sheets. Red and blue lines represent the PET sheets bent downwards and upwards, respectively. The inset of **a** shows a PET origami sheet manufactured by a laser cutter. **b**, the folding process of a TMP tessellation. Each picture corresponds to a set of images of a 3D rendering and a manufactured sample with folding angles $\theta_m = 20°$, $\theta_m = 40°$, $\theta_m = 60°$, and $\theta_m = 80°$ from top left to bottom right, respectively.

corresponds to a specific folding angle θ_m, as labeled in each panel (see Fig. 3.1(b) for the definition of θ_m).

3.2 Kinematic modeling of TMP tessellation

3.2.1 Dimensions and Poisson's ratio of TMP tessellation

We start with the analysis of the TMP tessellation in terms of the dimensions of the structure. We expand the result of the analysis of a unit cell [44] into a space-filling tessellation as shown in Fig. 3.4(c), where we define the breadth (B), height (H), and width (W) of the TMP tessellation (see the red markers for the exact boundaries). The analytical expression of these dimensions is as follows.

$$\begin{aligned} B &= 2N_B m \sin\theta_g + d\cos\theta_m \\ H &= N_H d \sin\theta_m \\ W &= \max\left(N_W\left(2l - \frac{d}{\tan\alpha}\right) - 2(N_W-1)m\cos\theta_g, 2N_W l + (N_W+1)m\cos\theta_g + \frac{d}{\tan\alpha}\right) \end{aligned} \tag{3.8}$$

Here, for the TMP tessellation, the geometrical parameters are defined as $(l, m, d, \alpha) = (28\,\text{mm}, 28\,\text{mm}, 21\,\text{mm}, 60^\circ)$. The parameter $N_H = 4$ represents the number of layers in the 3-direction for the TMP structure (see Fig. 3.4(c)). $N_B = 3$ and $N_W = 3$ represent the number of unit cells in the direction of breadth or width, respectively. Here, we only consider N_W to be odd-numbered for the symmetry of the tessellation. Folding angles θ_m, θ_g are defined in Fig. 3.1(b), and they are $\theta_m \in [0, \pi/2]$ and $\theta_g \in [0, 2\alpha]$. Based on the definition of the folding angle, the tessellation is flat-folded in the 1-3 plane when $\theta_m = \pi/2$ and in the 1-2 plane when $\theta_m = 0$. Based on the analytical expressions of the dimensions above, we

obtain the Poisson's ratios ν_{HB}, ν_{HW}, and ν_{BW} defined as follows.

$$\begin{aligned} \nu_{HB} &= -\frac{dB/B}{dH/H} \\ \nu_{HW} &= -\frac{dW/W}{dH/H} \\ \nu_{BW} &= -\frac{dW/W}{dB/B} \end{aligned} \tag{3.9}$$

3.2.2 Effective density

Based on the dimensions of the TMP tessellation, we can further obtain the properties of the tessellation. The cross-sectional area A enclosed by the tessellation is obtained as follows:

$$A = 2N_{cell} m \sin\theta_m (2l + m\cos\theta_g) \tag{3.10}$$

where $N_{cell} = N_B N_W - (N_W - 1)/2$ represents the number of the unit cells within the tessellation. Moreover, we define the volume V as the enclosed space by the outer wall of the tessellation.

$$V = AH \tag{3.11}$$

Here, to evaluate the density of the system due to the volume change of the TMP tessellation, we define the effective density ρ of the tessellation:

$$\rho = \rho_{mat} \frac{V_{mat}}{V} \tag{3.12}$$

where V_{mat} and ρ_{mat} are the volume and density of the material used to construct the tessellation, respectively. In this work, we use PET for the manufacturing of origami-based metamaterial, and the density of PET is $\rho_{mat} = 1.38 \times 10^{-3}\,\mathrm{g/mm^3}$. The volume of the material V_{mat} corresponds to the total volume of the PET sheets, and it is formulated as follows:

$$V_{mat} = N_s N_H t d \left(6l + 4m + \frac{d}{\tan\alpha}\right) \tag{3.13}$$

where $N_s = 2N_B$ is the number of origami sheets used to build the TMP tessellation, and $t = 0.25\,\mathrm{mm}$ is the thickness of PET.

3.3 Force-displacement relationship of the TMP tessellation

Now we investigate the force-displacement relationship of the tessellation. Due to the rigid foldability of TMP structures, we can adopt the model of approximating the TMP tessellation with rigid panels for facets and torsional springs along the crease lines [44]. We consider the folding motion of the TMP tessellation under an axial force F_3 in the direction of height. The axial force F_3 is expressed as follows (Details are discussed in the next section):

$$\begin{aligned} F_3 = -\frac{4}{N_H d \cos\theta_m}(l_m^s f(\theta_m, \theta_{mn}; k_1^s, k_2^s, k_3^s) + l_m^d f(\theta_m, \theta_{mn}; k_1^d, k_2^d, k_3^d) \\ + l_s \frac{\cos^3(\frac{\theta_g}{2})\sin\theta_m}{\cos\alpha \sin\theta_s} f(\theta_s, \theta_{sn}; k_1^s, k_2^s, k_3^s)) \end{aligned} \tag{3.14}$$

where l_m^s and l_m^d are the lengths of the main (horizontal) crease line with single and double sheet thickness, respectively, to take overlapping sheets introduced during the fabrication into account. Length l_s is the length of sub (inclined) crease lines with single sheet thickness. The function $f(\theta, \theta_n; k_1, k_2, k_3)$ represents the nonlinear spring function defined as follows.

$$f(\theta, \theta_n; k_1, k_2, k_3) = k_1(\theta - \theta_n) + k_2(\theta - \theta_n)^2 + k_3(\theta - \theta_n)^3 \tag{3.15}$$

Here, θ_n denotes the natural folding angle of the folding process with zero potential energy. The spring coefficients k_1^s, k_2^s, and k_3^s are for the single thickness sheets. Likewise, the spring coefficients k_1^d, k_2^d, and k_3^d are for the double thickness sheets. These spring coefficients are obtained by the bending tests on the crease lines.

Since we evaluate the mechanical property as a whole of the tessellation, the effective stress and strain in this direction can be obtained as follows:

$$\begin{aligned} \sigma_3 &= \frac{F_3}{A} \\ \epsilon_3 &= \frac{\Delta H}{H_0} \end{aligned} \tag{3.16}$$

where A is the cross-sectional area defined in the previous section, H_0 is the initial height of the tessellation, and ΔH is the amount by which the height of the tessellation changes. Furthermore, we derive Young's modulus E_3 of this metamaterial.

$$E_3 = \left.\frac{d\sigma_3}{d\epsilon_3}\right|_{\epsilon_3=0} \tag{3.17}$$

Here, Young's modulus is evaluated as the slope at the origin of the stress-strain relationship; in other words, the stiffness right after starting the compression.

3.3.1 Details of force-displacement relationship of TMP tessellations

We model the TMP tessellation as a combination of rigid panels and nonlinear torsional springs to analyze the force-displacement relationship. By applying the principle of the virtual work, we obtain the following equation,

$$F_i \delta u_i = 2(l_m^s M_m^s + l_m^d M_m^d)\delta\theta_m + 2 l_s M_s \delta\theta_s \tag{3.18}$$

where l_m^s and l_m^d are the lengths of the main (horizontal) crease line with single and double sheet thickness, respectively. l_s is the length of the sub (inclined) crease line with single sheet thickness. The length of the crease lines is obtained as follows:

$$\begin{aligned} l_m^{total} &= 6(N_H - 1)\left(4l + 6m + \frac{d}{\tan\alpha}\right) \\ l_m^d &= 14(N_H - 1)\left(2m - \frac{d}{\tan\alpha}\right) \\ l_m^s &= l_m^{total} - l_m^d \end{aligned} \tag{3.19}$$

The subscript $i = 1, 2, 3$ denotes the direction of the axis as shown in Fig. 3.2. The bending moments around the main crease lines per unit length with the single and double sheet thickness are expressed as M_m^s and M_m^d, respectively. Likewise, M_s represents the bending moment around the sub crease lines per unit length with single sheet thickness. These bending moments per unit length are obtained as follows:

$$\begin{aligned} M_m^s &= f(\theta_m, \theta_{mn}; k_1^s, k_2^s, k_3^s) \\ M_m^d &= f(\theta_m, \theta_{mn}; k_1^d, k_2^d, k_3^d) \\ M_s &= f(\theta_s, \theta_{sn}; k_1^s, k_2^s, k_3^s) \end{aligned} \tag{3.20}$$

where the function $f(\theta, \theta_n, k_1, k_2, k_3)$ is the nonlinear spring function defined as follows:

$$f(\theta, \theta_n; k_1, k_2, k_3) = k_1(\theta - \theta_n) + k_2(\theta - \theta_n)^2 + k_3(\theta - \theta_n)^3 \tag{3.21}$$

θ_0 denotes the initial folding angle of the folding process. k_1^s, k_2^s, and k_3^s are the spring coefficients for the single thickness sheets. Likewise, k_1^d, k_2^d, and k_3^d are the spring coefficients for the double-thickness sheets. These spring coefficients are obtained by the bending tests on the crease lines.

In this study, we investigate the force-displacement relationship in the 3-axis. In the direction of height, the displacement $u_3 = H_0 - H$ where H_0 is the initial height. For the variation of u_3, we obtain

$$\begin{aligned} \delta u_3 &= -\delta H \\ &= -N_H d cos\theta_m \delta\theta_m \end{aligned} \tag{3.22}$$

Finally, we obtain the force-displacement relationship in the 3-axis as follows:

$$\begin{aligned} F_3 = -\frac{4}{N_H d\cos\theta_m}(l_m^s f(\theta_m, \theta_{mn}; k_1^s, k_2^s, k_3^s) + l_m^d f(\theta_m, \theta_{mn}; k_1^d, k_2^d, k_3^d) \\ + l_s \frac{\cos^3(\frac{\theta_g}{2})\sin\theta_m}{\cos\alpha\sin\theta_s} f(\theta_s, \theta_{sn}; k_1^s, k_2^s, k_3^s)) \end{aligned} \tag{3.23}$$

3.3.2 Measurement of the crease line stiffness coefficient

We conduct bending tests on our crease line designs to measure their spring constants. The setup for the experiment is presented in Fig. 3.6(a). The sample of the crease line is attached to the load cell (LUX-B-50N-ID, Kyowa) with 3D printed fixtures. We force vertical compression via the linear stage (BiSlider, Velmex). We model the sample of the crease line with two rigid panels connected by a nonlinear torsional spring as shown in Fig. 3.6(b). Then, the force-displacement relationship is modeled as follows:

$$\begin{aligned} F &= \frac{2L_{cr} f(\theta, \theta_n; k_1, k_2, k_3)}{L\cos\theta} \\ f(\theta, \theta_n; k_1, k_2, k_3) &= k_1(\theta - \theta_n) + k_2(\theta - \theta_n)^2 + k_3(\theta - \theta_n)^3 \end{aligned} \tag{3.24}$$

where L_{cr} is the length of the crease line, L is the length of the sample, θ is the folding angle, and θ_n is the natural folding angle. Also, k_1, k_2, and k_3 are the nonlinear spring coefficients. By applying the curve-fitting algorithm to the result of the compression test

shown in Fig. 3.6(c), we obtain the nonlinear spring constants k_1, k_2, and k_3. Finally, we obtain the spring coefficients, $k_1^s = 0.169$N/rad, $k_2^s = 0.0782$N/rad, and $k_3^s = 0.0412$N/rad for the single-thickness crease line. Moreover, we obtain $k_1^d = 0.505$N/rad, $k_2^d = 0.220$N/rad, and $k_3^d = 0.116$N/rad for the double-thickness crease line.

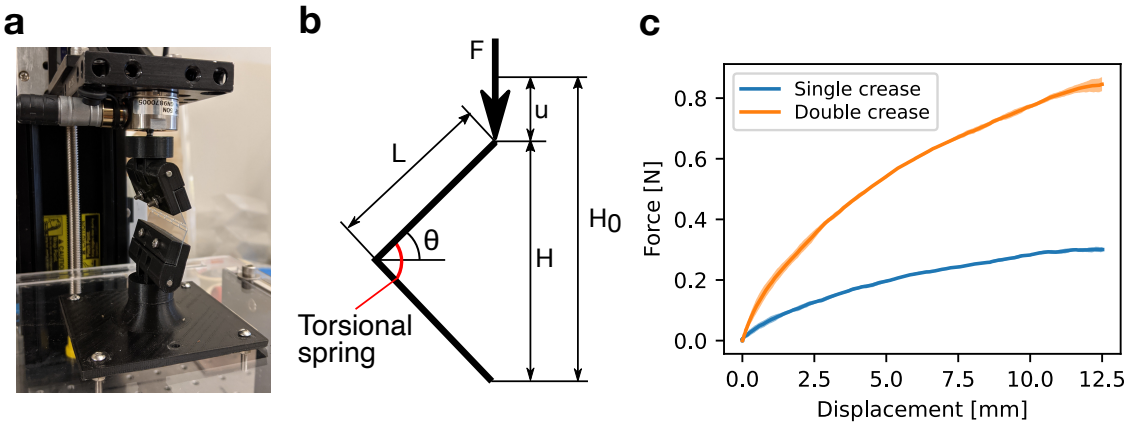

Figure 3.6: Setup of the bending test to measure the spring constant of the crease line. **a**, the photograph of the experimental setup for the crease line sample. **b**, the analytical model of the bending test of the crease line. The model is composed of two rigid panels and a nonlinear torsional spring. **c**, the result of the compression tests for the single-thickness crease line (blue) and double-thickness crease line (orange). The solid lines represent the mean values, whereas the colored area represents the standard deviation from the five experiments.

3.4 Post-fabrication tuning of a TMP tessellation and experimental process

The force-displacement relationship depends not only on the design parameters of the TMP tessellation but also on its natural posture (see Eq.(3.15)). This natural posture is represented by the natural folding angle θ_{mn}, which is the dihedral angle between facets measured at a zero-energy state (i.e., without external forces). Fig. 3.7(a) shows the same TMP tessellation, but in two different zero-energy states, which tend to show different force-displacement behavior (see Fig. 3.7(c)). To exploit this feature for tunability in TMP-based metama-

terials, we employ a heat-processing method using a convection heat oven to modify the natural folding angle of the origami structure, as schematically depicted in Fig. 3.7(b). Prior research has generally proposed two directions for heat-processing techniques: active actuation of origami structures using heat-activated materials like polyvinyl chloride (PVC) films [17] and shape memory composites [73], and passive control of mechanical properties through heat annealing [74].

We extend the heat annealing method for tuning the properties of origami mechanical metamaterials. We place the sample in a convection oven (Despatch), secure it in the desired posture, heat the structure to 80°C for four hours, and allow it to cool to room temperature. Fig. 3.7(b) displays examples of heat-processed outcomes. The samples, manufactured with identical geometric parameters, exhibit different natural folding angles due to heat processing. Owing to the nonlinearity of the TMP tessellation's force-displacement relationship, multiple responses can be achieved from one tessellation, as illustrated in Fig. 3.7(c).

To investigate the broad range of Young's modulus achievable through compression tests with varying natural folding angles of the TMP tessellations, we conduct compression tests on the manufactured sample using the aforementioned tuning method. We construct an experimental setup with low-friction plates (Delrin®) and a linear stage for axial compression tests to capture the force-displacement relationship, as demonstrated in Fig. 3.7(c). We apply the heat process to a single fabricated sample, stage by stage, allowing us to achieve multiple natural folding angles using just one structure. For each stage, we perform a compression test to observe varying Young's modulus from one structure.

3.5 Heat processing to control the natural folding angle of TMP tessellation

To control the natural posture of the TMP tessellation, we employ heat-processing to the sample of TMP tessellation. We put the sample in the convection oven (LAC 1-38A-4, Despatch) with an aluminum frame to control the height of the structure as shown in Fig. 3.8(a). Then we apply the heat of 80 °C for four hours and cool the sample down to room temperature. The result of the heat processing is shown in Fig. 3.8(b). The sample

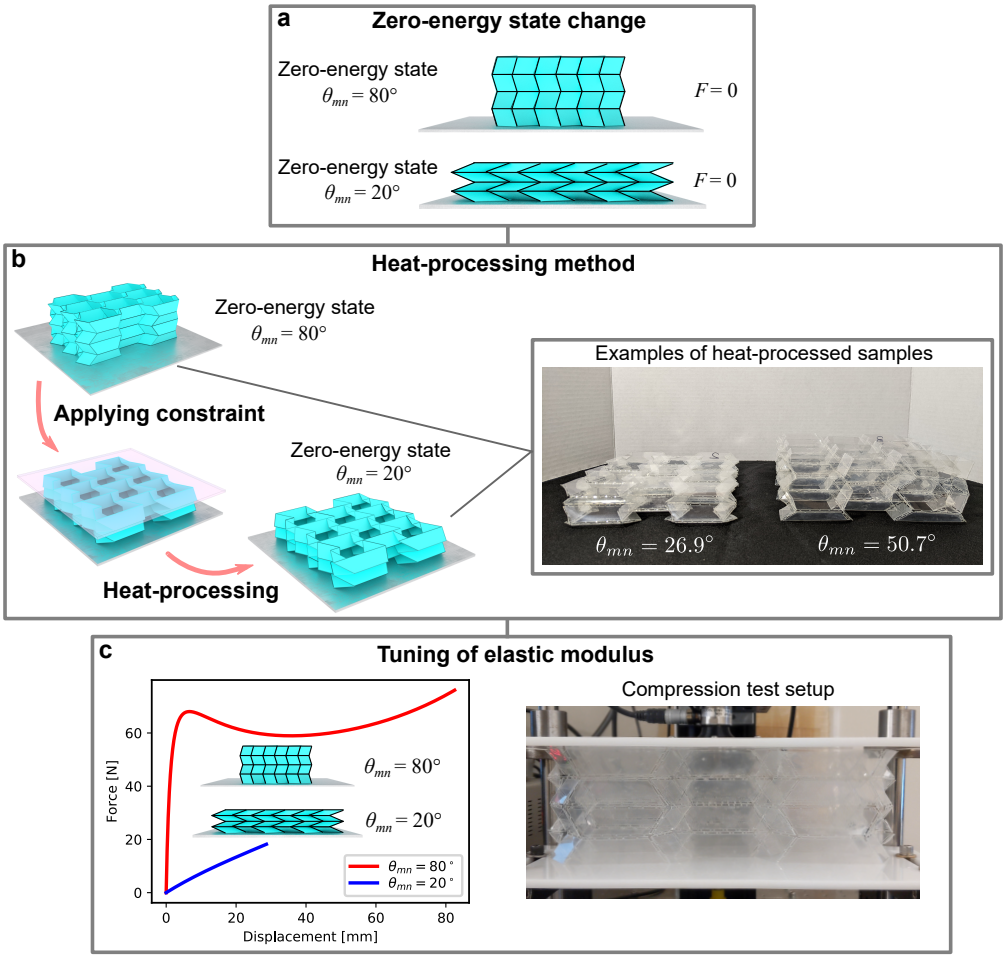

Figure 3.7: Schematic figures of the post-fabrication tuning of TMP tessellation. **a**, schematic illustration of the change of the zero-energy state of TMP tessellation with two different natural folding angles. **b**, schematic illustration of the heat-processing method to change a natural folding angle of TMP structure. The inset in **b** shows two heat-processed samples with different natural postures. The left sample has a height of 38 mm ($\theta_{mn} = 26.9°$), and the right sample has a height of 65 mm ($\theta_{mn} = 50.7°$). **c**, the schematic force-displacement relationship based on the two different natural folding angles ($\theta_{mn} = 20°$ and $\theta_{mn} = 80°$). The inset in **c** shows the experimental setup to measure the force-displacement relationship and elastic modulus of the manufactured sample.

on the left is controlled to the height of 38 mm and the one on the right is controlled to 65 mm. These results show that we can achieve the desired initial posture of TMP tessellation through heat processing.

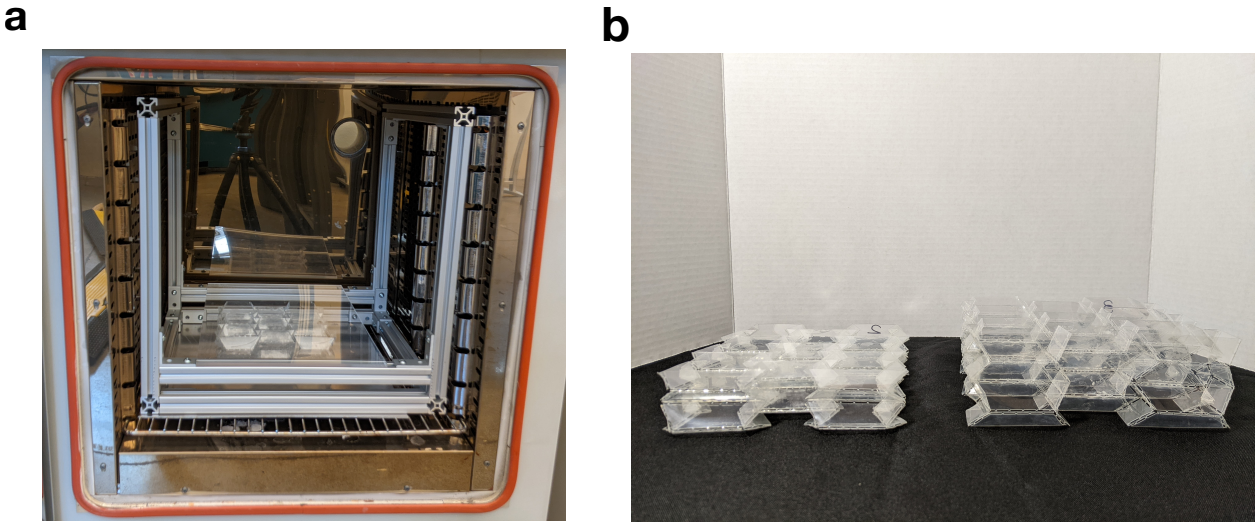

Figure 3.8: Overview of the heat process on the TMP samples to control the natural posture. **a**, a convectional oven, and the sample of the TMP tessellation with an aluminum frame to fix the posture. **b**, two heat-processed samples with different natural postures.

3.5.1 Compression test on the TMP tessellation

To observe the force-displacement relationship and Young's modulus of the TMP tessellation, we perform the compression tests on a sample of TMP tessellation. The setup of the compression test is shown in Fig. 3.9. The sample made of PET is compressed between two panels of low-frictional Derlin plates with the Velmex linear stage. The force is measured with the Kyowa load cell. The results of the compression tests are shown in Fig. 3.10 and Fig. 3.11. Here, the natural folding angle of the tessellation is tuned by the aforementioned heat processing method. The range of tuning is from $\theta_{mn} = 77.9°$ to $\theta_{mn} = 26.9°$, applied to one fabricated sample stage by stage. We observe the slope at the origin where there

is a good agreement between analysis and experiment to obtain Young's modulus of this metamaterial. The result of the experiments is summarized in the main article.

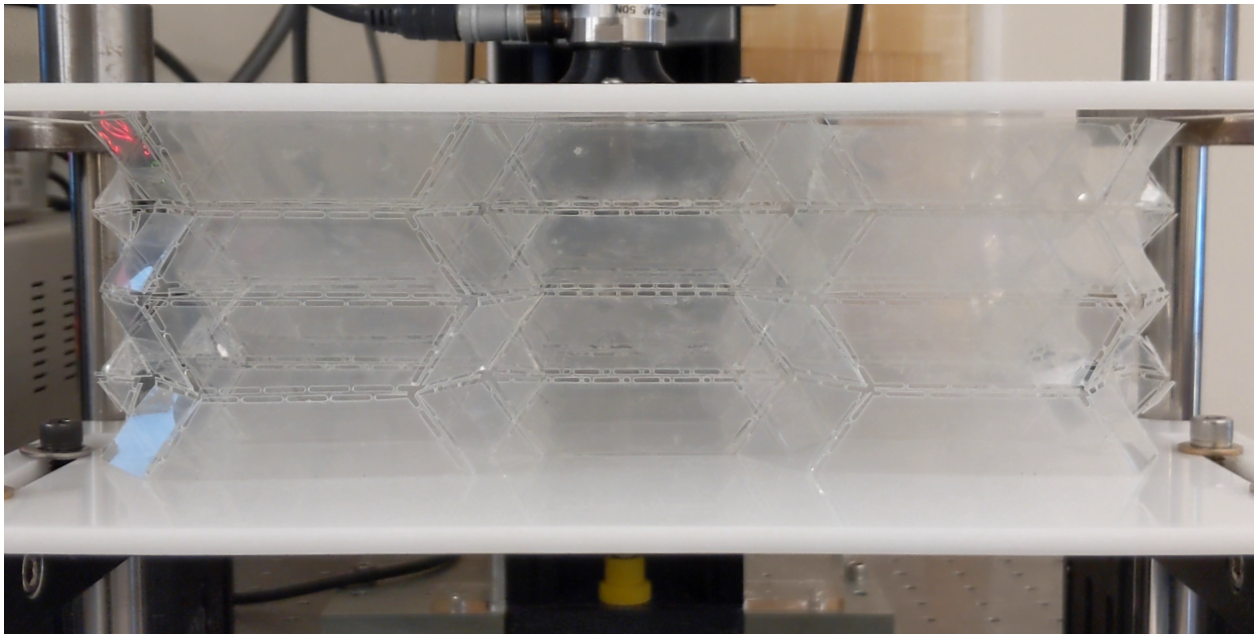

Figure 3.9: Setup of the compression tests on the TMP tessellation samples. The sample is compressed between two low-frictional Derlin plates with a linear stage.

3.5.2 Measurement of dimensions of a TMP tessellation sample

To verify the analytical model of the dimensions of TMP tessellations, we perform measurements on the manufactured sample of the TMP tessellation. The experimental setup is shown in Fig. 3.12. We construct a jig so that we can fix the height of the sample with a transparent acrylic plate as shown in Fig. 3.12(a). We measure the breadth (B), width (W) with a different height (H) controlled by the jig. To measure breadth and width, we use a ruler on top of the transparent plate as shown in Fig. 3.12(b). The measurement was conducted three times for each height.

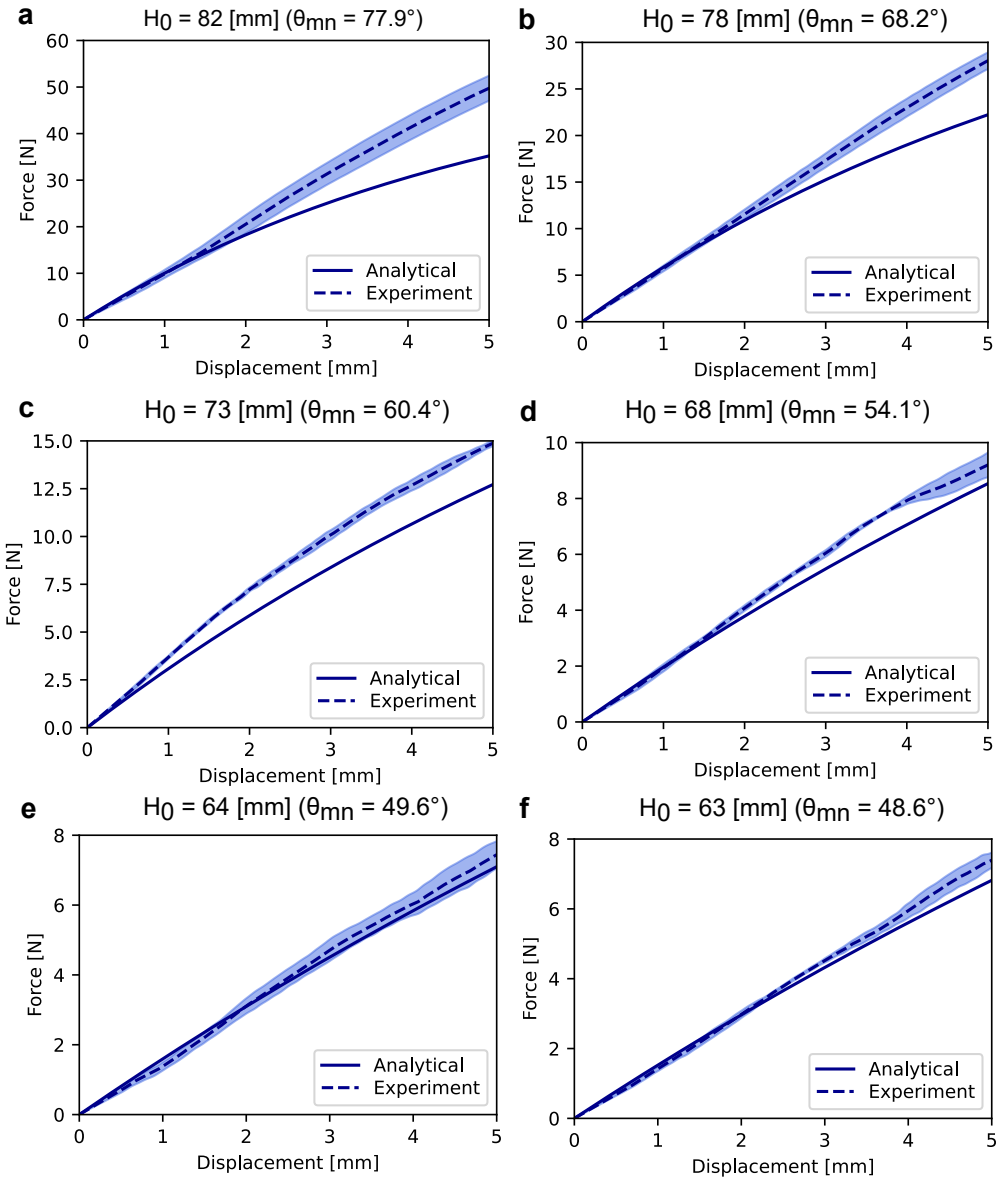

Figure 3.10: The first part of the results of the compression tests with various natural heights. Blue solid lines represent the analytical data, whereas dashed lines and color-shaded areas depict the mean values and standard deviation of the experiments that are executed three times.

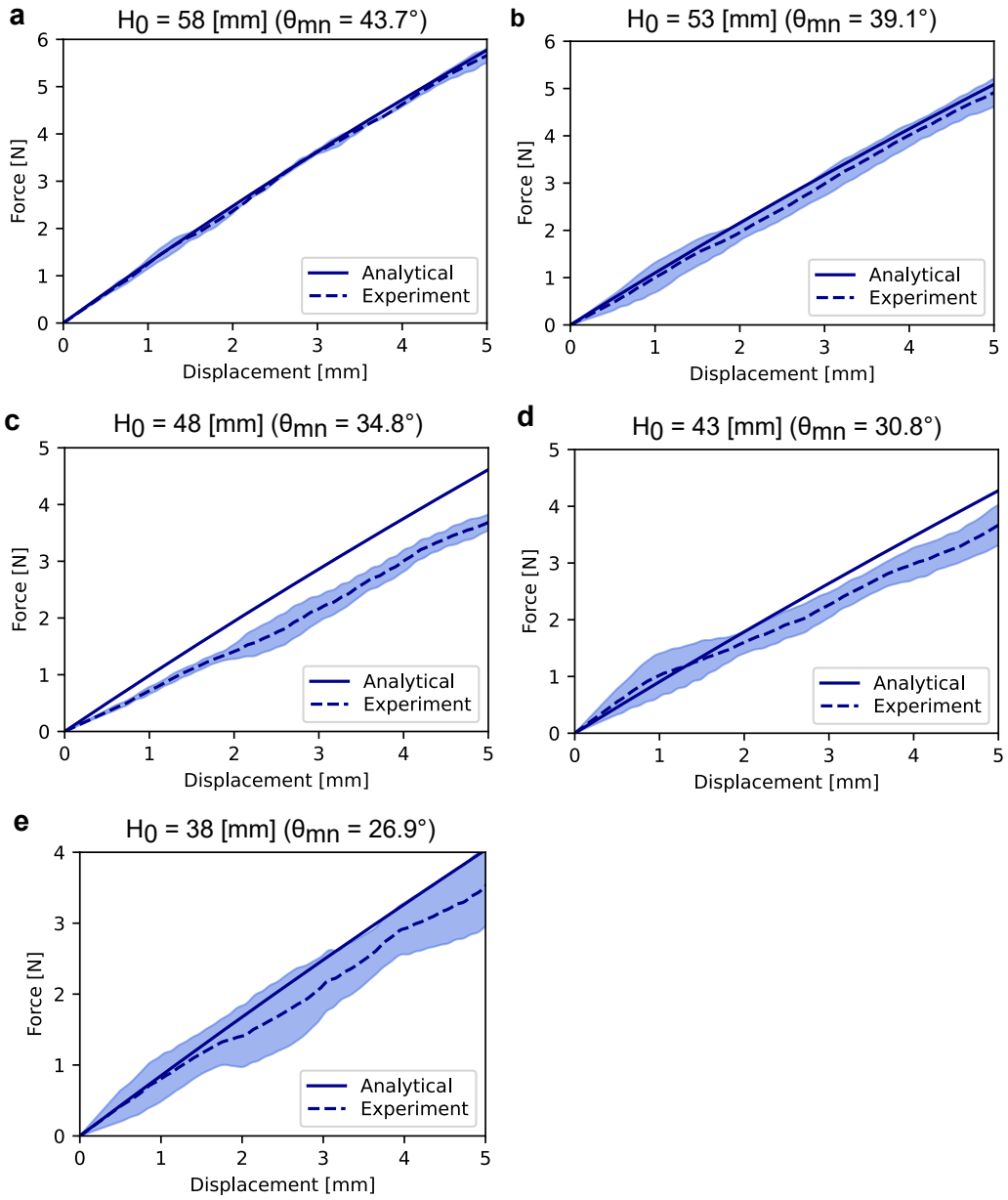

Figure 3.11: The second part of the results of the compression tests with various natural heights. Blue solid lines represent the analytical data, whereas dashed lines and color-shaded areas depict the mean values and standard deviation of the experiments that are executed three times.

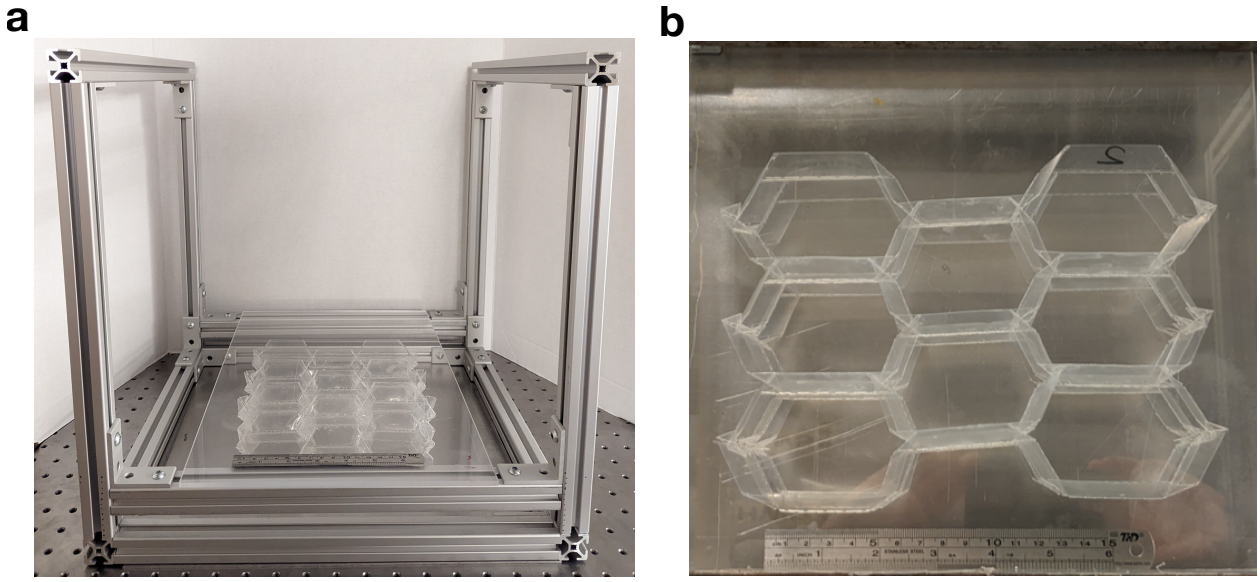

Figure 3.12: Experimental setup of the measurement of the dimensions of the manufactured TMP sample. **a**, the overview of the experimental setup for the measurement of the TMP tessellation sample. **b**, the view from the top side of the setup.

3.6 Results and discussion

3.6.1 Kinematic analysis and effective density

First, we examine the change in dimensions as a function of the folding angle θ_m. We compress the structure using a transparent acrylic plate and measure the dimensions. Fig. 3.13(a) presents three dimensions (W, B, and H) of a TMP tessellation, revealing a significant change in dimensions between the two flat stages ($\theta_m = 0°, 90°$). Based on these dimensions, we calculate the tessellation's volume, as shown in Fig. 3.13(b). Similarly, by incorporating the density, we estimate the effective density of the tessellation, as demonstrated in Fig. 3.13(c). Both volume and density exhibit considerable changes. However, since the analysis relies on the rigid origami assumption, in which panel thickness is assumed to be zero, the analysis may be invalid when the folding angle is close to 0° or 90°. To avoid unrealistic analysis, we restrict the range of the analysis to between 20° and 80°. Within this analysis range, we find that the experimental results and the analysis are in good agreement, as illustrated in Fig. 3.13(a)-(c).

3.6.2 Poisson's ratio

We examine the Poisson's ratio of a TMP tessellation. Poisson's ratios are derived from three dimensions - height, breadth, and width - and represented as ν_{HB}, ν_{HW}, and ν_{BW} based on Eq.(3.9), as depicted in Fig. 3.14(a)-(c). Here, we present both analytical results derived from Eq.(3.9) and experimental measurements of the dimensions, denoted by blue solid lines and red circle symbols, respectively. Due to the non-smooth change in width measurements, we observe discontinuity in Poisson's ratios ν_{HW} and ν_{BW}.

Poisson's ratios exhibit anisotropy in each pair of dimensions. Poisson's ratio ν_{HB} ranges from slightly negative values to highly positive values. Poisson's ratio ν_{HW} demonstrates negative values throughout the folding process. Poisson's ratio ν_{BW} displays a wide range in both negative and positive regions. Here, around $\theta_m = 50°$ in Fig. 3.13(a), B becomes insensitive to θ_m with showing the flat region in the graph. Therefore, dB, the infinitesimal

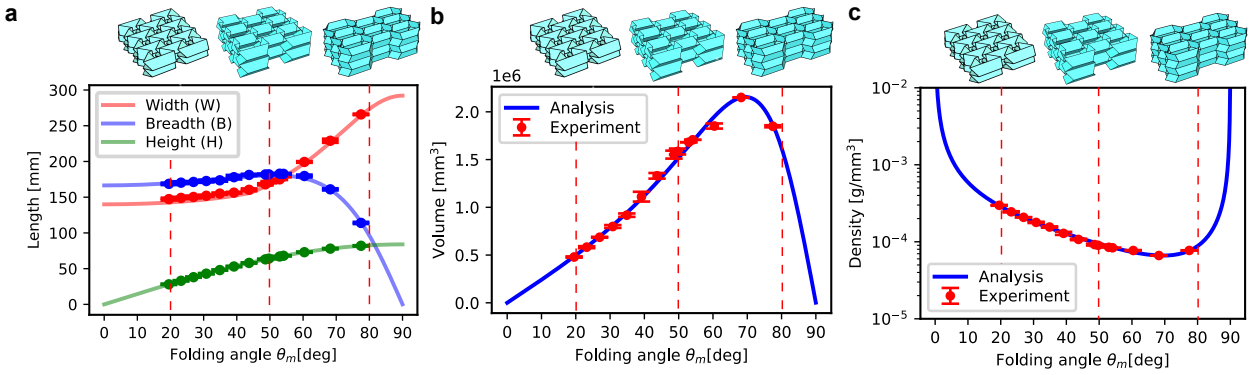

Figure 3.13: Theoretical analysis and experiments on a kinematic modeling of a TMP tessellation. **a**, the three dimensions of the tessellation, W, B, and H. **b**, the volume of the tessellation. **c**, the effective density of the tessellation. Curves represent theoretical predictions based on analysis, while discrete dots and bars denote the average and standard deviation of the measurements, respectively.

difference of B, reaches zero. This introduces the singularity in ν_{BW} where it becomes positive or negative infinite. In the experimental verification process, we can confirm that ν_{BW} ranges from -40 to 20 with this definition of Poisson's ratio, as shown in Fig. 3.14(c). These findings are consistent with Poisson's ratios of TMP unit cells reported in a previous study [44]. Furthermore, they demonstrate the rich anisotropy and extensive range of Poisson's ratio, with a strong agreement between the analysis and experiment.

3.6.3 Elastic modulus

In this section, we examine the force-displacement relationship and Young's modulus of a TMP tessellation both theoretically and experimentally. Fig. 3.15 presents the theoretical and experimental force-displacement relationships for three representative natural folding angles: $\theta_{mn} = 77.9°$ ($H_0 = 82$ mm), $\theta_{mn} = 49.6°$ ($H_0 = 64$ mm), and $\theta_{mn} = 39.1°$ ($H_0 = 53$ mm). The analytical results are obtained using Eq. (3.14). We observe a significant

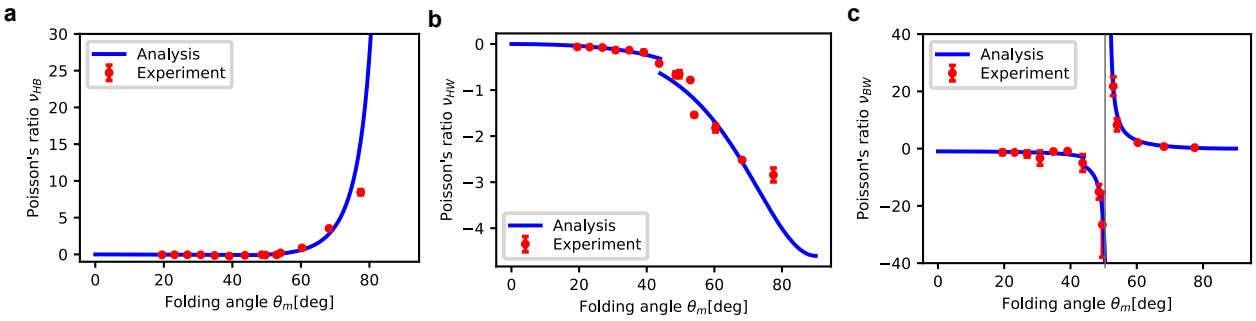

Figure 3.14: Poisson's ratio of a TMP tessellation. **a**, Poisson's ratio ν_{HB}. **b**, Poisson's ratio ν_{HW}. **c**, Poisson's ratio ν_{BW}. Blue solid lines in **a** - **c** represent theoretical analysis. Red dots in **a** - **c** represent the mean values of the experiment. Red bars in **a** - **c** represent the standard deviation of the experiment. Grey vertical line in **c** represents the singular point of ν_{BW} where B becomes insensitive to θ_m (see Section 3.2 for the details).

difference in the force-displacement relationship depending on the natural folding angle, and the stiffness measured at the origin in Fig. 3.15 varies considerably with the tuning of the natural folding angle. Based on these findings, we calculate the effective stress and strain of the TMP tessellation using Eq. (3.16) and subsequently determine Young's modulus of the tessellation as formulated in Eq. (3.17). The change of Young's modulus with respect to natural folding angles is discussed in the next section. In addition to these three natural folding angles, we examine eight more natural folding angles and obtain Young's modulus for each angle.

3.6.4 Visualization and analysis of tunability via 3D Ashby chart

The analysis and experiments on effective density (Section 3.6.1), Poisson's ratio (Section 3.6.2), and Young's modulus (Section 3.6.3) yields three-dimensional Ashby charts, as shown in Fig. 3.16(a)-(c). The inset in Fig. 3.16(a) displays a two-dimensional Ashby chart with effective density and Young's modulus. This 2D Ashby chart is common in Fig. 3.16(a)-(c) since the only difference in Fig. 3.16(a)-(c) is Poisson's ratio (ν_{HB}, ν_{HW}, and ν_{BW}). These

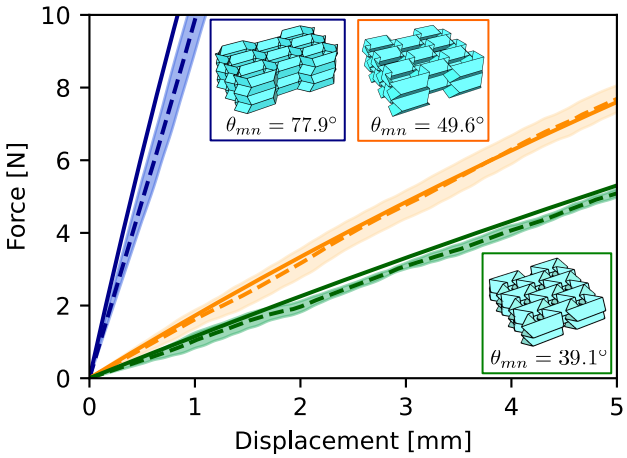

Figure 3.15: Force-displacement relationship and elastic modulus of a TMP tessellation. Blue, orange, and green solid lines represent a theoretical force-displacement relationship with three different natural folding angles $\theta_{mn} = 77.9°$, $\theta_{mn} = 49.6°$, and $\theta_{mn} = 39.1°$, respectively. Dashed lines and color-shaded areas for each color depict the mean values and standard deviation of the experiments that are executed three times.

plots reveal the remarkable properties of this mechanical metamaterial, with approximately a 60-time difference in Young's modulus and a 10-time difference in density. The wide range of Young's modulus, effective density, and positive/negative anisotropic Poisson's ratio highlights the tunability of TMP origami-based mechanical metamaterials.

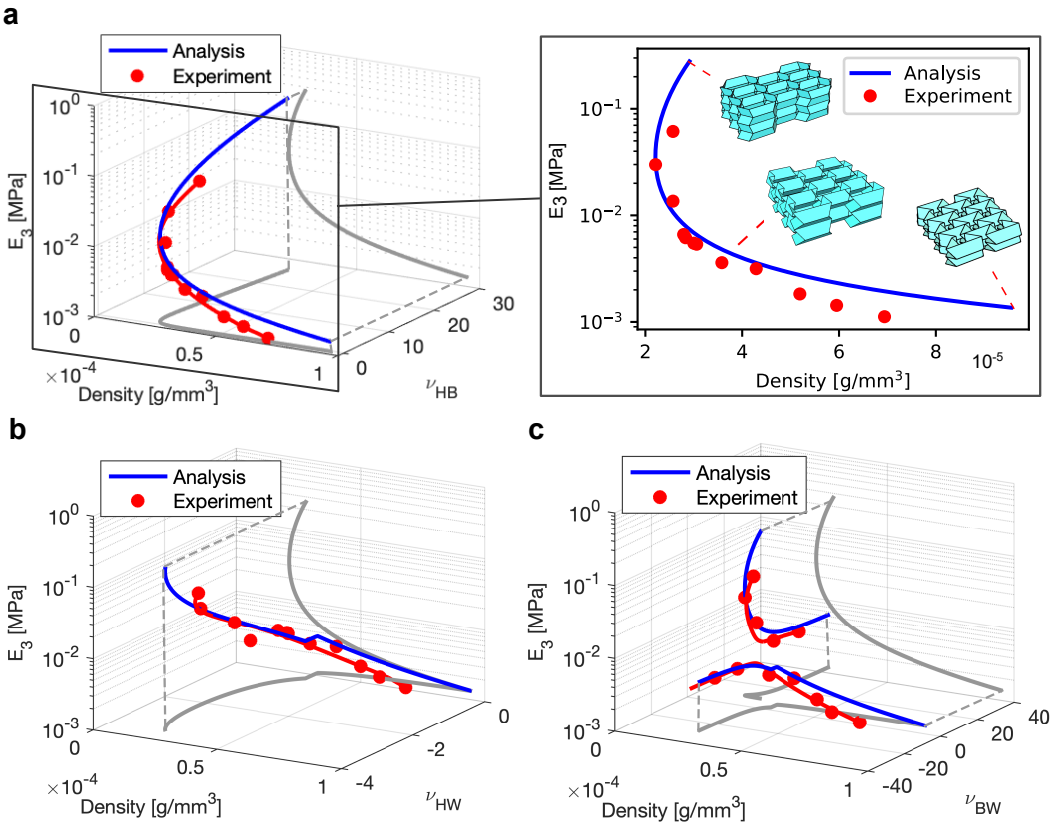

Figure 3.16: Three-dimensional Ashby chart of a TMP tessellation. **a**, three-dimensional Ashby chart with effective density, Young's modulus, and Poisson's ratio ν_{HB}. The inset of **a** depicts the two-dimensional Ashby chart of effective density and Young's modulus. **b**, three-dimensional Ashby chart with effective density, Young's modulus, and Poisson's ratio ν_{HW}. **c**, three-dimensional Ashby chart with effective density, Young's modulus, and Poisson's ratio ν_{BW}. Red dots in **a** - **c** represent the mean values of the experiment. Red solid lines in **a** - **c** depict polynomial fitting to the experiment data. Gray lines in **a** - **c** represent the two-dimensional projections of the three-dimensional curves.

Moreover, we observe a unique behavior where the origami metamaterial's effective density and Young's modulus are inversely correlated, which is uncommon in traditional materials. Conventional materials tend to show stiffer behavior as their density increases. However, our TMP-based metamaterial can be designed to exhibit enhanced stiffness even under a reduced effective density. This is a highly desirable characteristic for constructing lightweight yet stiff structures. Remarkably, this unique property is the outcome of rigid-foldable kinematics of the TMP system, without relying on any plastic, self-locking, and/or external actuation mechanisms. The good agreement between the analysis and experiment presents the ability to predict the mechanical properties to design a tuning process to meet users' requirements.

These three-dimensional Ashby charts indicate that TMP, a 3D voluminous origami element, can serve as a building block for designing mechanical metamaterials with desired mechanical properties in terms of effective density, Young's modulus, and positive/negative anisotropic Poisson's ratio. This is achieved through a simply-fabricated single sample by applying heat processing to control the natural folding angle.

3.7 Conclusion

In this study, we showcase the extensive post-fabrication tunability of the TMP tessellation through theoretical analysis and experimental verification. Tailoring mechanical metamaterials after fabrication concerning three representative mechanical properties—effective density, Poisson's ratio, and Young's modulus—has been a long-standing and challenging problem. To this end, we propose and construct a prototype of an origami-based mechanical metamaterial featuring the TMP architecture. The rigid foldable nature of this TMP prototype enables an accurate prediction of these fundamental mechanical properties based on simple kinematic analysis. We employ the heat processing method to control the natural posture of the tessellation, achieving the desired properties.

The simplicity of modeling this metamaterial, assuming the structure consists of rigid panels and nonlinear torsional springs, enables us to visualize its extensive design space. We

adopt the Ashby chart concept for visualization. Traditionally, the Ashby chart utilizes two material properties; however, we extend this approach to three-dimensional plots incorporating effective density, Young's modulus, and Poisson's ratio. Moreover, we experimentally verify this design space using a novel manufacturing scheme inspired by honeycomb structures. The agreement between analysis and experimentation suggests abundant opportunities to tailor these metamaterials according to users' engineering requirements. Furthermore, we observe the unique behavior of this origami-based metamaterial, where effective density decreases while Young's modulus increases.

In conclusion, the versatility of this origami-based metamaterial offers significant potential for transforming and adapting its mechanical properties to rapidly changing external environments after fabrication. TMP-based metamaterials stand out from previous research on space-filling mechanical metamaterials with lattice-based or origami-based architectures in terms of their extensive tunability, flat foldability, auxeticity, the inverse correlation between effective density and Young's modulus. Although we have explored uniform homogeneous architectures, we envision the possibility of locally tuning properties using the same units, which constitutes one of our future tasks. The dimensionless working principle of TMP metamaterial enables its application on both large scales, such as space structures and automotive airbags, and small scales, like the micro-structure of artificial bones (meta-implants [56]). Furthermore, while we consider the linear-elastic region in this chapter, combining post-fabrication tuning, nonlinear finite element analysis, and data-driven design of metamaterials [75, 76] can unlock the full potential of this metamaterial. The broad tunability of mechanical properties offers further possibilities for employing this metamaterial as a highly adaptable engineering platform.

3.8 Author contributions

This chapter is based on the paper: K. Yamaguchi, Y. Miyazawa, H. Yasuda, Y. Song, S. Shimokawa, U. Gandhi, J. Yang, "Post-fabrication tuning of origami-inspired mechanical metamaterials based on Tachi-Miura polyhedron," Materials & Design 233 (2023) 112170.

[34]. K.Y, H.Y, and J.Y conceived the idea of this project. The numerical studies, experiments, and original draft writing were carried out by K.Y. K.Y, Y.M, H.Y, Y.S, S.S, U.G, and J.Y contributed to the review and editing of the manuscript. J.Y supervised the project. All authors contributed to the paper with valuable inputs.

Chapter 4

CONTROLLABILITY ANALYSIS OF ORIGAMI DYNAMICS VIA STATE-SPACE MODELING

In the previous chapters (Ch. 2 and 3), we focused on the schematic, combinatorial, and static mechanical properties of origami-based mechanical metamaterials. However, with the rising research interest in the utilization of origami for robotics [35, 36, 37, 39, 40, 41], it is now essential to investigate their dynamics, develop control models, and adopt a control-aware design approach. In this chapter, we address the challenge of controlling the transient dynamics of flexible origami structures by developing a framework to analyze their controllability, focusing on the efficient deployment of Miura-ori cells [33]. We discretize the origami system into a bar-and-hinge model and derive its state-space representation to model its dynamics. Using this model, we employ the controllability Gramian to systematically calculate the minimum control energy required for deployment, thereby ranking the efficiency of placing an actuator on any given crease line. Our computational predictions for optimal actuator placement in single, two-cell, and four-cell configurations are validated through experiments with servo-actuated stainless steel prototypes, where the theoretical rankings of deployment efficiency show strong agreement with measured control effort. Furthermore, we extend the analysis to large deformations using a piecewise-affine linearization approach, demonstrating its applicability beyond small-displacement scenarios. Our primary contribution is a computational and experimentally-verified framework that bridges origami dynamics and control theory, providing a systematic method for designing and operating efficient actuation systems for complex, deployable origami structures in fields like robotics and aerospace engineering.

4.1 Geometry of Miura-ori unit cell and tessellation

We present a Miura-ori unit cell, a two-cell pattern, and a four-cell pattern in Fig. 4.1. In Fig. 4.1(a), we define the length of the dimensions of the parallelogram facet with the lengths a and b, and acute angle α. Assuming rigid foldability (i.e., folding occurs only along crease lines, while facets remain rigid), the outer dimensions H, S, L, and V are determined from those three design parameters and folding angle $\theta \in [0, \pi/2]$. Here, the angle θ is the dihedral angle between the facet and the x-y plane as shown in Fig. 4.1(b). Similarly, the dimensions of two-cell and four-cell patterns are presented in Fig. 4.1(c) and (d), respectively. Based on this origami architecture, the folding process of a unit cell from the flat state to the folded state is presented in Fig. 4.1(e). The outer dimensions are analytically expressed as follows [33]:

$$\begin{aligned} H &= a \sin\theta \sin\alpha \\ S &= b \frac{\cos\theta \tan\alpha}{\sqrt{1 + \cos^2\theta \tan^2\alpha}} \\ L &= a\sqrt{1 - \sin^2\theta \sin^2\alpha} \\ V &= b \frac{1}{\sqrt{1 + \cos^2\theta \tan^2\alpha}}. \end{aligned} \tag{4.1}$$

The analysis above is based on the rigid foldable assumption, resulting in a single degree of freedom deployment of the Miura-ori cells. Ideally, this kinematic relationship is valid when the creases are highly compliant and the facets remain rigid. However, if origami structures are tessellated and undergo deformation in a dynamic situation, this rigid-foldable assumption no longer applies. For example, local actuation of a large Miura-ori tessellation may not induce global folding or unfolding — and may even lead to jamming — due to factors such as elastic or plastic deformation, friction, and damping. Therefore, to accurately predict the behavior of Miura-ori structures under realistic conditions, a practical and robust model that captures their non-rigid, dynamic nature is essential.

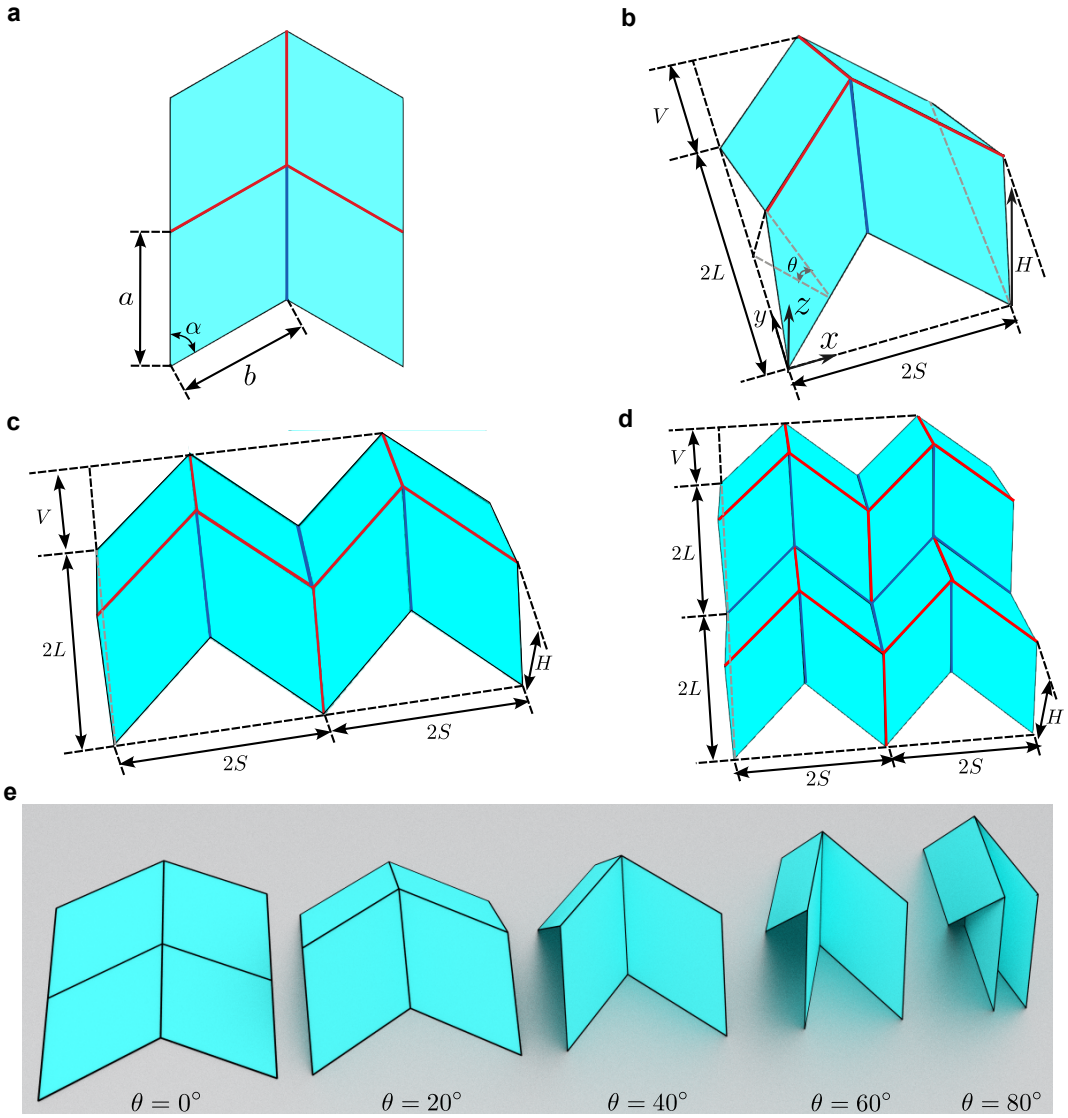

Figure 4.1: Geometry of a Miura-ori unit cell. **a**, top view of a Miura-ori unit cell in a flat state. The unit cell geometry can be determined by design parameters a, b, and α. **b**, definitions of the outer dimensions (H, S, L, and V) of a Miura-ori unit cell. The angle θ is the dihedral angle between the x-y plane and a facet. **c** and **d**, the dimensions of two-cell and four-cell Miura-ori tessellations, respectively. Adjacent unit cells in this illustration **c** and **d** have the same folding angle. Red and blue lines in **a-d** represent the mountain and valley folds, respectively. **e**, the folding process of a Miura-ori unit cell.

4.2 Bar-and-hinge modeling of the Miura-ori unit cell

To analyze the dynamics of the aforementioned Miura-ori unit cell, we utilize the bar-and-hinge model. The bar-and-hinge model is a prevalent reduced-order mechanical model to represent the behavior of origami structures [54, 77] because these models have a simple formulation and are computationally efficient. Compared to the kinematics-based simulations, where the facets are assumed to be rigid [44], the bar-and-hinge model can capture the richer global response and deformation of origami structures to be simulated.

Recent advances in the bar-and-hinge model also include the study of the dynamics of origami [30, 78]. To this end, by assigning particle mass to the nodes of the model, we can represent the mass distribution of origami structures. In this formulation, the nodal position, velocity, and acceleration describe the whole behavior of an origami structure. The dynamic response of a Miura-ori structure via the bar-and-hinge model has been previously investigated [78]. While their study focuses on the dynamics of origami structures, we aim to fill the gap between the origami dynamics itself and the model-based control theory of origami based on the bar-and-hinge model.

4.2.1 Model setup

We discretize a Miura-ori unit cell with five nodes and eight edges per facet of a Miura-ori as shown in Fig. 4.2(a), as the previous research work shows this modeling can achieve high accuracy while remaining efficient [54]. We assign bar elements, hinge elements, and nodal masses along vertices, facets, and crease lines within a structure. Here, bar elements capture the in-plane stretching and shear, whereas the hinge elements capture the out-of-plane bending of panels and bending along crease lines. Although the element type is the same, hinge elements for facets and crease lines are designed to have different rotational spring stiffness. Generally, the stiffness for crease lines is much lower than that of facets. The methods to obtain these stiffness values are explained in the subsequent sections.

In this finite particle formulation, the governing equation of motion of an arbitrary node

i can be expressed as follows [78]:

$$m_i \ddot{\boldsymbol{d}}_i = \boldsymbol{f}_i^{\mathrm{i}} + \boldsymbol{f}_i^{\mathrm{e}} + \boldsymbol{f}_i^{\mathrm{d}}, \tag{4.2}$$

where m_i is the nodal mass, $\boldsymbol{d}_i \in \mathbb{R}^3$ is the nodal displacement vector, $\boldsymbol{f}_i^{\mathrm{i}} \in \mathbb{R}^3$, $\boldsymbol{f}_i^{\mathrm{e}} \in \mathbb{R}^3$, and $\boldsymbol{f}_i^{\mathrm{d}} \in \mathbb{R}^3$ are internal, external, and damping force vector, respectively. Here, in the dynamic analysis of the origami bar-and-hinge model, we take viscous damping into account. The damping force is described as $\boldsymbol{f}_i^{\mathrm{d}} = -\zeta m_i \dot{\boldsymbol{d}}_i$, where $\dot{\boldsymbol{d}}_i$ is the nodal velocity vector and ζ is the damping parameter.

In this study, we impose boundary conditions on the Miura-ori structures to reflect the physical constraints for experimental implementation, where the leftmost side is fixed. Thus, for example, in a unit-cell setting, the equations of motion for Node 1 in the x, y, and z directions, as well as for Node 7 in the x and z directions, are constrained and removed (see Fig. 4.2(a)). For the two-cell and four-cell tessellations, the corner node in the bottom-left is fixed in all directions, and the other nodes along the leftmost side are constrained in the x and z directions.

Based on the bar-and-hinge model, the internal force vector $\boldsymbol{f}_i^{\mathrm{i}}$ can be described as follows:

$$\boldsymbol{f}_i^{\mathrm{i}} = \boldsymbol{f}_i^{\mathrm{b}} + \boldsymbol{f}_i^{\mathrm{h}}, \tag{4.3}$$

where $\boldsymbol{f}_i^{\mathrm{b}} \in \mathbb{R}^3$ is from bar elements, and $\boldsymbol{f}_i^{\mathrm{h}} \in \mathbb{R}^3$ is from rotational spring elements for facets and crease lines, respectively. To develop a linear time-invariant state-space model for a Miura-ori unit cell, we need to obtain a linearized stiffness matrix that establishes the relationship between nodal forces $\boldsymbol{f}_i$ and small displacements $\boldsymbol{d}_i$ around the natural state of the structure. The formulation of these forces is described in the following sections.

To obtain the nodal mass m_i, the mass of each triangular section in the discretized Miura-ori model is evenly distributed among constituting three nodes:

$$m = \frac{1}{3} ST\rho, \tag{4.4}$$

where ρ is the density of the material, S is the area of a triangular section, T is the thickness

of the section. In our discretization scheme of a Miura-ori, the area S is described as follows:

$$S = \frac{1}{4} ab \sin \alpha. \tag{4.5}$$

This mass m is superimposed for each triangular section to calculate the nodal mass m_i.

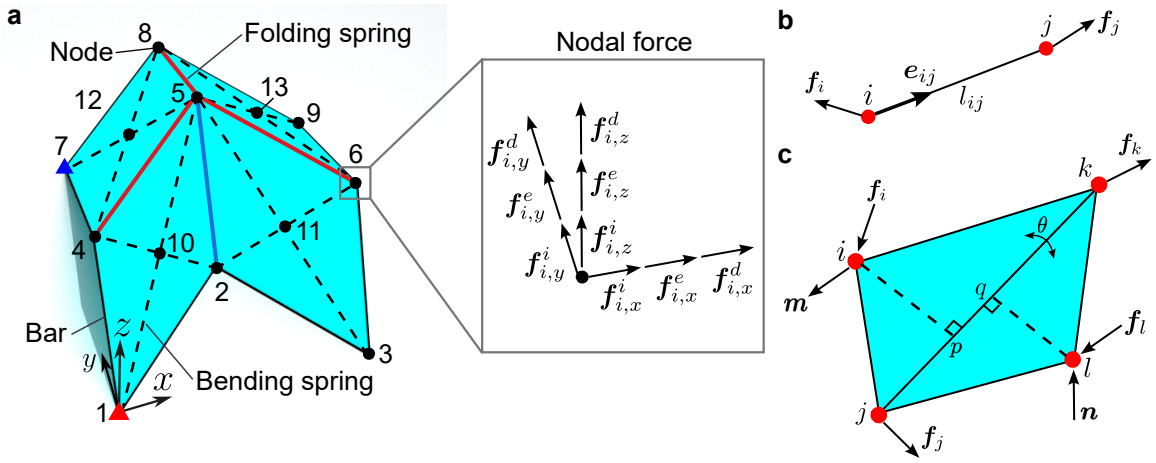

Figure 4.2: Discretization of a Miura-ori unit cell using the bar-and-hinge model. **a**, the discretized model, where nodes are represented by black dots. Solid red and blue lines denote mountain and valley creases, respectively, which are modeled with both bar and hinge elements. Dashed black lines outline the facets. The red triangle at Node 1 indicates a fixed boundary condition (zero displacement in x, y, and z), while the blue triangle at Node 7 indicates a roller boundary condition allowing translation only along the y-axis (zero displacement in x and z). The inset illustrates the resultant forces on a node. **b**, schematic of a bar element, representing axial stiffness between two nodes. **c**, schematic of a hinge element, representing the bending stiffness between adjacent facets.

4.2.2 Nodal internal force from bar elements

The bar elements are essentially modeled as linear-elastic spring elements with axial stiffness. Here, we consider an arbitrary pair of nodes i and j that consists of a bar element to express

the formulation of it as shown in Fig. 4.2(b).

$$\begin{aligned} \boldsymbol{f}_i^{\mathrm{b}} &= k^{\mathrm{b}}(l_{ij} - l_{ij}^0)\boldsymbol{e}_{ij} \\ \boldsymbol{f}_j^{\mathrm{b}} &= -k^{\mathrm{b}}(l_{ij} - l_{ij}^0)\boldsymbol{e}_{ij}, \end{aligned} \tag{4.6}$$

where k^{b} is the stiffness of a bar element, l_{ij}^0 is the initial length of a bar element, $\boldsymbol{e}_{ij} \in \mathbb{R}^3$ is the unit vector from node i to node j. Here, based on the previous work on the bar-and-hinge model [54], the bar stiffness k^{b} can be obtained as $k^{\mathrm{b}} = EA/l_{ij}^0$ where E is the Young's modulus of the material and A is the virtual cross section of the bar element. We can express the virtual area A as follows [79]:

$$A = \frac{2ST}{(1-\nu)\Sigma_{k=1}^3 L_k}, \tag{4.7}$$

where ν is Poissonś ratio of the material, and $\Sigma_{k=1}^3 L_k$ is the total length of three edges in a triangular section in the discretized Miura-ori model. The linearized force from a bar element for node i at the arbitrary state of the structure can be expressed as follows:

$$\boldsymbol{f}_i^{\mathrm{b}} \approx \boldsymbol{f}_i^{\mathrm{b}}|_{\boldsymbol{X}=\boldsymbol{X}_r} + \left.\frac{\partial \boldsymbol{f}_i^{\mathrm{b}}}{\partial \boldsymbol{x}_i}\right|_{\boldsymbol{X}=\boldsymbol{X}_r} (\boldsymbol{x}_i - \boldsymbol{x}_{i,r}) + \left.\frac{\partial \boldsymbol{f}_i^{\mathrm{b}}}{\partial \boldsymbol{x}_j}\right|_{\boldsymbol{X}=\boldsymbol{X}_r} (\boldsymbol{x}_j - \boldsymbol{x}_{j,r}), \tag{4.8}$$

where $\boldsymbol{f}_{i,r}^{\mathrm{b}} = \boldsymbol{f}_i^{\mathrm{b}}(\boldsymbol{X}_r)$ is the residual force at the reference configuration. We define $\boldsymbol{x}_i, \boldsymbol{x}_j \in \mathbb{R}^3$ as nodal position vectors, $\boldsymbol{X} = [\boldsymbol{x}_i, \boldsymbol{x}_j]$ as the set of vectors, and $\boldsymbol{X}_r$ denotes the corresponding reference configuration. The general form of the derivative term $\frac{\partial \boldsymbol{f}_i^{\mathrm{b}}}{\partial \boldsymbol{x}_i}$ can be expressed as follows

$$\frac{\partial \boldsymbol{f}_i^{\mathrm{b}}}{\partial \boldsymbol{x}_i} = k^{\mathrm{b}} \left\{ \frac{\partial l_{ij}}{\partial \boldsymbol{x}_i} \otimes \boldsymbol{e}_{ij} + (l_{ij} - l_{ij}^0) \frac{\partial \boldsymbol{e}_{ij}}{\partial \boldsymbol{x}_i} \right\}. \tag{4.9}$$

Under the small-displacement assumption around $\boldsymbol{X}_r$, the derivative terms can be expressed as follows:

$$\frac{\partial \boldsymbol{f}_i^{\mathrm{b}}}{\partial \boldsymbol{x}_i} = -k^{\mathrm{b}} \left[\boldsymbol{e}_{ij} \otimes \boldsymbol{e}_{ij} + \frac{l_{ij} - l_{ij}^0}{l_{ij}} (\boldsymbol{I} - \boldsymbol{e}_{ij} \otimes \boldsymbol{e}_{ij}) \right] \tag{4.10}$$

$$\frac{\partial \boldsymbol{f}_i^{\mathrm{b}}}{\partial \boldsymbol{x}_j} = k^{\mathrm{b}} \left[\boldsymbol{e}_{ij} \otimes \boldsymbol{e}_{ij} + \frac{l_{ij} - l_{ij}^0}{l_{ij}} (\boldsymbol{I} - \boldsymbol{e}_{ij} \otimes \boldsymbol{e}_{ij}) \right]. \tag{4.11}$$

Likewise, the derivative terms for node j are:

$$\frac{\partial \boldsymbol{f}_j^{\mathrm{b}}}{\partial \boldsymbol{x}_i} = k^{\mathrm{b}} \left[\boldsymbol{e}_{ij} \otimes \boldsymbol{e}_{ij} + \frac{l_{ij} - l_{ij}^0}{l_{ij}} (\boldsymbol{I} - \boldsymbol{e}_{ij} \otimes \boldsymbol{e}_{ij}) \right] \tag{4.12}$$

$$\frac{\partial \boldsymbol{f}_j^{\mathrm{b}}}{\partial \boldsymbol{x}_j} = -k^{\mathrm{b}} \left[\boldsymbol{e}_{ij} \otimes \boldsymbol{e}_{ij} + \frac{l_{ij} - l_{ij}^0}{l_{ij}} \left(\boldsymbol{I} - \boldsymbol{e}_{ij} \otimes \boldsymbol{e}_{ij} \right) \right]. \tag{4.13}$$

Therefore, under the assumption that the nodes experience small displacements, the force-displacement relationship is expressed as follows:

$$\begin{aligned} \begin{bmatrix} \boldsymbol{f}_i^{\mathrm{b}} \\ \boldsymbol{f}_j^{\mathrm{b}} \end{bmatrix} &\approx \begin{bmatrix} \boldsymbol{f}_{i,r}^{\mathrm{b}} \\ \boldsymbol{f}_{j,r}^{\mathrm{b}} \end{bmatrix} + k^{\mathrm{b}} \begin{bmatrix} -\boldsymbol{H} & \boldsymbol{H} \\ \boldsymbol{H} & -\boldsymbol{H} \end{bmatrix} \begin{bmatrix} \boldsymbol{d}_i \\ \boldsymbol{d}_j \end{bmatrix} \\ &= \begin{bmatrix} \boldsymbol{f}_{i,r}^{\mathrm{b}} \\ \boldsymbol{f}_{j,r}^{\mathrm{b}} \end{bmatrix} + \boldsymbol{K}_{ij}^{\mathrm{b}} \begin{bmatrix} \boldsymbol{d}_i \\ \boldsymbol{d}_j \end{bmatrix}, \end{aligned} \tag{4.14}$$

where $\boldsymbol{f}_{i,r}^{\mathrm{b}}$ and $\boldsymbol{f}_{j,r}^{\mathrm{b}}$ are the residual forces at the reference configuration. Here, $\boldsymbol{d}_i = \boldsymbol{x}_i - \boldsymbol{x}_{i,r}$ and $\boldsymbol{d}_j = \boldsymbol{x}_j - \boldsymbol{x}_{j,r}$ are the corresponding displacements. The nodal positions for nodes i and j at both current and reference configurations are defined as $\boldsymbol{x}_i$ and $\boldsymbol{x}_j$, $\boldsymbol{x}_{i,r}$ and $\boldsymbol{x}_{j,r}$, respectively. $\boldsymbol{H}$ is defined as

$$\boldsymbol{H} = \boldsymbol{e}_{ij} \otimes \boldsymbol{e}_{ij} + \frac{l_{ij} - l_{ij}^0}{l_{ij}} \left(\boldsymbol{I} - \boldsymbol{e}_{ij} \otimes \boldsymbol{e}_{ij} \right), \tag{4.15}$$

and $\boldsymbol{K}_{ij}^{\mathrm{b}} \in \mathbb{R}^{6\times 6}$ is the linearized bar element stiffness matrix around the reference configuration. This local linearization serves as the basis for assembling the global stiffness matrix across both equilibrium and non-equilibrium configurations.

4.2.3 Nodal internal force from hinge elements

The hinge elements are applied to the model to simulate crease folding and facet bending within an origami structure. To obtain a linearized stiffness matrix for hinge elements in our state-space representation, we refer to the formulation of hinge elements developed in previous research works [30, 54, 77, 78]. Fig. 4.2(c) depicts a general hinge element composed of an arbitrary set of nodes i to l to introduce the expression for the nodal force generated by a rotational spring within the element.

The nodal force acting on node i, generated by the rotational spring, is expressed as:

$$\boldsymbol{f}_i^{\mathrm{h}} = M \frac{\partial \theta}{\partial \boldsymbol{x}_i}, \tag{4.16}$$

where $M = -k^{\mathrm{h}} l_{kj}^0 (\theta - \theta_0)$ is the resistance moment. Here, k^{h} is the torsional stiffness per unit length of the hinge, l_{kj}^0 is the initial length between nodes k and j, θ is the dihedral angle between two facets, and θ_0 is the equilibrium angle. In the bar-and-hinge model, the torsional stiffness k^{h} can have two variations, k^h_{crease} and k^h_{facet}. They are used to simulate the different stiffness in bending along the crease line and facet within an origami structure. In this work, k^h_{crease} is calculated from the compression tests on the samples of the crease line (to be discussed in Section 4.6.2)), whereas k^h_{facet} is obtained from the actuation experiment of a Miura-ori unit cell (to be discussed in Section 4.7.1).

The linearization of $\boldsymbol{f}_i^{\mathrm{h}}$ at the reference state of the structure is expressed as follows:

$$\boldsymbol{f}_i^{\mathrm{h}} \approx \boldsymbol{f}_i^{\mathrm{h}}|_{\boldsymbol{X}=\boldsymbol{X}_r} + \sum_{p\in\{i,j,k,l\}} \left.\frac{\partial \boldsymbol{f}_i^{\mathrm{h}}}{\partial \boldsymbol{x}_p}\right|_{\boldsymbol{X}=\boldsymbol{X}_r} (\boldsymbol{x}_p - \boldsymbol{x}_{p,r}) \tag{4.17}$$

where we define $\boldsymbol{x}_i, \boldsymbol{x}_j, \boldsymbol{x}_k, \boldsymbol{x}_l \in \mathbb{R}^3$ as nodal position vectors, $\boldsymbol{X} = [\boldsymbol{x}_i, \boldsymbol{x}_j, \boldsymbol{x}_k, \boldsymbol{x}_l]$ as the set of vectors, and $\boldsymbol{X}_r$ as the given reference configuration. Thus, for instance, $\left.\frac{\partial \boldsymbol{f}_i^{\mathrm{h}}}{\partial \boldsymbol{x}_i}\right|_{\boldsymbol{X}=\boldsymbol{X}_r}$ represents the derivative term evaluated at the reference configuration of the structure. Detailed expressions for the partial derivatives $\partial \boldsymbol{f}_i^{\mathrm{h}}/\partial \boldsymbol{x}_p$ ($p \in \{i,j,k,l\}$) are provided below.

$$\begin{aligned}
\left.\frac{\partial \boldsymbol{f}_i^{\mathrm{h}}}{\partial \boldsymbol{x}_i}\right|_{\boldsymbol{X}=\boldsymbol{X}_r} &= k^{\mathrm{h}}\, l_{kj}^0 \left(\frac{\partial \theta}{\partial \boldsymbol{x}_i} \otimes \frac{\partial \theta}{\partial \boldsymbol{x}_i} + (\theta - \theta_0) \frac{\partial^2 \theta}{\partial \boldsymbol{x}_i^2} \right) \\
&= k^{\mathrm{h}}\, l_{kj}^0 \left\{ |\boldsymbol{r}_{kj}|^2 \boldsymbol{T}_{\boldsymbol{m}} - \frac{(\theta - \theta_0)}{|\boldsymbol{m}|^4} |\boldsymbol{r}_{kj}| \left[\boldsymbol{m} \otimes (\boldsymbol{r}_{kj} \times \boldsymbol{m}) + (\boldsymbol{r}_{kj} \times \boldsymbol{m}) \otimes \boldsymbol{m} \right] \right\}
\end{aligned} \tag{4.18a}$$

$$\begin{aligned}
\left.\frac{\partial \boldsymbol{f}_i^{\mathrm{h}}}{\partial \boldsymbol{x}_j}\right|_{\boldsymbol{X}=\boldsymbol{X}_r} &= k^{\mathrm{h}}\, l_{kj}^0 \left(\frac{\partial \theta}{\partial \boldsymbol{x}_j} \otimes \frac{\partial \theta}{\partial \boldsymbol{x}_i} + (\theta - \theta_0) \frac{\partial^2 \theta}{\partial \boldsymbol{x}_j \partial \boldsymbol{x}_i} \right) \\
&= k^{\mathrm{h}}\, l_{kj}^0 \left\{ \left(\boldsymbol{r}_{ij} \cdot \boldsymbol{r}_{kj} - |\boldsymbol{r}_{kj}|^2 \right) \boldsymbol{T}_{\boldsymbol{m}} + \boldsymbol{r}_{kl} \cdot \boldsymbol{r}_{kj}\, \boldsymbol{T}_{\boldsymbol{n},\boldsymbol{m}} \right. \\
&\quad \left. + \frac{(\theta - \theta_0)}{|\boldsymbol{m}|^4} \left[-\frac{|\boldsymbol{m}|^2}{|\boldsymbol{r}_{kj}|} \boldsymbol{r}_{kj} \otimes \boldsymbol{m} + |\boldsymbol{r}_{kj}| \big(\boldsymbol{m} \otimes (\boldsymbol{r}_{ki} \times \boldsymbol{m}) + (\boldsymbol{r}_{ki} \times \boldsymbol{m}) \otimes \boldsymbol{m} \big) \right] \right\}
\end{aligned} \tag{4.18b}$$

$$\begin{aligned}
\left.\frac{\partial \boldsymbol{f}_i^{\mathrm{h}}}{\partial \boldsymbol{x}_k}\right|_{\boldsymbol{X}=\boldsymbol{X}_r} &= k^{\mathrm{h}}\, l_{kj}^0 \left(\frac{\partial \theta}{\partial \boldsymbol{x}_k} \otimes \frac{\partial \theta}{\partial \boldsymbol{x}_i} + (\theta - \theta_0) \frac{\partial^2 \theta}{\partial \boldsymbol{x}_k \partial \boldsymbol{x}_i} \right) \\
&= k^{\mathrm{h}}\, l_{kj}^0 \left\{ - \left(\boldsymbol{r}_{kl} \cdot \boldsymbol{r}_{kj} - |\boldsymbol{r}_{kj}|^2 \right) \boldsymbol{T}_{\boldsymbol{n},\boldsymbol{m}} - \boldsymbol{r}_{ij} \cdot \boldsymbol{r}_{kj} \boldsymbol{T}_{\boldsymbol{m}} \right.
\end{aligned}$$

$$+\frac{(\theta-\theta_0)}{|\boldsymbol{m}|^4}\left[\frac{|\boldsymbol{m}|^2}{|\boldsymbol{r}_{kj}|}\,\boldsymbol{r}_{kj}\otimes\boldsymbol{m}+|\boldsymbol{r}_{kj}|\big(\boldsymbol{m}\otimes(\boldsymbol{r}_{ij}\times\boldsymbol{m})+(\boldsymbol{r}_{ij}\times\boldsymbol{m})\otimes\boldsymbol{m}\big)\right]\Bigg\} \tag{4.18c}$$

$$\begin{aligned}\left.\frac{\partial\boldsymbol{f}_i^{\mathrm{h}}}{\partial\boldsymbol{x}_l}\right|_{\boldsymbol{X}=\boldsymbol{X}_r} &= k^{\mathrm{h}}\,l_{kj}^0\left(\frac{\partial\theta}{\partial\boldsymbol{x}_l}\otimes\frac{\partial\theta}{\partial\boldsymbol{x}_i}+(\theta-\theta_0)\,\frac{\partial^2\theta}{\partial\boldsymbol{x}_l\partial\boldsymbol{x}_i}\right)\\ &= -k^{\mathrm{h}}\,l_{kj}^0\,|\boldsymbol{r}_{kj}|^2\,\boldsymbol{T}_{\boldsymbol{n},\boldsymbol{m}},\end{aligned} \tag{4.18d}$$

where $\boldsymbol{m}=\boldsymbol{r_{ij}}\times\boldsymbol{r_{kj}}$ and $\boldsymbol{n}=\boldsymbol{r_{kj}}\times\boldsymbol{r_{kl}}$ are normal vectors of triangular panels among sets of nodes $\{i,j,k\}$ and $\{j,k,l\}$, respectively. We define $\boldsymbol{x}_i\in\mathbb{R}^3$ as a nodal position vector and $\boldsymbol{r}_{ab}=\boldsymbol{x}_a-\boldsymbol{x}_b$ as a relative position vector. To simplify the derivations, we introduced the normalized tensorial quantities $T_m=\frac{\boldsymbol{m}\otimes\boldsymbol{m}}{|\boldsymbol{m}|^4}$ and $T_{n,m}=\frac{\boldsymbol{n}\otimes\boldsymbol{m}}{|\boldsymbol{n}|^2\,|\boldsymbol{m}|^2}$. We obtain the stiffness matrix of a hinge element for node i as follows:

$$\boldsymbol{K}_i^{\mathrm{h}}=\left[\left.\frac{\partial\boldsymbol{f}_i^{\mathrm{h}}}{\partial\boldsymbol{x}_i}\right|_{\boldsymbol{X}=\boldsymbol{X}_r}\quad\left.\frac{\partial\boldsymbol{f}_i^{\mathrm{h}}}{\partial\boldsymbol{x}_j}\right|_{\boldsymbol{X}=\boldsymbol{X}_r}\quad\left.\frac{\partial\boldsymbol{f}_i^{\mathrm{h}}}{\partial\boldsymbol{x}_k}\right|_{\boldsymbol{X}=\boldsymbol{X}_r}\quad\left.\frac{\partial\boldsymbol{f}_i^{\mathrm{h}}}{\partial\boldsymbol{x}_l}\right|_{\boldsymbol{X}=\boldsymbol{X}_r}\right]. \tag{4.19}$$

In summary, the relationship between the nodal force and small nodal displacements within the hinge element is summarized as follows:

$$\boldsymbol{f}_i^{\mathrm{h}}=\boldsymbol{f}_i^{\mathrm{h}}|_{\boldsymbol{X}=\boldsymbol{X}_r}+\boldsymbol{K}_i^{\mathrm{h}}\boldsymbol{d}. \tag{4.20}$$

Likewise, derivative terms for node l are expressed as follows:

$$\begin{aligned}\left.\frac{\partial\boldsymbol{f}_l^{\mathrm{h}}}{\partial\boldsymbol{x}_i}\right|_{\boldsymbol{X}=\boldsymbol{X}_r} &= k^{\mathrm{h}}\,l_{kj}^0\left(\frac{\partial\theta}{\partial\boldsymbol{x}_i}\otimes\frac{\partial\theta}{\partial\boldsymbol{x}_l}+(\theta-\theta_0)\,\frac{\partial^2\theta}{\partial\boldsymbol{x}_i\partial\boldsymbol{x}_l}\right)\\ &= -k^{\mathrm{h}}\,l_{kj}^0\,|\boldsymbol{r}_{kj}|^2\,\boldsymbol{T}_{\boldsymbol{m},\boldsymbol{n}}\end{aligned} \tag{4.21a}$$

$$\begin{aligned}\left.\frac{\partial\boldsymbol{f}_l^{\mathrm{h}}}{\partial\boldsymbol{x}_j}\right|_{\boldsymbol{X}=\boldsymbol{X}_r} &= k^{\mathrm{h}}\,l_{kj}^0\left(\frac{\partial\theta}{\partial\boldsymbol{x}_j}\otimes\frac{\partial\theta}{\partial\boldsymbol{x}_l}+(\theta-\theta_0)\,\frac{\partial^2\theta}{\partial\boldsymbol{x}_j\partial\boldsymbol{x}_l}\right)\\ &= k^{\mathrm{h}}\,l_{kj}^0\Bigg\{-\big(\boldsymbol{r}_{ij}\cdot\boldsymbol{r}_{kj}-|\boldsymbol{r}_{kj}|^2\big)\,\boldsymbol{T}_{\boldsymbol{m},\boldsymbol{n}}-\boldsymbol{r}_{kl}\cdot\boldsymbol{r}_{kj}\,\boldsymbol{T}_{\boldsymbol{n}}\\ &\quad+\frac{(\theta-\theta_0)}{|\boldsymbol{n}|^4}\left[\frac{|\boldsymbol{n}|^2}{|\boldsymbol{r}_{kj}|}\,\boldsymbol{r}_{kj}\otimes\boldsymbol{n}-|\boldsymbol{r}_{kj}|\big(\boldsymbol{n}\otimes(\boldsymbol{r}_{kl}\times\boldsymbol{n})+(\boldsymbol{r}_{kl}\times\boldsymbol{n})\otimes\boldsymbol{n}\big)\right]\Bigg\}\end{aligned} \tag{4.21b}$$

$$\left.\frac{\partial\boldsymbol{f}_l^{\mathrm{h}}}{\partial\boldsymbol{x}_k}\right|_{\boldsymbol{X}=\boldsymbol{X}_r} = k^{\mathrm{h}}\,l_{kj}^0\left(\frac{\partial\theta}{\partial\boldsymbol{x}_k}\otimes\frac{\partial\theta}{\partial\boldsymbol{x}_l}+(\theta-\theta_0)\,\frac{\partial^2\theta}{\partial\boldsymbol{x}_k\partial\boldsymbol{x}_l}\right)$$

$$= k^{\mathrm{h}}\, l_{kj}^{0} \left\{ \left(\boldsymbol{r}_{kl} \cdot \boldsymbol{r}_{kj} - |\boldsymbol{r}_{kj}|^2 \right) \boldsymbol{T}_{\boldsymbol{n}} + \boldsymbol{r}_{ij} \cdot \boldsymbol{r}_{kj} \boldsymbol{T}_{\boldsymbol{m},\boldsymbol{n}} \right.$$
$$\left. + \frac{(\theta - \theta_0)}{|\boldsymbol{n}|^4} \left[-\frac{|\boldsymbol{n}|^2}{|\boldsymbol{r}_{kj}|} \boldsymbol{r}_{kj} \otimes \boldsymbol{n} - |\boldsymbol{r}_{kj}| \left(\boldsymbol{n} \otimes (\boldsymbol{r}_{lj} \times \boldsymbol{n}) + (\boldsymbol{r}_{lj} \times \boldsymbol{n}) \otimes \boldsymbol{n} \right) \right] \right\} \quad (4.21c)$$

$$\left. \frac{\partial \boldsymbol{f}_l^{\mathrm{h}}}{\partial \boldsymbol{x}_l} \right|_{\boldsymbol{X}=\boldsymbol{X}_r} = k^{\mathrm{h}}\, l_{kj}^{0} \left(\frac{\partial \theta}{\partial \boldsymbol{x}_l} \otimes \frac{\partial \theta}{\partial \boldsymbol{x}_l} + (\theta - \theta_0) \frac{\partial^2 \theta}{\partial \boldsymbol{x}_l^2} \right)$$
$$= k^{\mathrm{h}}\, l_{kj}^{0} \left\{ |\boldsymbol{r}_{kj}|^2 \boldsymbol{T}_{\boldsymbol{n}} + \frac{(\theta - \theta_0)}{|\boldsymbol{n}|^4} |\boldsymbol{r}_{kj}| \left[\boldsymbol{n} \otimes (\boldsymbol{r}_{kj} \times \boldsymbol{n}) + (\boldsymbol{r}_{kj} \times \boldsymbol{n}) \otimes \boldsymbol{n} \right] \right\}. \quad (4.21d)$$

Thus, we obtain the stiffness matrix of a hinge element for node l as follows:

$$\boldsymbol{K}_l^{\mathrm{h}} = \left[\left. \frac{\partial \boldsymbol{f}_l^{\mathrm{h}}}{\partial \boldsymbol{x}_i} \right|_{\boldsymbol{X}=\boldsymbol{X}_r} \quad \left. \frac{\partial \boldsymbol{f}_l^{\mathrm{h}}}{\partial \boldsymbol{x}_j} \right|_{\boldsymbol{X}=\boldsymbol{X}_r} \quad \left. \frac{\partial \boldsymbol{f}_l^{\mathrm{h}}}{\partial \boldsymbol{x}_k} \right|_{\boldsymbol{X}=\boldsymbol{X}_r} \quad \left. \frac{\partial \boldsymbol{f}_l^{\mathrm{h}}}{\partial \boldsymbol{x}_l} \right|_{\boldsymbol{X}=\boldsymbol{X}_r} \right]. \quad (4.22)$$

Based on $\boldsymbol{K}_i^{\mathrm{h}}$ and $\boldsymbol{K}_l^{\mathrm{h}}$, we can define $\boldsymbol{K}_j^{\mathrm{h}}$ and $\boldsymbol{K}_k^{\mathrm{h}}$ to balance the reaction force within the element as follows:

$$\begin{aligned} \boldsymbol{K}_j^{\mathrm{h}} &= -\left(\frac{l_{kq}}{l_{kj}} \boldsymbol{K}_l^{\mathrm{h}} + \frac{l_{kp}}{l_{kj}} \boldsymbol{K}_i^{\mathrm{h}} \right) \\ \boldsymbol{K}_k^{\mathrm{h}} &= -\left(\frac{l_{jq}}{l_{kj}} \boldsymbol{K}_l^{\mathrm{h}} + \frac{l_{jp}}{l_{kj}} \boldsymbol{K}_i^{\mathrm{h}} \right), \end{aligned} \quad (4.23)$$

where l_{jp}, l_{jq}, l_{kp}, and l_{kq} are the distance between nodes i and j, and points p and q, respectively. In summary, the relationship between the nodal force and small nodal displacements within the hinge element is summarized as follows:

$$\begin{aligned} \boldsymbol{f}_i^{\mathrm{h}} &= \boldsymbol{f}_{i,r}^{\mathrm{h}} + \boldsymbol{K}_i^{\mathrm{h}} \boldsymbol{d} \\ \boldsymbol{f}_j^{\mathrm{h}} &= \boldsymbol{f}_{j,r}^{\mathrm{h}} + \boldsymbol{K}_j^{\mathrm{h}} \boldsymbol{d} \\ \boldsymbol{f}_k^{\mathrm{h}} &= \boldsymbol{f}_{k,r}^{\mathrm{h}} + \boldsymbol{K}_k^{\mathrm{h}} \boldsymbol{d} \\ \boldsymbol{f}_l^{\mathrm{h}} &= \boldsymbol{f}_{l,r}^{\mathrm{h}} + \boldsymbol{K}_l^{\mathrm{h}} \boldsymbol{d}, \end{aligned} \quad (4.24)$$

where $\boldsymbol{f}_{p,r}^{\mathrm{h}} = M \left(\frac{\partial \theta}{\partial \boldsymbol{x}_p} \right)_{\boldsymbol{X}_r}$ for $p \in \{i, j, k, l\}$, and $\boldsymbol{K}_i^{\mathrm{h}}, \boldsymbol{K}_j^{\mathrm{h}}, \boldsymbol{K}_k^{\mathrm{h}}, \boldsymbol{K}_l^{\mathrm{h}} \in \mathbb{R}^{3\times 12}$ are the element stiffness matrices of a hinge element. This affine formulation enables local linearization of hinge forces around configurations with non-zero internal energy or residual stress.

4.3 State-space representation of the dynamics of Miura-ori unit cell

In control engineering, state-space modeling provides a unified way to represent the dynamics of a system through first-order differential equations involving state variables, inputs, and outputs [55, 80]. For systems linearized around an arbitrary configuration, the dynamics can be approximated using an affine state-space form:

$$\dot{\boldsymbol{x}}_{\mathrm{st}} = \boldsymbol{A}\,\boldsymbol{x}_{\mathrm{st}} \;+\; \boldsymbol{B}\,u_{\mathrm{in}} \;+\; \boldsymbol{c}, \tag{4.25}$$

where $\boldsymbol{x}_{\mathrm{st}} \in \mathbb{R}^{6n\times 1}$ is the state vector, $u_{\mathrm{in}} \in \mathbb{R}$ is the input torque from actuators, $\boldsymbol{A} \in \mathbb{R}^{6n\times 6n}$ is the state matrix, and $\boldsymbol{B} \in \mathbb{R}^{6n\times 1}$ is the input matrix. The offset vector $\boldsymbol{c} \in \mathbb{R}^{6n\times 1}$ accounts for residual forces that arise from affine (non-zero) equilibrium conditions. Here, n is the total number of nodes in the bar-and-hinge model of Miura-ori structures.

For our bar-and-hinge model of the Miura-ori unit cell, $\boldsymbol{x}_{\mathrm{st}}$ and $\boldsymbol{A}$ can be expressed as follows:

$$\begin{aligned} \boldsymbol{x}_{\mathrm{st}} &= \begin{bmatrix} d_1 & \dots & d_{3n} & \dot{d}_1 & \dots & \dot{d}_{3n} \end{bmatrix}^T \\ \boldsymbol{A} &= \begin{bmatrix} \boldsymbol{0} & \boldsymbol{I} \\ \boldsymbol{M}^{-1}\boldsymbol{K} & \boldsymbol{M}^{-1}\boldsymbol{C}_{\mathrm{damp}} \end{bmatrix}. \end{aligned} \tag{4.26}$$

Here, $\boldsymbol{A}$ is constructed from the global mass matrix $\boldsymbol{M} \in \mathbb{R}^{3n\times 3n}$, global stiffness matrix $\boldsymbol{K} \in \mathbb{R}^{3n\times 3n}$, and damping matrix $\boldsymbol{C}_{\mathrm{damp}} \in \mathbb{R}^{3n\times 3n}$. The global stiffness matrix $\boldsymbol{K}$ is based on the aforementioned bar and hinge element matrices $\boldsymbol{K}_{ij}^{\mathrm{b}}$ and $\boldsymbol{K}_{i}^{\mathrm{h}}$, respectively. As schematically shown in Fig. 4.3(a), the matrices $\boldsymbol{A}$ and $\boldsymbol{B}$ depend on the reference configuration of Miura-ori and the actuator location, respectively. The affine offset term $\boldsymbol{c}$ is defined as

$$\boldsymbol{c} = \begin{bmatrix} \boldsymbol{0} \\ \boldsymbol{M}^{-1}\boldsymbol{f}_r \end{bmatrix}, \tag{4.27}$$

where $\boldsymbol{f}_r$ denotes the vector of residual internal forces resulting from the linearization around a non-equilibrium configuration. These residuals may include, for example, the bar and hinge forces at node i, denoted $\boldsymbol{f}_{i,r}^{\mathrm{b}}$ and $\boldsymbol{f}_{i,r}^{\mathrm{h}}$, respectively. Details of the input matrix $\boldsymbol{B}$ are provided in Section 4.3.1.

The Miura-ori structure is first linearized about the zero-energy state ($\boldsymbol{c} = \boldsymbol{0}$), forming the basis for the small-deformation analysis. To address large deformations, it is also linearized about arbitrary configurations with non-zero internal energy. At each linearization point, the matrices $\boldsymbol{A}$, $\boldsymbol{B}$, and $\boldsymbol{c}$ are updated. This approach constitutes a piecewise-affine framework, which enables systematic modeling of the structure's nonlinear response through a sequence of locally valid affine systems.

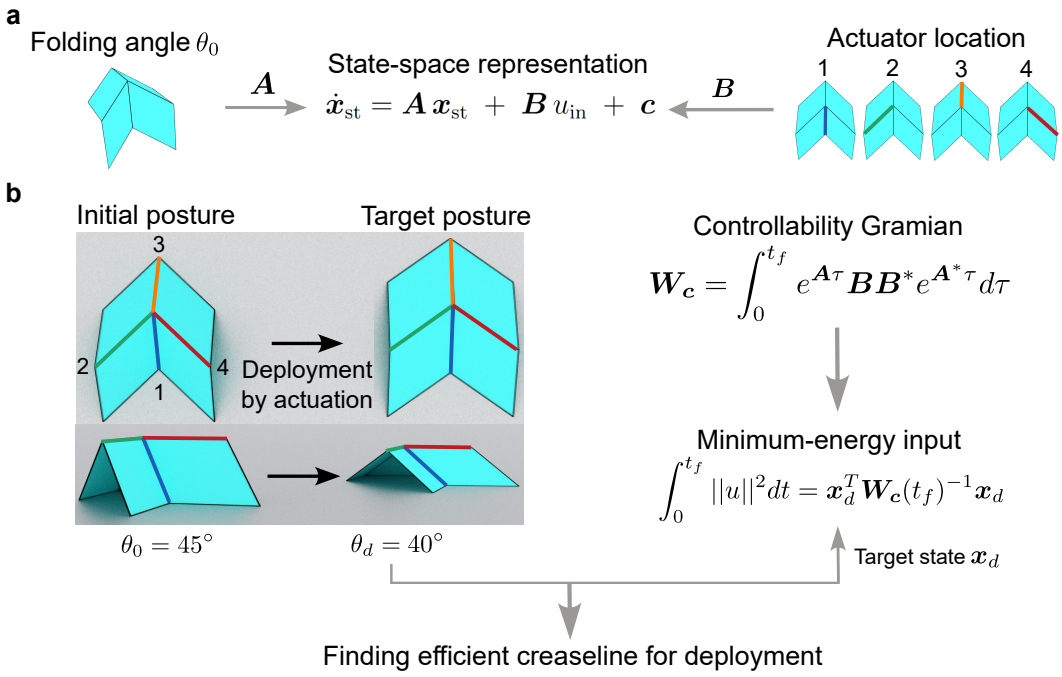

Figure 4.3: **a**, schematic illustration of the state-space representation of origami dynamics. State matrix $\boldsymbol{A}$ and input matrix $\boldsymbol{B}$ are dependent on the folding angle of Miura-ori θ_0 and the location of the actuator (Crease 1-4), respectively. The affine term $\boldsymbol{c}$ arises from linearization around a non-zero configuration. **b**, schematic illustration of obtaining controllability Gramian $\boldsymbol{W_c}$ and minimum-energy input $||u||_{L2}^2$, shown here for the simplified case $\boldsymbol{c} = 0$.

4.3.1 Formulation of the input matrix

In this section, we discuss how to construct the input matrix $\boldsymbol{B}$ in the state-space representation. In this work, we consider inputs from the actuation of the crease line. Therefore, the formulation of the input matrix can be based on the hinge element depicted in Fig. 4.2(c) and discussed in the previous section. As shown in Fig. 4.4, the element-wise nodal forces from the actuation of the hinge are described as follows:

$$\begin{aligned}
\boldsymbol{F_i} &= \frac{\boldsymbol{m}}{|\boldsymbol{m}|}\frac{u_{in}}{l_{ip}} \\
\boldsymbol{F_j} &= -\left(\frac{l_{kq}}{l_{jk}}\boldsymbol{F}_l + \frac{l_{kp}}{l_{jk}}\boldsymbol{F}_i\right) \\
\boldsymbol{F_k} &= -\left(\frac{l_{jq}}{l_{jk}}\boldsymbol{F}_l + \frac{l_{jp}}{l_{jk}}\boldsymbol{F}_i\right) \\
\boldsymbol{F_l} &= -\frac{\boldsymbol{n}}{|\boldsymbol{n}|}\frac{u_{in}}{l_{lq}},
\end{aligned} \tag{4.28}$$

where u_{in} is the external input torque on the actuated crease line. These nodal forces are summed up to construct the input matrix $\boldsymbol{B}$ based on the node numbers of the actuated crease line element in the bar-and-hinge model of a Miura-ori structure. By incorporating the input matrix into the state-space representation, we further analyze the controllability of the Miura-ori unit cell.

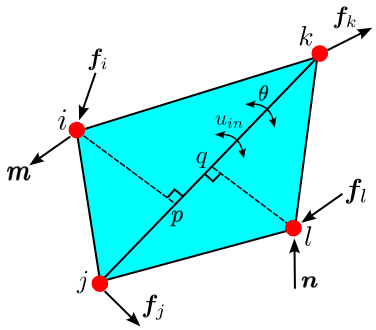

Figure 4.4: Schematic illustration of a hinge element with the external input torque u_{in}.

4.4 Controllability analysis of origami dynamics

Based on the affine state-space representation in Eq. (4.25), we analyze the controllability of the system [81, 82]. A system is controllable if it can be driven from any initial state to any final state within a finite time using admissible control inputs. To investigate the controllability, we analyze the controllability Gramian $\boldsymbol{W_c}$ of a linear time-invariant system and its eigendecomposition, defined as follows [55, 80, 83, 84]:

$$\boldsymbol{W}_c(t) = \int_0^t e^{\boldsymbol{A}\tau}\, \boldsymbol{B}\boldsymbol{B}^T e^{\boldsymbol{A}^T\tau}\, d\tau, \qquad \boldsymbol{W}_c(t)\, \boldsymbol{\zeta}_i = \lambda_i\, \boldsymbol{\zeta}_i, \tag{4.29}$$

where $\boldsymbol{\zeta}_i$ is the eigenvector and λ_i is the eigenvalue of $\boldsymbol{W_c}$. Here, the system is controllable if the controllability Gramian $\boldsymbol{W_c}$ is positive definite, that is, the minimum eigenvalue $\lambda_{\min}$ is larger than zero (see Section 4.4.1 for the details).

We can also calculate minimum-energy input required to steer the system from an initial state $\boldsymbol{x}_0$ (state vector $\boldsymbol{x}_{\text{st}}$ at initial condition) to a target state $\boldsymbol{x}_d$ (state vector $\boldsymbol{x}_{\text{st}}$ at target condition) over time T_f, by utilizing the controllability Gramian.

$$||u||_{L_2}^2 = \int_0^{T_f} \|u\|^2\, dt = \left(\boldsymbol{x}_d - e^{\boldsymbol{A}T_f}\boldsymbol{x}_0 - \boldsymbol{h_c}(T_f)\right)^T \boldsymbol{W}_c^{-1} \left(\boldsymbol{x}_d - e^{\boldsymbol{A}T_f}\boldsymbol{x}_0 - \boldsymbol{h_c}(T_f)\right), \tag{4.30}$$

where $\boldsymbol{h_c}(T_f) = \int_0^{T_f} e^{\boldsymbol{A}(T_f-\tau)}\boldsymbol{c}\, d\tau$ accounts for the integrated effect of the affine term $\boldsymbol{c}$ over the time horizon. $||u||_{L_2}^2$ has units of $\mathrm{N^2m^2s}$ in this study, as torque is used as the control input (see Section 4.4.2).

To evaluate input effort under large deformations, we apply the previously introduced piecewise-affine framework by linearizing the system at multiple configurations. For each segment, the operating point is set to the initial state of that segment, where the local state-space matrices are reconstructed and the corresponding $||u||_{L_2}^2$ is computed. The total input energy is the sum of the minimum-energy inputs across all segments, where u_i is the optimal control input for segment i and N is the number of segments:

$$\mathcal{U}_{\text{tot}} := \sum_{i=1}^{N} \|u_i\|_{L_2}^2. \tag{4.31}$$

We utilize the total minimum control energy $\mathcal{U}_{\text{tot}}$ to rank candidate crease lines in terms of deployment efficiency. For example, if an initial folding angle of a Miura-ori is $\theta_0 = 45°$ and we aim to deploy it to $\theta_d = 40°$ by actuating even a single crease line, finding the most efficient crease line among four candidates (shown in Fig. 4.3(b)) is nontrivial, given specific geometry and boundary conditions of the Miura-ori structure. To address this, we evaluate the deployment efficiency using the controllability Gramian by quantifying the minimum control energy required for each case. For small folding angle changes, this analysis is conducted over a single segment (i.e., $N = 1$). The theoretical deployment efficiency e_t is defined as follows:

$$e_t := \frac{1}{\mathcal{U}_{\text{tot}}}. \tag{4.32}$$

Thus, a higher value of e_t indicates better deployment efficiency.

4.4.1 Confirming the controllability of the origami dynamics

Based on the validity of the state-space modeling, we first confirm the controllability of the system for each location of the actuator. As stated in the previous section, we can confirm the controllability of the system by examining the minimum eigenvalue λ_{min} of the controllability Gramian $\boldsymbol{W}_c$. That is, the minimum eigenvalue has to be larger than zero to confirm the system is controllable. The equation is presented as follows:

$$\boldsymbol{W}_c(t) = \int_0^t e^{\boldsymbol{A}\tau}\, \boldsymbol{B}\boldsymbol{B}^T e^{\boldsymbol{A}^T\tau}\, d\tau, \qquad \boldsymbol{W}_c(t)\, \boldsymbol{\zeta}_i = \lambda_i\, \boldsymbol{\zeta}_i. \tag{4.33}$$

Based on Eq. (4.29), Fig. 4.5 presents the minimum eigenvalues of the controllability Gramian for (a), the unit cell, (b), the two-cell configuration, and (c), the four-cell configuration, showing that the system is controllable under the current material parameters, inputs, and constraint conditions.

4.4.2 Dimensional analysis of controllability Gramian and minimum-energy input

In the previous chapters, we described the state-space representation, the controllability Gramian, and the magnitude of the minimum-energy control input for arbitrary configura-

a

	Minimum eigenvalue of W_c
Crease 1	3.63×10^{-10}
Crease 2	8.95×10^{-10}
Crease 3	2.94×10^{-9}
Crease 4	9.81×10^{-9}

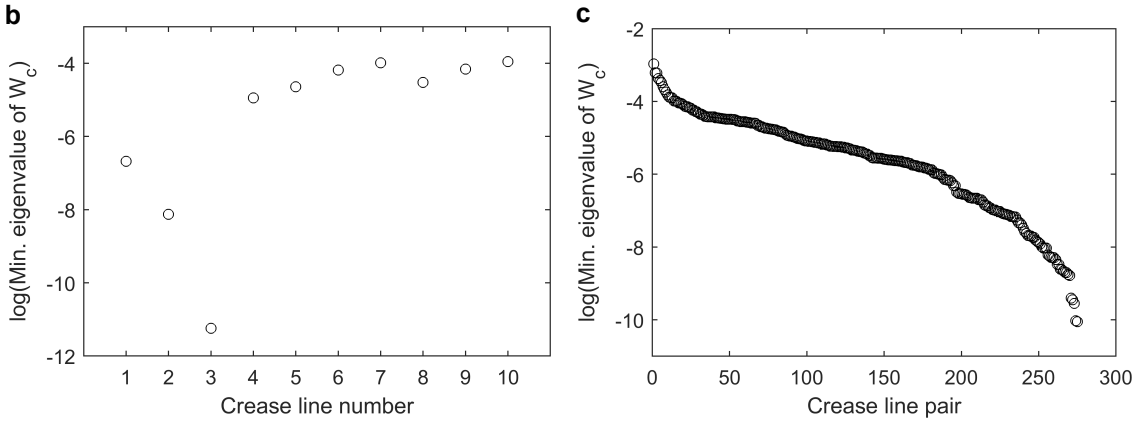

Figure 4.5: Minimum eigenvalues of the controllability Gramian for **a**, the unit cell (table format), **b**, the two-cell configuration by crease line number, and **c**, the four-cell configuration with values from 276 crease line pairs sorted in ascending order, all plotted on a logarithmic scale.

tions. For the purpose of dimensional analysis, we consider the case where the system starts from the zero-energy configuration, as follows:

$$\dot{\boldsymbol{x}}_{st} = \boldsymbol{A}\boldsymbol{x}_{st} + \boldsymbol{B}\boldsymbol{u}_{in} \tag{4.34}$$

$$\boldsymbol{W}_c = \int_0^{t_f} e^{\boldsymbol{A}\tau}\boldsymbol{B}\boldsymbol{B}^T e^{\boldsymbol{A}^T\tau}\, d\tau \tag{4.35}$$

$$\|u\|_{L2}^2 = \int_0^t \|u(\tau)\|^2 d\tau = \boldsymbol{x}_d^T \boldsymbol{W}_c^{-1}\boldsymbol{x}_d. \tag{4.36}$$

In this section, we confirm the physical unit of each equation to review the validity of our data processing from the experiments. The state vector $\boldsymbol{x}_{st}$ consists of displacement [m] and velocity [m/s]. Hence, $\dot{\boldsymbol{x}_{st}}$ consists of velocity [m/s] and acceleration [m/s^2]. The input vector $\boldsymbol{u}_{in}$ is torque [N·m]. Based on the units of variables $\boldsymbol{x}_{st}$ and $\boldsymbol{u}_{in}$, the units of state-space equation (4.34) are as follows:

$$\begin{bmatrix} \mathrm{m/s} \\ \mathrm{m/s^2} \end{bmatrix} = \begin{bmatrix} 0 & 1 \\ \mathrm{s^{-2}} & \mathrm{s^{-1}} \end{bmatrix} \begin{bmatrix} \mathrm{m} \\ \mathrm{m/s} \end{bmatrix} + \begin{bmatrix} 0 \\ \mathrm{kg^{-1}m^{-1}} \end{bmatrix} \begin{bmatrix} \mathrm{N \cdot m} \end{bmatrix}. \tag{4.37}$$

The units of controllability Gramian $\boldsymbol{W}_c$ (4.35) are as follows:

$$e^{\boldsymbol{A}\tau}\boldsymbol{B}\boldsymbol{B}^T e^{\boldsymbol{A}^T\tau}\, d\tau : [-] \begin{bmatrix} 0 \\ \mathrm{kg^{-1}m^{-1}} \end{bmatrix} \begin{bmatrix} 0 & \mathrm{kg^{-1}m^{-1}} \end{bmatrix} [-] \begin{bmatrix} \mathrm{s} \end{bmatrix} = \begin{bmatrix} 0 & 0 \\ 0 & \mathrm{s \cdot kg^{-2}m^{-2}} \end{bmatrix}. \tag{4.38}$$

Here, $e^{\boldsymbol{A}\tau}$ and $e^{\boldsymbol{A}^T\tau}$ have no physical dimension. Hence, the units of the magnitude of the minimum-energy control input $\|u\|_{L2}^2$ (4.36) are as follows:

$$\boldsymbol{x}_d^T \boldsymbol{W}_{\boldsymbol{c}}^{-1}\boldsymbol{x}_d : \begin{bmatrix} \mathrm{m} & \mathrm{m/s} \end{bmatrix} \begin{bmatrix} 0 & 0 \\ 0 & \mathrm{s^{-1} \cdot kg^2m^2} \end{bmatrix} \begin{bmatrix} \mathrm{m} \\ \mathrm{m/s} \end{bmatrix} = \begin{bmatrix} \mathrm{kg^2m^4/s^3} \end{bmatrix} \tag{4.39}$$

$$\mathrm{kg^2m^4/s^3} = \mathrm{N^2 \cdot m^2 \cdot s}. \tag{4.40}$$

Here, $[\mathrm{N^2 \cdot m^2 \cdot s}]$ is a unit of $\int_0^t \|u(\tau)\|^2 d\tau$, matching with the square of torque multiplied by time.

4.5 Physical interpretation using Euler–Lagrange dynamics

The Euler–Lagrange equation, which incorporates both conservative and dissipative effects in mechanical systems with external forcing, is employed in our analysis and is expressed as

$$\frac{d}{dt}\left(\frac{\partial L}{\partial \dot{q}_i}\right) - \frac{\partial L}{\partial q_i} + \frac{\partial F}{\partial \dot{q}_i} = Q_i, \tag{4.41}$$

where $L = T - V$ is the Lagrangian, F is the Rayleigh dissipation function, and Q_i is the generalized force acting on coordinate q_i.

We assume the Miura-ori unit as a single-degree-of-freedom system governed by a folding angle θ. During the deployment process, each crease i undergoes a local rotation $\phi_i(\theta)$. The actuation torque u_i, applied about the local crease axis, contributes to generalized torque associated with θ. This relationship is characterized by the kinematic ratio $S_i = \frac{d\phi_i}{d\theta}$, which quantifies how the local folding rate of crease i maps to the global folding rate, as illustrated in Fig. 4.6(a). The kinetic, potential, and dissipative energies are modeled as $T = \frac{1}{2}I(\theta)\dot{\theta}^2, V = \frac{1}{2}k(\theta)(\theta - \theta_0)^2, F = \frac{1}{2}C(\theta)\dot{\theta}^2$, where $I(\theta)$, $k(\theta)$, and $C(\theta)$ denote the effective inertia, stiffness, and damping coefficients, respectively, which may vary with the global folding angle θ. Substituting these into Eq. (4.41) yields the general nonlinear equation of motion:

$$I(\theta)\ddot{\theta} + C(\theta)\dot{\theta} + k(\theta)(\theta - \theta_0) = u_i S_i(\theta). \tag{4.42}$$

For analytical tractability, we neglect higher-order terms associated with the θ-dependence of inertia and stiffness. Linearizing this expression around a nominal configuration $\theta = \bar{\theta}$ leads to

$$I^*\ddot{\theta} + C^*\dot{\theta} + k^*(\theta - \theta_0) = u_i S_i^*, \tag{4.43}$$

where $I^* = I(\bar{\theta})$, and $S_i^* = \frac{d\phi_i}{d\theta}\big|_{\theta=\bar{\theta}}$ is the evaluated kinematic leverage at the operating point. We now derive the minimum-energy input required to achieve a prescribed global displacement $\Delta\theta$ over a finite time horizon T_f. We begin by expressing the linearized dynamics in state-space form. Defining the state vector $\boldsymbol{x} = [\theta - \theta_0,\ \dot{\theta}]^\top$, the system can be written as

$$\dot{\boldsymbol{x}}(t) = \boldsymbol{A}\boldsymbol{x}(t) + \boldsymbol{B}_i u_i(t) \tag{4.44}$$

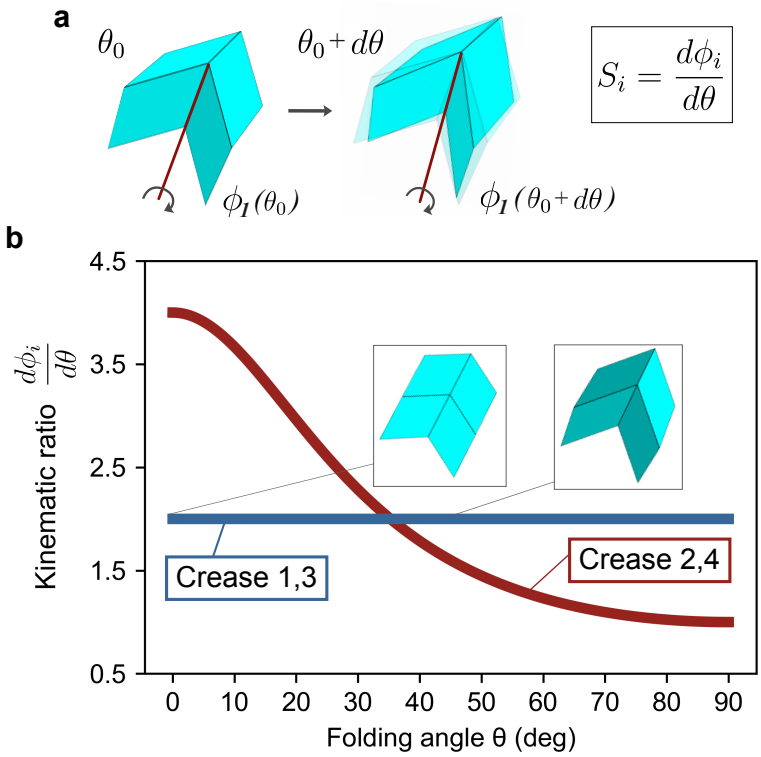

Figure 4.6: **a**, illustration of the kinematic ratio $S_i = \frac{d\phi_i}{d\theta}$, representing the relative folding rate of crease i with respect to the folding angle θ in the single-degree-of-freedom Miura-ori model. **b**, kinematic ratio S_i of each crease line, plotted against the folding angle θ. In the early stage of deployment, creases 1 and 3 exhibit higher S_i values, after which the kinematic ratios of creases 2 and 4 become reversed. The right inset shows the Miura-ori at $\theta = 45°$.

$$\boldsymbol{A} = \begin{bmatrix} 0 & 1 \\ -\frac{k^*}{I^*} & -\frac{C^*}{I^*} \end{bmatrix}, \quad \boldsymbol{B}_i = \begin{bmatrix} 0 \\ \frac{S_i^*}{I^*} \end{bmatrix}. \tag{4.45}$$

The goal is to drive the system from rest, $\boldsymbol{x}(0) = [0, 0]^\top$, to the target state $\boldsymbol{x}(T_f) = [\Delta\theta, 0]^\top$ while minimizing the input energy $\|u_i\|_{L_2}^2 = \int_0^{T_f} u_i^2(t)\, dt$. The optimal input satisfies

$$\|u_i\|_{L_2}^2 = \boldsymbol{x}_f^T \boldsymbol{W_c}^{-1} \boldsymbol{x}_f \tag{4.46}$$

$$\boldsymbol{W}_c = \int_0^{T_f} e^{\boldsymbol{A}t} \boldsymbol{B}_i \boldsymbol{B}_i^T e^{\boldsymbol{A}^T t} dt, \tag{4.47}$$

where $x_f = [\Delta\theta,\ 0]^\top$ is the final state and W_c is the finite-horizon controllability Gramian. Since B_i contains the scalar factor $\frac{S_i^*}{I^*}$, the Gramian can be factored as

$$\boldsymbol{W}_c = \left(\frac{S_i^*}{I^*}\right)^2 \boldsymbol{G}(T_f), \tag{4.48}$$

where $\boldsymbol{G}(T_f)$ depends only on the system dynamics ($\boldsymbol{A}$) and the time horizon T_f, but not on the crease index i. Substituting into the minimum-input energy expression yields

$$||u_i||_{L_2}^2 = \int_0^{T_f} u_i^2(t)\, dt = (\Delta\theta)^2 \left(\frac{I(\bar{\theta})}{S_i(\bar{\theta})}\right)^2 \alpha(T_f), \quad \text{with} \quad \alpha(T_f) = [\boldsymbol{G}^{-1}(T_f)]_{11}. \tag{4.49}$$

Therefore, we define the deployment efficiency index

$$e_t^{\mathrm{EL}} = \frac{1}{\|u_i\|_{L_2}^2} \propto S_i^2. \tag{4.50}$$

This relationship confirms that creases with higher kinematic ratio S_i require less control effort to achieve the same global displacement. It provides a clear physical interpretation of the deployment efficiency metric e_t^{EL}, which aligns with the intuition that actuation becomes more efficient when a crease induces greater global rotation per unit torque. For a single-cell rigid Miura-ori structure, the kinematic ratio S_i is plotted in Fig. 4.6(b) as a function of θ from the flat to the fully folded configuration. Starting from the zero-energy configuration of our model ($\theta = 45°$), creases 1 and 3 initially exhibit greater kinematic leverage than creases 2 and 4. As the origami continues to deploy, however, creases 2 and 4 eventually attain higher kinematic leverage.

4.6 Experimental setup of Miura-ori actuation

We verify this computational result via experiment. To build a physical setup, we first fabricate Miura-ori samples made of a thin sheet of stainless steel cut with a laser cutter (Bodor i5). To design the Miura-ori sample, we define the geometric parameters a, b, and α as 90 mm, 90 mm, and 60°, respectively. Also, the material parameters of stainless steel, such as the density ρ, Poisson's ratio ν, Young's modulus E, and panel thickness T, are given as 8000 kg/m^3, 0.27, 193 GPa, and 0.2 mm, respectively. To improve the elastic behavior of crease lines of metal Miura-ori structures, we employ lamina emergent torsional (LET) hinges to simulate the behavior of the origami crease lines [85, 86]. This is an improvement over a perforated compliant mechanism that non-metal origami structures often use [87]. The LET hinges allow the implementation of a linear torsional spring along the crease lines, as described in Section 4.6.2.

Fig. 4.7 illustrates the folding process of a metal Miura-ori sheet. In Fig. 4.7(a), a flat Miura-ori sheet made of stainless steel is shown. Fig. 4.7(b) depicts the 3D-printed jigs used to fold the crease lines. Fig. 4.7(c) demonstrates the application of these jigs along the crease lines, where plastic deformation is induced manually. After folding all crease lines, the fully folded Miura-ori unit cell is displayed in Fig. 4.7(d).

To test the scalability of our framework, we also perform experiments on two-cell and four-cell Miura-ori tessellations. The two-cell structure has ten crease lines (Fig. 4.9(a)), and the four-cell structure has 24 (Fig. 4.9(b)), each available for actuator implementation. In both cases, linear guide and green markers are mounted on a metal Miura-ori placed on a low-friction plastic plate, as shown in Fig. 4.9(c). With this setup and a servo motor, the experimental deployment efficiency e_{exp} is measured for each crease line in the case of the two-cell configuration. For the four-cell tessellation, two servo motors are mounted at different pairs of crease lines to ensure controllability. This dual actuation results in 276 possible crease line pairs. Ten representative pairs are selected at regular intervals of 27 from the lowest to the highest efficiency, based on the ranked list of theoretical deployment

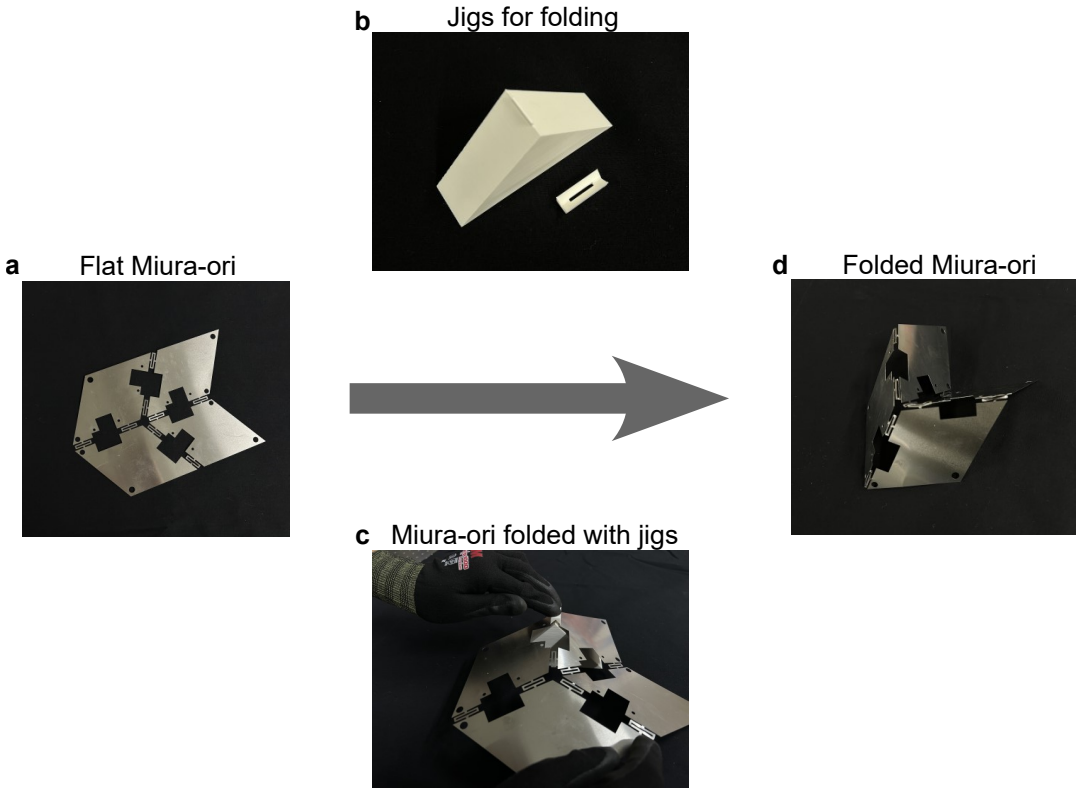

Figure 4.7: **a**, a flat metal sheet of Miura-ori unit cell cut with a laser cutter (Bodor i5). **b**, 3D-printed jigs for folding crease lines of Miura-ori. **c**, a Miura-ori unit cell being folded by hand with jigs. **d**, a folded metal Miura-ori unit cell.

efficiencies.

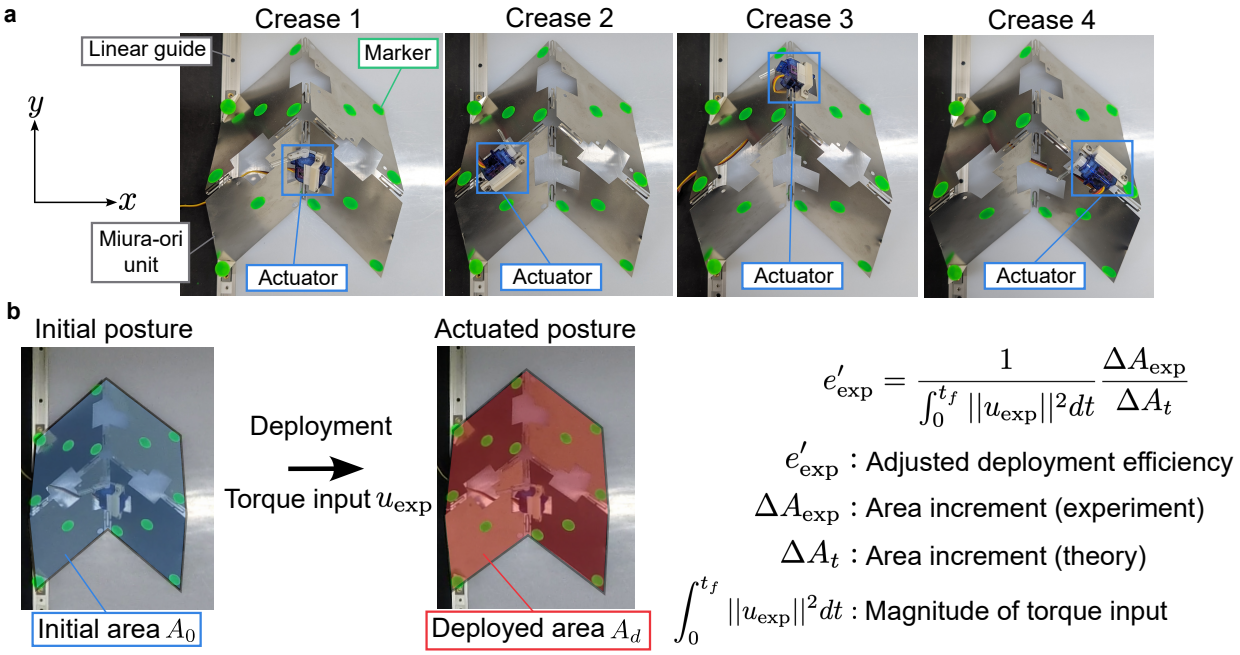

Figure 4.8: **a**, experiment setup for the actuation of a Miura-ori unit cell for deployment. A Miura-ori unit cell made of stainless steel is installed with an actuator, linear guide, and green marker to track dynamic behavior. **b**, schematic illustration of the measurement of the experiment. The initial area A_0 (blue shaded area) and deployed area A_d (red shaded area) are considered as the experimental area increment $\Delta A_{\exp} = A_d - A_0$ to calculate the adjusted deployment efficiency $e'_{\exp}$ along with the theoretical area increment ΔA_t as presented in Eq. (4.52).

Based on experimental measurements, we calculate $e_{\exp}$ as the inverse of the input energy obtained by integrating the squared applied torque over time:

$$e_{\exp} = \frac{1}{\int_0^{t_f} ||u_{\exp}||^2 dt}. \tag{4.51}$$

To account for the difference in the deployed area between the experiment and the theory,

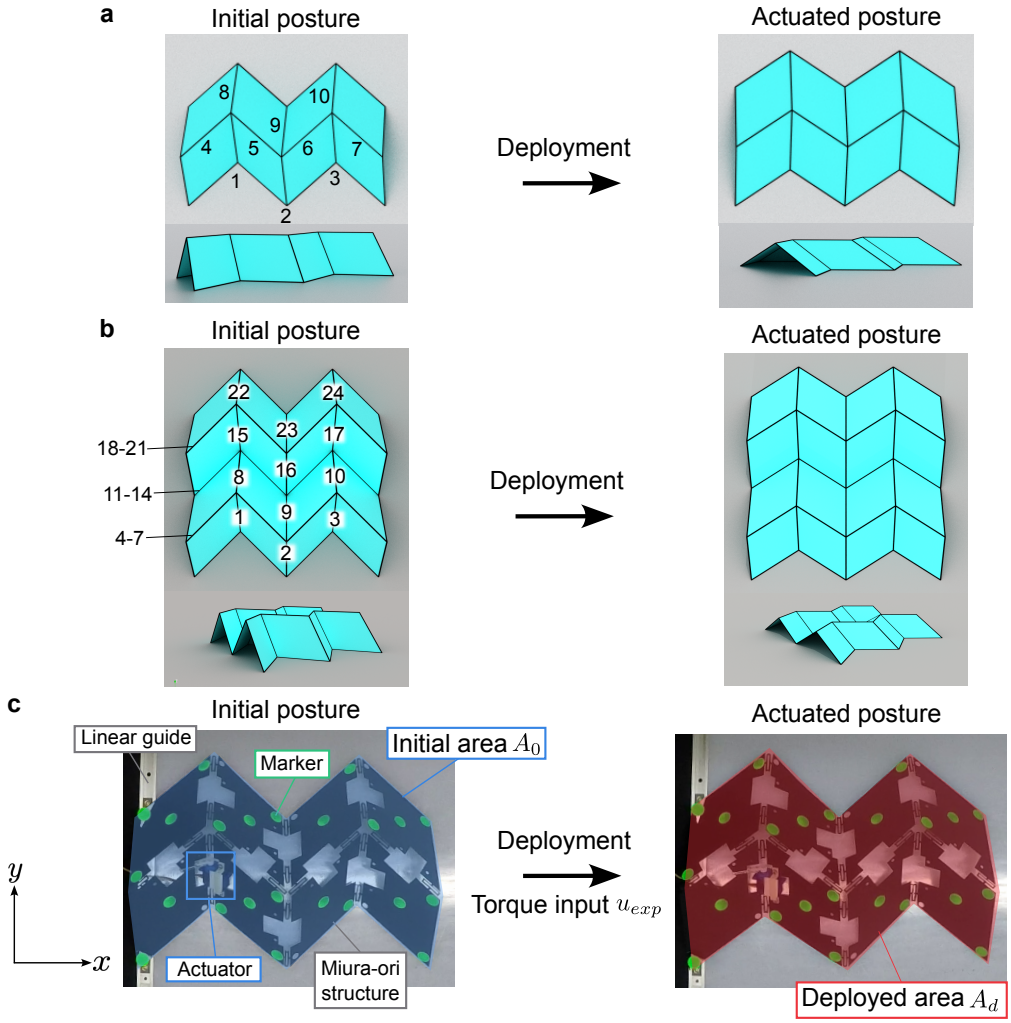

Figure 4.9: **a**, schematic of the deployment of the two-cell Miura-ori structure. **b**, schematic of a four-cell Miura-ori deployment. In both (a) and (b), crease lines are numbered sequentially from the bottom left to the top right, moving horizontally. **c**, experimental setup for the actuation of a two-cell Miura-ori deployment. The structure is installed with a linear guide, a servo motor, and green markers to track the dynamics. The Miura-ori structure, made of stainless steel, is colored with black paint to suppress the reflection of light. The initial area A_0 (blue shaded area) and deployed area A_d (red shaded area) are considered to calculate the adjusted deployment efficiency e'_{exp}.

we also define the adjusted deployment efficiency e'_{exp} as follows:

$$e'_{\text{exp}} = e_{\text{exp}} \frac{\Delta A_{\text{exp}}}{\Delta A_t}, \tag{4.52}$$

where ΔA_t is the increment of the deployed area in the theory. We utilize this adjusted e'_{exp} to quantify the deployment efficiency in each experimental case.

Fig. 4.10 shows the experimental setup for Miura-ori samples. Fig. 4.10(a)-(c) show a Miura-ori unit cell, a two-cell Miura-ori sample, and a four-cell Miura-ori sample, respectively. The metal Miura-ori unit samples are placed on a low-frictional Derlin plate to minimize the damping effect. The green markers are attached near the nodes of the bar-and-hinge model to track the dynamics of the structure with high-speed cameras (GoPro Hero 4). The left sides of the samples are attached to a linear guide to apply constraints to the system. We install a servo motor (SG51R) to each of the crease lines and deploy the miura-ori structure via the actuation of the servo motor. The servo motor is connected to a DC power supply set to 6V.

The camera setup is presented in Fig. 4.10(d). The GoPro camera is placed above the Miura-ori sample at a certain distance to capture the whole motion of the green markers on the sample. The captured videos are processed with OpenCV library. Fig. 4.10(e) shows the schematic illustration of the data-acquisition system for the Miura-ori samples. The actuator attached to the Miura-ori sample is controlled by an Arduino Uno microcomputer. The voltage-current sensor (INA219) is attached to the actuator to measure the operating voltage and current. For the four-cell dual-motor actuation, the two servo motors are connected in parallel, and the voltage-current sensor measures the combined current. The data from the sensor is sent to the computer (MacBook Pro) via an Arduino Mega microcomputer.

4.6.1 Adjustment of the mass matrix

In this section, we describe how to adjust the mass matrix of the system regarding the mass of the actuator. The Miura-ori unit cell, two-cell, and four-cell structures have masses of 26.2 g, 50.1 g, and 113.3 g, respectively. On the other hand, the actuator component we

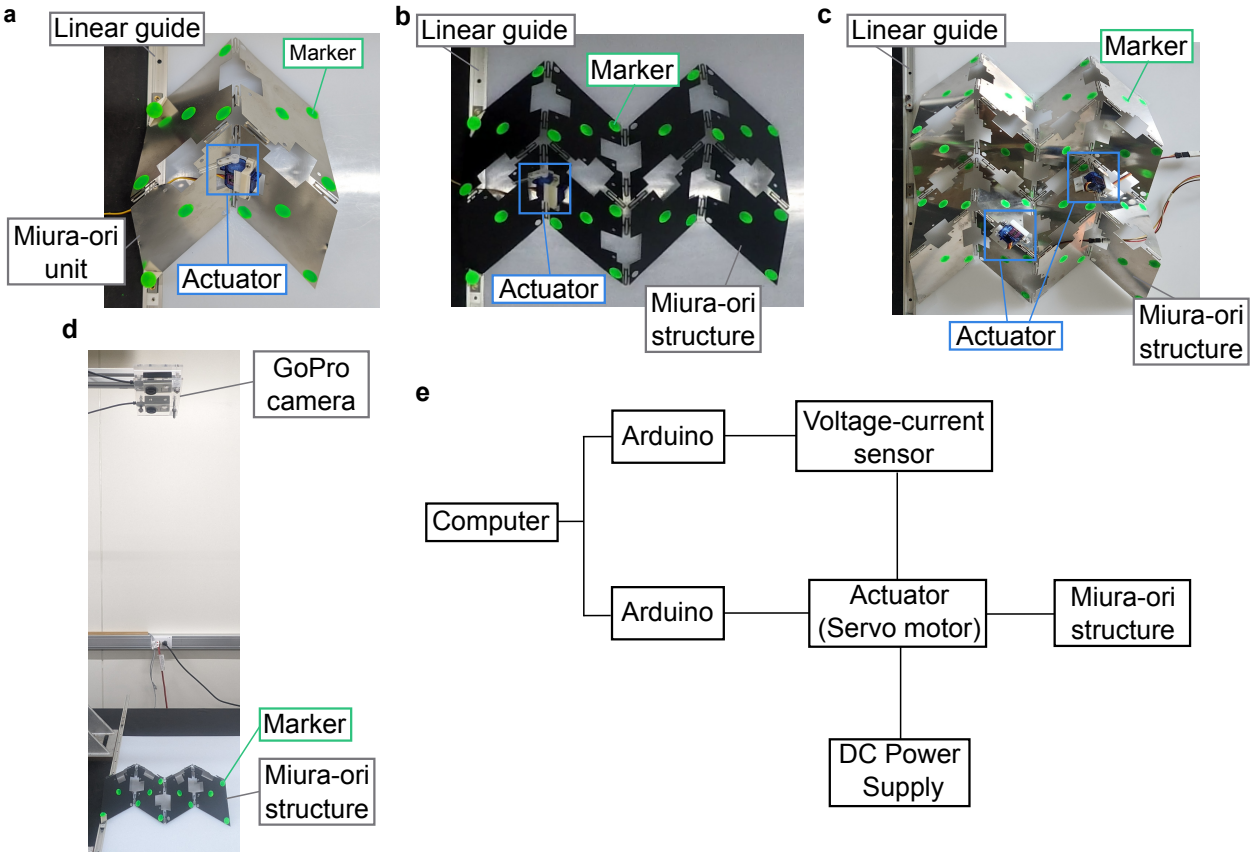

Figure 4.10: **a**, experimental setup for the actuation of a Miura-ori unit cell for deployment. **b**, experimental setup for the actuation of a two-cell Miura-ori deployment. **c**, experimental setup for the actuation of a four-cell Miura-ori deployment with dual actuation. **d**, setup of a high-speed camera (GoPro) to capture the dynamics of Miura-ori structures. **e**, schematic illustration of the data acquisition system for the dynamics of Miura-ori structures.

described in Section 4.6 and Fig. 4.10(a) weighs 6.1 grams. Thus, the mass of the actuator system is not negligible compared to the weight of the structure itself. Hence, it necessitates us to update the mass matrix of the system introduced in Section 4.3. Given the location of the actuation along one of the crease lines, we add a quarter of the actuator mass (1.525 g) for each nodal mass (node i, j, k, and l) that forms the actuated hinge element as shown in Fig. 4.4.

4.6.2 Compression test on lamina emergent torsional hinge

We perform compression tests on our LET hinge samples to measure their spring constants. The setup for the experiment is presented in Fig. 4.11(a). The crease line sample is attached to the load cell (LUX-B-200N-ID, Kyowa) with 3D printed fixtures. We apply vertical compression via the linear stage (BiSlider, Velmex). We model the sample of the crease line with two rigid panels connected by a nonlinear torsional spring as shown in Fig. 4.11(b). Then, the force-displacement relationship is modeled as follows:

$$F = \frac{2L^h k^h_{\text{crease}}(\theta - \theta_0)}{L\cos\theta}, \tag{4.53}$$

where $L^h = 50$ mm is the length of the crease line, $L = 35$ mm is the length of the sample, θ is the folding angle, and $\theta_0 = 51.8^\circ$ is the initial folding angle. Also, k_h is the linear spring coefficient per unit length. By applying the curve-fitting algorithm to the result of the compression test shown in Fig. 4.11(c), we obtain the spring constant $k^h_{\text{crease}} = 2.12$ [N/rad].

4.6.3 Estimation of the input torque via the voltage-current sensor

In this section, we describe how to estimate the input torque from the servo motor via the data from the voltage-current sensor. Based on the experimental setup described in the previous section, Fig. 4.12 shows an example of the experimental data obtained from the sensor in an experiment with an actuator installed on Crease 1. Fig. 4.12(a) and (b) are the time histories of the load voltage and current on the servo motor, respectively. Based on these time histories and the specification of the servo motor, we apply the coefficient to

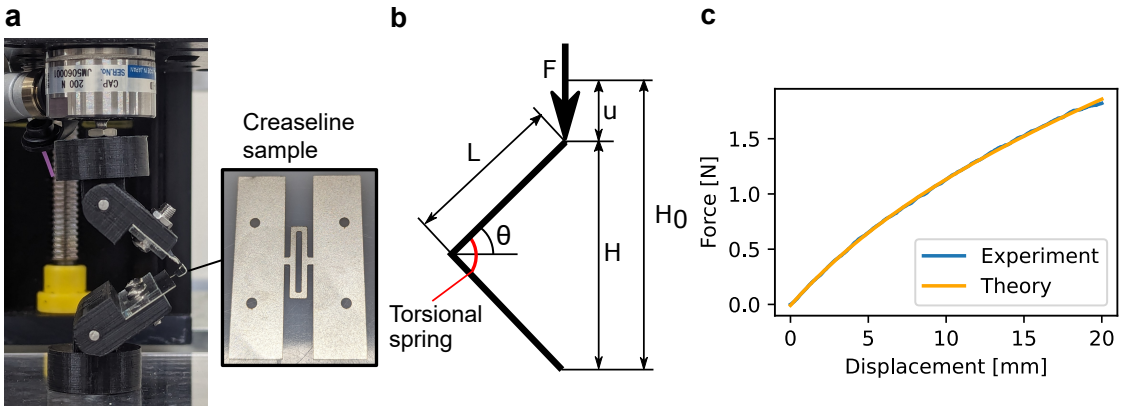

Figure 4.11: Setup of the compression test to measure the spring constant of the crease line. **a**, the picture of the experimental setup for the crease line sample. The inset of **a** shows the design of the sample of lamina emergent torsional hinge. **b**, the analytical model of the bending test of the crease line. The model is composed of two rigid panels and a linear torsional spring. **c**, the result of the compression tests for the sample. The blue solid line represents the mean value, whereas the colored area represents the standard deviation from the five experiments. The orange solid line represents the result of curve-fitting of the theoretical model.

convert the load current to the torque $c_{ct} = 1.63 \times 10^{-4}$ Nm/mA. The resulting time profile of the torque is shown in Fig. 4.12(c) as a blue curve. The deployment efficiency in experiment e_{exp} is computed by the summation of this time history of torque square. To supply the input torque to the computational model for a dynamic simulation discussed in the previous chapter, we approximate the time history of torque with a third-order polynomial fitting. The result of the fitting is presented as an orange curve in Fig. 4.12(c).

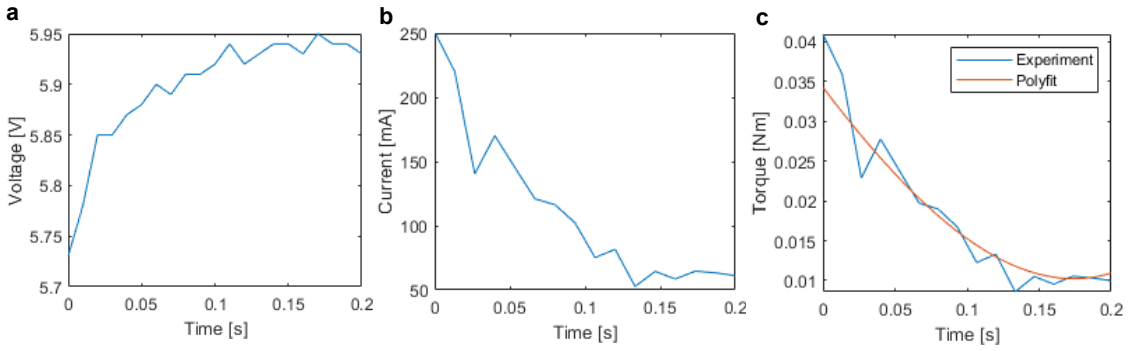

Figure 4.12: **a**, the load voltage profile of a servo motor during the actuation measured by the voltage-current sensor. **b**, the load current profile of a servo motor during the actuation measured by the voltage-current sensor. **c**, the torque profile generated by a servo motor. The blue curve presents the estimation from the experimental data shown in **a** and **b**, whereas the orange curve is the result of the third-order polynomial fit to the experimental data.

4.6.4 Experiment on a two-cell sample to measure the damping parameter

In this section, we describe how to estimate the damping parameter for a two-cell Miural-ori sample. To calibrate the computational model based on the bar-and-hinge model, we need to acquire the damping parameter from the experiment. To this end, we prepare the experiment setup as shown in Fig. 4.13. Fig. 4.13(a) shows the digital images of the experimentation to measure the damping parameter. The two-cell Miura-ori sample is folded from folding angle $\theta = 45^\circ$ to $\theta = 40^\circ$ with a thin nylon string. We release the string and observe the dynamics

of the structure that goes back to the zero-energy state ($\theta = 45°$).

To fit the numerical analysis to the experimental result, we utilize the dynamics of node 10 in the x-direction. The location of node 10 is indicated in Fig. 4.13(a). Fig. 4.13(b) presents the experimental and numerical behavior of node 10 in the x-direction. Here, the numerical analysis is fit to the experimental result with an optimization algorithm to minimize the error between the two results. Finally, we obtain the damping factor $\zeta = 0.164$ s^{-1} for our two-cell Miura-ori system.

4.7 Results and discussion

4.7.1 Dynamic behavior of Miura-ori unit cell

To confirm the validity of the bar-and-hinge model of Miura-ori and state-space representation, we first compare the computational simulation and experimental results of the dynamics of a Miura-ori unit cell. In experiments based on the setup shown in Fig. 4.8, we track the dynamic behavior of node 6 of a Miura-ori (as shown in Fig. 4.2(a)). Node 6, located centrally along the right edge of the structure, is selected for tracking as it effectively represents the overall dynamic response of the structure. The experiment of the deployment of a Miura-ori is conducted by installing an actuator to each crease line corresponding to Crease 1 to 4 in Fig. 4.8(a). The actuation of the servo motor is configured so that it changes the folding angle of the Miura-ori unit cell from $\theta_0 = 45°$ to $\theta_d = 40°$. We also perform the simulation of the dynamics of the deployment based on the state-space modeling presented in Eq. (4.25). To provide the input u_{in} to the simulation (see Eq. (4.25)), we estimate the time profile of the torque generated by the servo motor u_{exp} from the measurements of the voltage-current meter (see Section 4.6.3). The simulation is performed with the MATLAB linear simulator with the time step of $\Delta t = 10^{-5}s$. For each case of the actuator location, the mass matrix $\boldsymbol{M}$ in the simulation is corrected to account for the mass of the actuator unit (see Section 4.6.1).

Fig. 4.14(a)-(d) shows the result of the simulation and the experimental measurements of

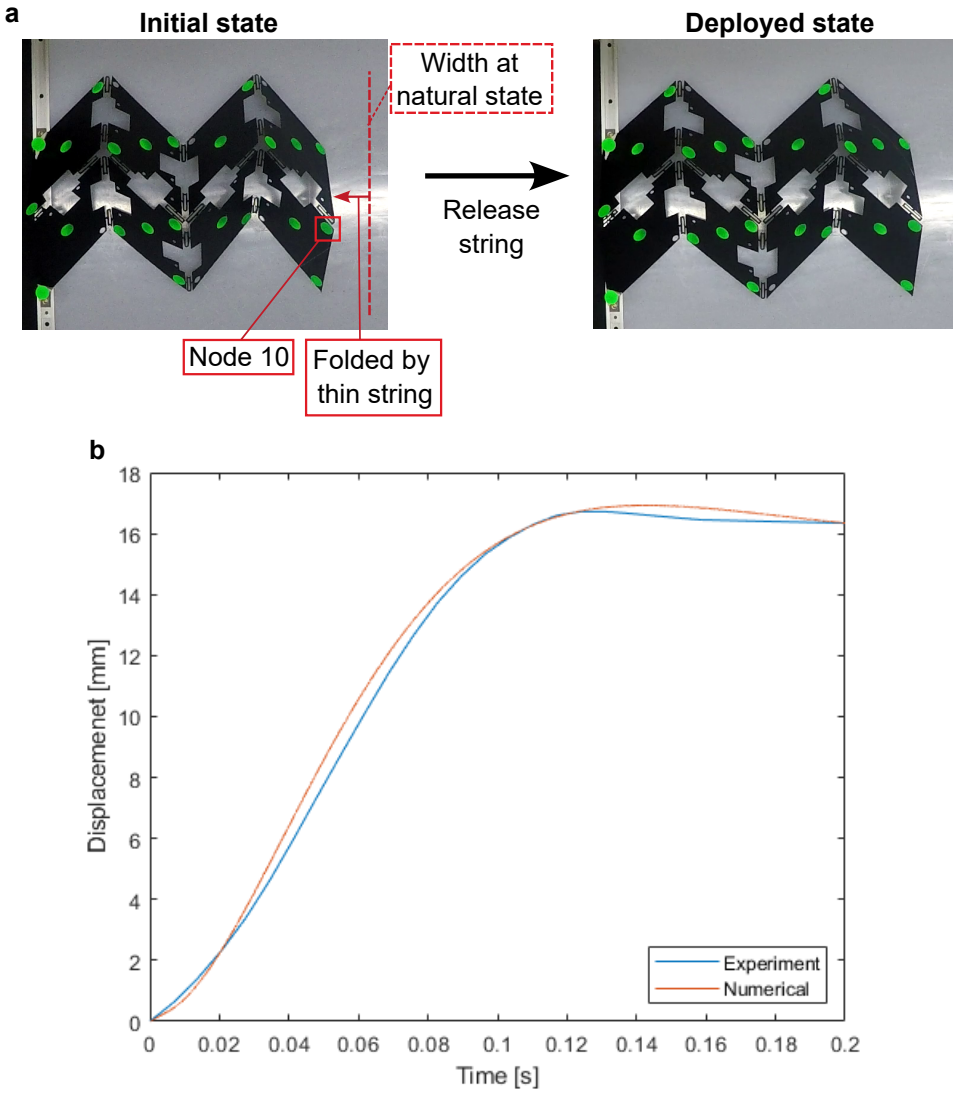

Figure 4.13: **a**, the schematic illustration of the experiment to measure the damping parameter of the system. **b**, the dynamic behavior of node 10 in the x-axis. Blue and orange solid lines represent the experimental and numerical results, respectively.

the dynamic behavior of node 6 with an actuator installed to crease lines 1 to 4, respectively. Here, we observe a good agreement between the simulation and experiment, regardless of the location of the actuator. The parameters for the bar-and-hinge model are defined as follows: $k^b = 1.93 \times 10^5$ N/m, $k^h_{\text{facet}} = 10.0$ N/rad, and $k^h_{\text{crease}} = 2.12$ N/rad. As described in the previous sections, k^b is the stiffness of the bar element obtained analytically (see Section 4.2.2). The parameters k^h_{crease} and k^h_{facet} are the per-unit-length rotational stiffness of the hinge element for the crease line and facet of Miura-ori, respectively. Here, k^h_{crease} is obtained via the compression test of the sample of the crease line, whereas k^h_{facet} is determined to fit the computational result to the experimental one presented in Fig. 4.14(a). We adopt this approach due to the challenges in analytically or experimentally determining the torsional stiffness of the hinge element within a facet. This fitted value of k^h_{facet} is then used as a fixed parameter for the computations in Fig. 4.14(b)-(d), with no further adjustments. Although each case (Fig. 4.14(a)-(d)) can have a different optimal damping parameter from each other, we use $\zeta = 0.157\ \text{s}^{-1}$ (from the experiment on Crease 1) for the numerical model to minimize the overall error and to have the unified evaluation of the controllability Gramian. These parameters are justified based on the good agreement between the experiment and computational results. This result supports the validity of the state-space modeling for small displacement scenarios, consistent with the scope of this study. While the deformation regime explored here is limited, it provides a foundational validation of the framework, motivating us to use this model to investigate the controllability of the system further.

4.7.2 Theoretical and experimental results on the deployment of Miura-ori structures

We summarize the theoretical analysis and experimental results on the efficiency of the single Miura-ori cell deployment in Fig. 4.15. Fig. 4.15(a) shows the theoretical ranking of the deployment efficiency e_t defined in Section 4.4. Through the analysis of the system via controllability Gramian, we identify that crease 1 (valley fold crease line) is the most efficient one for the deployment, followed by creases 3, 2, and 4. Based on the experimental setup presented in Section 4.6, Fig. 4.15(b)-(d) summarizes the experimental results and the

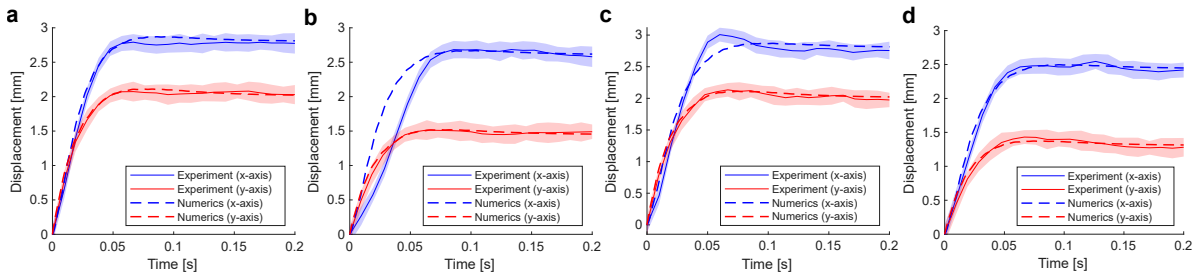

Figure 4.14: Dynamic behavior of node 6 on a Miura-ori unit cell during the deployment. **a**, the case of the actuation of crease line 1. **b**, the case of the actuation of crease line 2. **c**, the case of the actuation of crease line 3. **d**, the case of the actuation of crease line 4. Blue and red dashed lines represent the numerical results on the x-axis and y-axis, respectively. Blue and red solid lines and shaded areas represent the mean values and standard deviation of the experimental results on the x-axis and y-axis, performed five times, respectively.

adjustment process to validate the theoretical results in Fig. 4.15(a).

Fig. 4.15(b) shows the deployment efficiency in experiment e_{exp}. Based on the measurement from the voltage-current meter installed in the actuation system with a servo motor, we estimate the torque generated by the servo motor u_{exp} (see Section 4.6.3). From the time profile of the torque u_{exp}, we obtain the deployment efficiency e_{exp} as described in Eq. (4.51). Due to the difference in the location of the actuator and the direction of the motion of the servo motor, the impedance of the actuation is not uniform for each case. As this nature is predicted in Fig. 4.15(a), Fig. 4.15(b) results from the different magnitudes of input torque for each case. Although the ranking of the magnitude matches the theoretical prediction, the ratio of the magnitude differs between experimental and analytical results. This motivates us to consider applying an adjustment term to the result based on the deployed area.

Fig. 4.15(c) shows the measurement of the deployed area in the experiment ΔA_{exp}. For each location of the actuator, the angle of the servo motor is set to change from $\theta_0 = 45^\circ$ to $\theta_d = 40^\circ$. Therefore, the theoretical deployed area ΔA_t is the same for all cases. However, due to the open-loop input of the current state of our experiment, we experience deviations

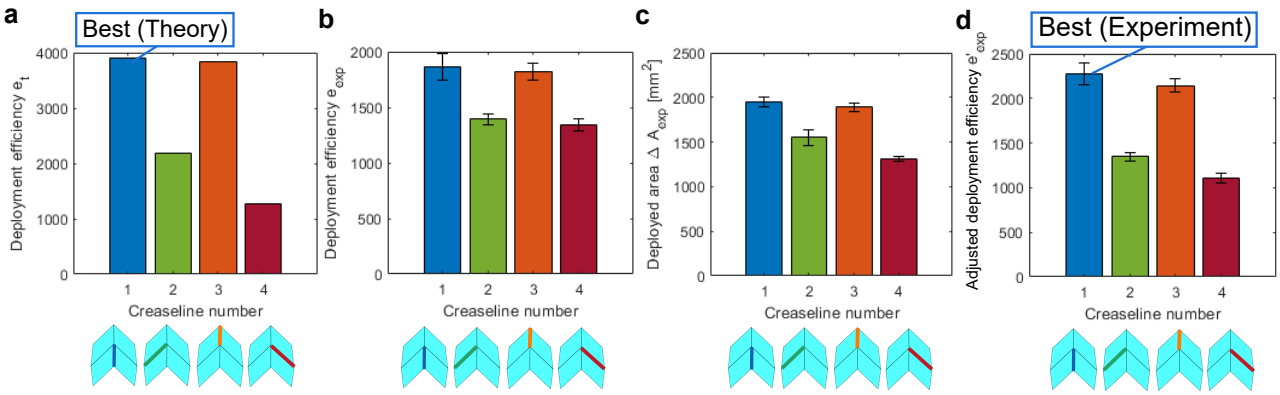

Figure 4.15: Theoretical and experimental results on a Miura-ori unit cell. **a**, the theoretical ranking of the deployment efficiency e_t. The color of the bar graph corresponds to the location of the crease lines shown in the inset below the graph. **b**, the deployment efficiency measured in experiment e_{exp}. **c**, the measurement of deployed area in the experiment ΔA_{exp}. **d**, the adjusted deployment efficiency measured base on the deployed area e'_{exp}. Black bars in **b** - **d** represent the standard deviation of the experiment repeated five times.

in experimental results from the theoretical values. This results in the unequal deployed area in Fig. 4.15(c). We utilize the difference of the deployed area for each case to account for the difference in the actuation and reflect it in the deployment efficiency (see Eq. (4.52)). Also, we observe that the deployment efficiency in experiment (Fig. 4.15(b)) and areal change (Fig. 4.15(c)) are in agreement. This is because the lower energy consumption leads to easier deployment, which in turn results in a larger deployed area.

Fig. 4.15(d) presents adjusted deployment efficiency in experiment e'_{exp} as described in Eq. (4.52). Based on the result shown in Fig. 4.15(b), we correct the magnitude of input torque regarding the difference of the increment of the projected area ΔA_{exp} presented in Fig. 4.15(c). By applying the adjustment term, we observe better matching between deployment efficiency e_t (Fig. 4.15(a)) and e'_{exp} (Fig. 4.15(d)) in terms of the ratio of the magnitude for each case. By summing up these results shown in Fig. 4.15(b)-(d), we find that actuating crease 1 is the most efficient. The subtle discrepancy between theoretical and experimental

deployment efficiencies arises primarily from differences in the input profiles. The theoretical efficiency assumes the minimum-energy input as calculated from Eq. (20). However, due to technical challenges in precisely realizing this theoretical minimum-energy input in experiments, the actual input profile differs. These deviations can be attributed to actuator limitations, friction, or other practical constraints in the experimental setup. Despite the differences in efficiency values, the agreement in the ranking of deployment efficiencies between theoretical and experimental results demonstrates the applicability of the proposed method for identifying efficient crease lines for actuation. This consistency indicates that the theoretical framework provides meaningful insights into the optimal placement of actuators.

To further validate the efficacy of this approach in a larger tessellation, we perform and summarize the theoretical analysis and experimental results on two-cell tessellations in Fig. 4.16. Fig. 4.16(a)-(d) shows the theoretical ranking of the deployment efficiency e_t, the deployment efficiency in experiment e_{exp}, deployed areas in experiment ΔA_{exp}, and adjusted deployment efficiency e'_{exp}, respectively. In Fig. 4.16(a) and (b), the deployment efficiency rankings from theoretical predictions and experimental results do not fully match. However, when we apply the adjustment term from Eq. (4.52) based on the deployment area (Fig. 4.16(c)), the results show strong agreement theory and experiments, as shown in Fig. 4.16(a) and (d). In this case, crease 5 (a mountain crease line) emerges as the most efficient for deployment, followed by crease 9. In contrast, creases 3 and 10, which are located far from the node constraints, exhibit the lowest efficiency. The parameters for the bar-and-hinge model (k^b, k^h_{facet}, and k^h_{crease}) are the same as the unit-cell case, except for the damping parameter $\zeta = 0.164\ \text{s}^{-1}$, which we particularly obtained for the two-cell system (see Section 4.6.4). These results suggest that the model can reliably predict efficient actuation sites beyond the unit cell.

We next extend the approach to a multi-actuator scenario. Fig. 4.17 presents the theoretical and experimental deployment efficiency for the four-cell Miura-ori tessellation. Under the dual-actuator configuration, the heatmap in Fig. 4.17(a) shows the theoretical deployment efficiency e_t computed for all 276 possible crease line pairs, with red indicating higher

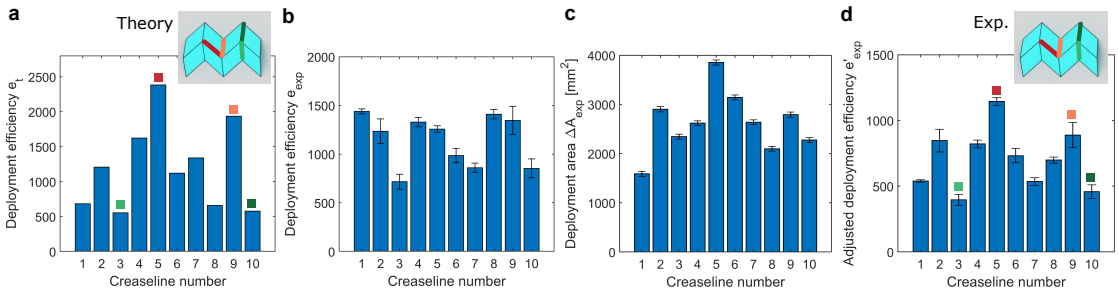

Figure 4.16: Theoretical and experimental results on a two-cell Miura-ori structure. **a**, the theoretical deployment efficiency e_t for each crease line. **b**, experimentally measured deployment efficiency e_{exp}. **c**, the measured deployed area in the experiment ΔA_{exp}. **d**, the adjusted deployment efficiency measured based on the deployed area e'_{exp}. Colored square markers in a and d denote performance rankings: red for the most efficient crease (crease 5), orange for the second (crease 9), green for the least efficient (crease 3), and dark green for the second least efficient (crease 10). Black bars in **b** - **d** represent the standard deviation of the experiment repeated fifteen times.

values. Based on this ranking, ten representative pairs are selected for experimental validation at regular intervals, as shown in Fig. 4.17(b). Among these, the pairs (8, 23) and (5, 8) exhibit the highest and lowest theoretical efficiencies, respectively, as highlighted in Fig. 4.17(c). It is noteworthy that crease line 8 serves as the actuator placement in both the most and least efficient cases, a result that underscores the sophistication of the proposed controllability strategy. The parameters for the bar-and-hinge model, including the damping coefficient, remain the same as in the two-cell case. Fig. 4.17(d)–(f) show the experimentally measured deployment efficiency e_{exp}, the deployed area ΔA_{exp}, and the adjusted deployment efficiency e'_{exp}, respectively.

As shown in Fig. 4.17(f), the ranking of the adjusted deployment efficiency e'_{exp} across the ten tested crease line pairs closely follows the theoretical ranking of e_t in Fig. 4.17(b). The most efficient pair (8, 23) achieved the highest adjusted deployment efficiency experimentally, whereas the least efficient pair (5, 8), comprising two adjacent creases, showed the lowest. Both results are consistent with theoretical predictions. Efficient crease pairs such as (8, 23) and (7, 18) tend to be spatially distributed, aligning with the intuition that broader actuation across the structure is more effective than localized input. In contrast, the least efficient cases include (8, 9), where two actuators are placed adjacent to each other, and (5, 8), where they share the same vertex. Notably, the experiments reveal up to a four-fold variation in e'_{exp} between the most and least efficient cases, underscoring the importance of optimal actuator placement in larger tessellations. Minor discrepancies in e'_{exp} are observed for low-efficiency pairs such as (5, 10) and (8, 9). For these pairs, the theoretical values differ by less than 50 in e_t values, making them difficult to distinguish experimentally. This is likely due to experimental limitations, particularly the use of a deployed area-based adjustment term and the presence of friction effects, which may lack the resolution needed to capture such subtle variations. Despite these deviations, the overall agreement in ranking across most tested pairs indicates that our framework provides a scalable and predictive tool for designing efficient, multi-actuated origami systems.

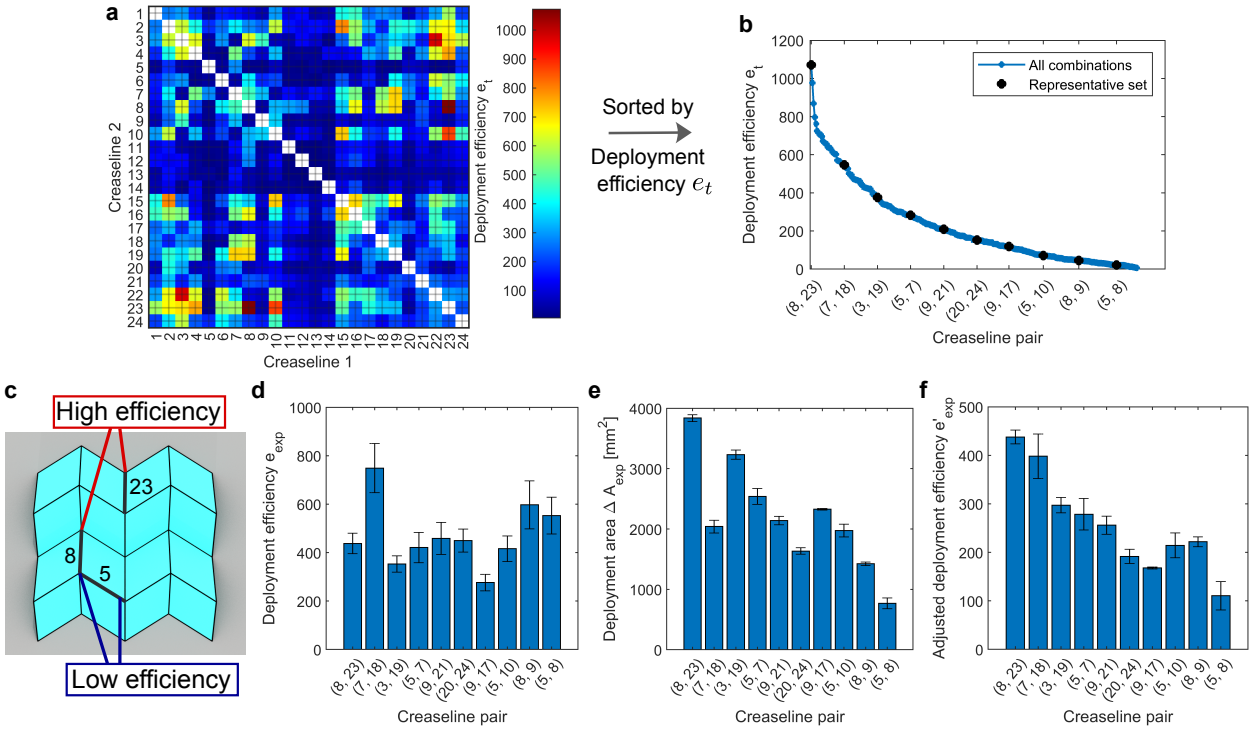

Figure 4.17: Theoretical and experimental results on a four-cell Miura-ori structure with dual-motor actuation. **a**, heatmap of theoretical deployment efficiency e_t for all crease line pairs (red: high, blue: low). **b**, ten representative pairs (black dots), selected based on the ranking of e_t, are used for the experiments. **c**, the highest-efficiency pair (8, 23) and the lowest-efficiency pair (5, 8) among the selected sets. **d**, experimentally measured deployment efficiency e_{exp} for each selected pair. **e**, the measured deployed area in the experiment ΔA_{exp}. **f**, the adjusted deployment efficiency e'_{exp} calculated based on the deployed area. Black bars in **d** - **f** represent the standard deviation from fifteen repeated experiments.

4.7.3 Large-Deployment Analysis via Piecewise Linearization

In addition to the small-displacement problems discussed above, we extend our framework to address the large-deployment behavior, a key characteristic of origami structures. As described in Section 4.4, the theoretical deployment efficiency e_t during large-deformation motion is analyzed using a piecewise-affine linearization approach. To facilitate the large-deployment analysis, we revert to the single-cell setting of a Miura-ori unit. Fig. 4.18(a) illustrates the piecewise-affine linearization process from the zero-energy state ($\theta_0 = 45^\circ$) to the fully deployed configuration ($\theta_d = 0^\circ$). The full deployment process is divided into 15 segments, each corresponding to a 3° decrement in the folding angle θ. The parameters for the bar-and-hinge model (k^b, k^h_{facet}, k^h_{crease}, and ζ) are the same as the small-displacement unit cell case. We also consider intermediate displacements of $\Delta\theta = 10^\circ$, 15°, and 30°, with each case discretized into 3, 5, and 10 equal segments, respectively. The finite-time horizon controllability Gramian for each segment is computed over $T_f = 5\,\text{s}$, which ensured numerical stability in computing its inverse across all segments.

For consistent comparison across four different deployment cases, the deployment efficiency e_t is normalized such that the most efficient crease line at each deployment case is scaled to one. As shown in Fig. 4.18(b), crease lines 1 and 3 exhibit higher deployment efficiency during the early stages of deployment. However, the efficiency of crease lines 2 and 4 gradually increases as the structure continues to unfold. Ultimately, in the full deployment case, crease lines 2 and 4 outperform crease lines 1 and 3 in terms of deployment efficiency.

To interpret these trends, we analytically evaluate deployment efficiency e_t^{EL} using the Euler–Lagrange framework described in Section 4.5. Fig. 4.18(c) shows the normalized deployment efficiency e_t^{EL} evaluated over range $\theta = 45^\circ$ to $\theta = 35^\circ$. The e_t^{EL} is integrated over the interval $\Delta\theta = 10^\circ$ for each crease line, and normalized such that the maximum value across all crease lines is scaled to one. Fig. 4.18(d) presents the normalized e_t^{EL} evaluated over the full range of $\theta = 45^\circ$ to $\theta = 0^\circ$. As a result, crease lines 1 and 3 exhibit greater efficiency in the early stages of deployment, while creases 2 and 4 become dominant in the

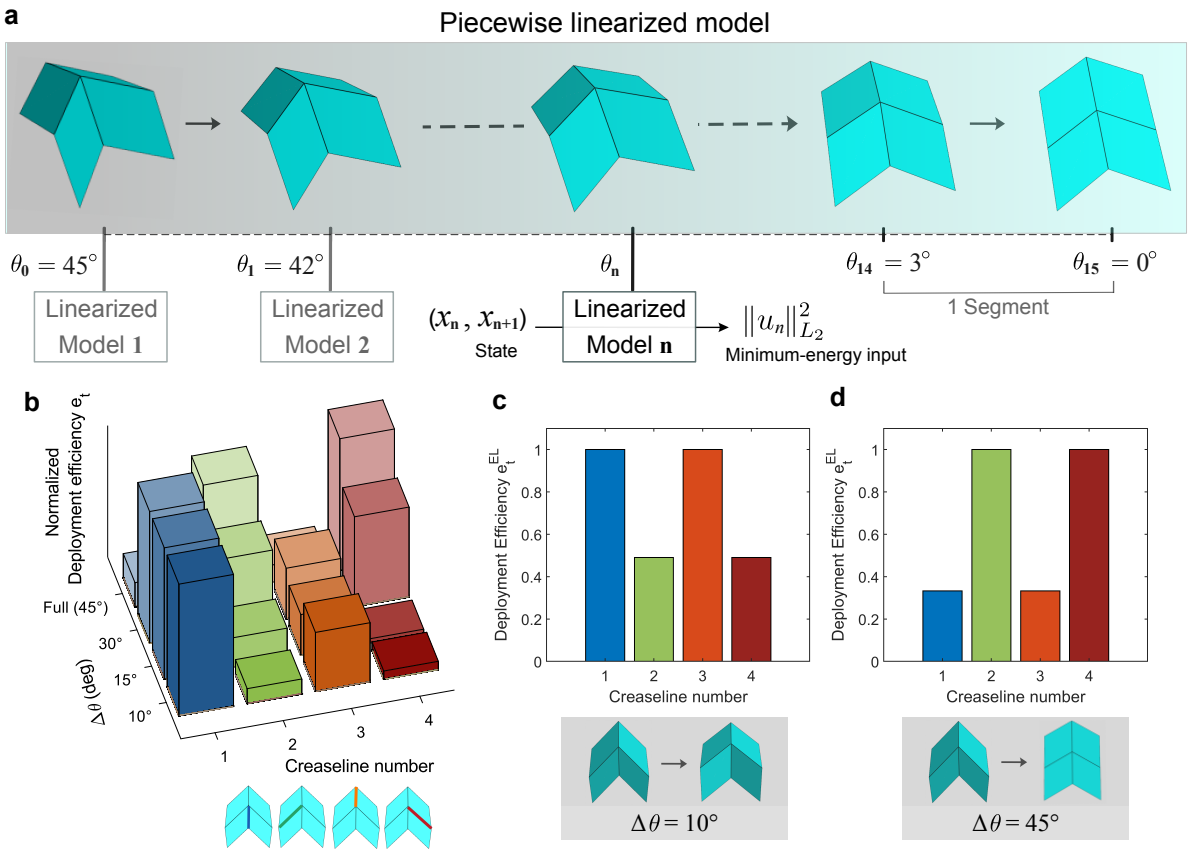

Figure 4.18: **a**, schematic of the piecewise-linearization approach for the full deployment case ($\Delta\theta = 45°$). Deployment from the neutral state $\theta_0 = 45°$ to the flat state $\theta_{15} = 0°$ is discretized into 15 intervals. Each segment is approximated by a linearized model to compute the minimum-energy input $\|u_n\|^2_{L_2}$. **b**, normalized deployment efficiency e_t for four $\Delta\theta = 10°, 15°, 30°, 45°$ cases. Crease lines 1 and 3 are more efficient at small deformation, whereas crease lines 2 and 4 dominate in the full deployment case. **c**, normalized deployment efficiency e_t^{EL} results using the Euler–Lagrange formulation at $\Delta\theta = 10°$, showing high efficiency in crease lines 1 and 3. **d**, normalized deployment efficiency e_t^{EL} at $\Delta\theta = 45°$, where crease lines 2 and 4 become dominant.

fully deployed case. This shift is explained by the evolution of the kinematic leverage, S_i. At $\theta = 45°$, S_i is greater for creases 1 and 3, but beyond a critical angle ($\theta \approx 35.25°$), the S_i values for creases 2 and 4 exceed those of creases 1 and 3. The complete variation of S_i over the full kinematic folding range is shown in Fig. 4.6. As boundary conditions are not incorporated in this framework, symmetrically placed creases yield identical efficiency values. Nevertheless, the observed ranking of deployment efficiency aligns closely with the theoretical control efficiency e_t predicted by the state-space model. Importantly, this controllability Gramian-based framework captures the physical intuition that creases producing greater motion per unit torque are inherently more efficient for actuation. This consistency supports the validity of our computational approach and provides insight into actuator placement strategies for large-deformation origami systems. Further analytical and experimental validations in this regime remain a promising direction for future work.

4.8 Conclusion

In this work, we demonstrate how to analyze the controllability of the origami dynamics. In particular, we propose a computational framework to find the efficient crease line for the deployment through actuation. Due to its flexible nature, it is often difficult to investigate control problems of origami structures. To this end, we discretize the Miura-ori structure with the bar-and-hinge model, a low-dimensional mechanical model, to capture the dynamic behavior of origami. Based on this model, we derive the state-space representation of the Miura-ori dynamics. The state-space representation is utilized to obtain the controllability Gramian, enabling us to theoretically evaluate the efficiency of the deployment for each crease line. Thus, we can find the best location to place an actuator based on this result. To verify these findings, we design an experimental setup with Miura-ori structures made of stainless steel for the small-displacement cases. By measuring the magnitude of actuation input by a servo motor and the deployed area, we evaluate the deployment efficiency experimentally. Under the small-displacement scenarios, the agreement between the computational and experimental results in one, two, and four-cell configurations is demonstrated, supporting the

validity of this computational framework. The analytical results for the large-deployment scenarios motivate further analytical and experimental investigation.

In conclusion, this computational framework lays a foundation for controlling nonlinear origami dynamics and designing actuation systems for large-scale deployments of origami tessellations. First, we validate the framework in small-displacement cases through linearization around the equilibrium configuration and experimental tests. Then, we extend the framework to address large deformation behaviors, an essential feature of origami structures, using a piecewise linearization approach. The 1-cell large deployment scenario is compared against a first-principles model based on the Euler–Lagrange equation, indicating the framework's capability to capture essential controllability characteristics of the system. Looking ahead, we acknowledge that there are two major directions to advance this research. One is further experimental work and expansion of the method to address the large deformation problems and more complex origami architectures, as they exhibit rich, nonlinear dynamics that are vital for advanced applications. Addressing these challenges will require accommodating diverse material properties, initial geometries, and detailed crease-line mechanics, alongside managing increased computational demands. The other is integrating system observation and feedback control into the framework for robust and accurate control of origami actuation. While this study focuses solely on actuation, sensing mechanisms to observe system states and enable real-time feedback adjustments would enhance the control of origami structures under practical conditions. Combining these two aspects can pave the way for further real-world applications of origami in robotics, aerospace, and biomedical engineering. For instance, deployable satellite components, soft robotic arms, and medical devices can benefit from optimized actuation strategies.

4.9 Author contributions

This chapter is based on the paper: K. Yamaguchi, S. Jeong, Y. Miyazawa, Y. B. Oh, R. Dai, M. Mesbahi, J. Yang, "Controllability analysis of origami dynamics via state-space modeling," Materials & Design (2025) [88]. K.Y and J.Y conceived the idea of this project. The

theoretical and numerical studies were performed by K.Y, S.J, and Y.M. The experiments were carried out by K.Y, S.J., and Y.O. The original draft writing was carried out by K.Y. and S.J. K.Y, S.J, Y.O, and J.Y contributed to the review and editing of the manuscript. J.Y supervised the project. All authors contributed to the paper with valuable inputs.

Chapter 5
CONCLUSIONS AND OUTLOOK

5.1 Conclusions

This dissertation has explored the integration of origami principles into the design, tuning, and control of mechanical metamaterials, addressing key challenges in efficient design exploration, post-fabrication tunability, and dynamic actuation. The key research accomplishments can be summarized as follows:

1. We developed a graph-theoretic framework for efficient design space exploration of origami-based metamaterials using the Tachi–Miura Polyhedron (TMP) as a model system. This framework effectively addresses the combinatorial explosion of possible fold configurations by representing each unit cell's phase and connectivity in a graph. It enables the identification of geometrically valid tessellations from an otherwise astronomical number of configurations. In doing so, we demonstrated the reconfigurability of TMP tessellations, showcasing how a single assembled lattice can morph into diverse shapes through different combinations of local unit-cell states. This graph-based design method provides a systematic and computationally tractable approach to discover metamaterial architectures with targeted properties and reconfiguration capabilities.

2. We introduced a post-fabrication thermomechanical tuning method that allows dramatic adjustment of a TMP metamaterial's effective stiffness and density after it has been manufactured. Through heat-processing techniques, we demonstrated an exceptionally wide in-situ tunability range within the elastic regime – including an approximately 60-fold change in Young's modulus (stiffness) and about a 10-fold change in effective density. Notably, we observed an inverse correlation between density and

stiffness in the tuned states: as the cellular lattice expands and its density decreases, its effective stiffness paradoxically increases (and vice versa). This study offers insight into designing metamaterials with customizable mechanical characteristics on demand. A single physical sample can thus be reprogrammed to exhibit different mechanical behaviors, which is a significant step toward adaptive material systems.

3. We developed a state-space modeling and controllability framework for the dynamic actuation of origami-based metamaterials, focusing on a Miura-ori fold pattern. By discretizing the Miura-ori structure into an interconnected network of masses, bars, and hinges, we obtained a low-dimensional state-space representation that captures the system's transient dynamics. Using this model, we analyzed the controllability of the origami mechanism that essentially quantifies how effectively external inputs (actuators) can drive the structure's configuration. From the controllability analysis, we proposed strategies for optimal actuator placement, identifying which crease lines to actuate to achieve the most efficient deployment of the origami structure. We validated these strategies experimentally: the theoretically predicted best actuation sites corresponded to lower energy consumption and more effective motion in physical tests. Furthermore, we extended the framework to account for large deformations, laying the groundwork for controlling origami metamaterials in their entire operating conditions. This controllability study bridges the gap between metamaterial design and active control, showing that even highly flexible, multi-degree-of-freedom structures like origami can be harnessed for predictable, engineered motion.

Collectively, these contributions advance the field of origami-inspired mechanical metamaterials on three fronts – design, tunability, and controllability. By addressing each of these aspects, we move closer to the vision of intelligent, adaptable mechanical systems. In essence, the dissertation demonstrates that it is possible to program the behavior of origami-based mechanical metamaterials: we can algorithmically design their architecture for reconfigurability, finely tune their material response post-fabrication, and analyze controllability to place

actuators intelligently. This synergy of structure, material, and control is a step toward realizing engineered materials that can change their properties or geometry on demand to meet specific tasks or environmental conditions. While challenges remain, the work presented here lays a foundation for mechanical systems that are not static objects but rather adaptive and responsive entities.

5.2 Outlook

Lastly, we briefly discuss potential directions to advance programmable origami metamaterials across design, tuning, and control:

1. *Graph-based inverse design methodologies for reconfigurable tessellations*: The next step is to elevate the current enumerative framework into a full inverse-design and optimization pipeline. The graph representation presented in Chapter 2 can be coupled with multi-objective search (e.g., Pareto optimization) to target not only geometric validity but also property sets such as effective stiffness, density, Poisson's ratios, and reconfiguration pathways. Embedding manufacturing and tolerance constraints (panel thickness, minimum hinge radius, allowable crease curvature, self-contact avoidance) will make the search outcomes fabrication-ready. Extending the graph rules to additional unit types (phase variants, defects, boundary/transition cells) will enable heterogeneous, functionally graded lattices and systematic design of domain walls and interfaces.

   Also, given the simplicity of the graph-based framework, it can be applied to the other types of the tessellations of mechanical metamaterials (e.g., metal-organic hinged cube tessellation [62], voxelated mechanical metamaterials [14, 63, 89], and other origami lattices in 2D or 3D settings [18, 19, 31, 64, 65]) by building graph representations for each architecture of mechanical metamaterials and by understanding the connections within the tessellations.

2. *From homogeneous architectures to spatially tunable, multiscale platforms*: Although we have explored uniform homogeneous architectures in Chapter 3, we envision the pos-

sibility of locally tuning properties using the same units. The dimensionless working principle of TMP metamaterial enables its application on both large scales, such as space structures and automotive airbags, and small scales, like the micro-structure of artificial bones (meta-implants [56]). The search for heterogeneous architectures can be well combined with the graph-based methods presented in Chapter 2.

Furthermore, while we consider the linear-elastic region, combining post-fabrication tuning, nonlinear finite element analysis, and data-driven design of metamaterials [75, 76] can unlock the full potential of this metamaterial. The broad tunability of mechanical properties offers further possibilities for employing this metamaterial as a highly adaptable engineering platform.

3. *Closed-loop, large-deformation control of origami lattices*: Building on the controllability analysis and optimal actuator placement, the next phase is feedback control with sensing. This entails co-designing actuator–sensor layouts and deploying state estimation to cope with unmeasured states. With these elements in place, robust and constrained controllers (e.g., Linear-quadratic Regulator/Model-predictive Control) can achieve precise, energy-aware deployment and reconfiguration while explicitly handling input limits, contact events, and path feasibility.

   To address large, configuration-dependent deformations, we generalized the linear models to a piecewise-affine form. It can further be complemented by data-driven reductions (e.g., DMD-based or Koopman-inspired methods) that preserve essential folding kinematics. Experimental milestones include scaling from a few-cell to dozens-of-cell arrays, verifying energy-benefit predictions, and demonstrating trajectory tracking across wide configuration ranges, and application to other origami architectures. Ultimately, integrating the control stack with the tuning methods of Chapter 3 will enable co-optimization of where to actuate and what to program, yielding minimal-energy, high-fidelity shape change in complex origami lattices.

BIBLIOGRAPHY

[1] M. I. Hussein, M. J. Leamy, M. Ruzzene, Dynamics of phononic materials and structures: Historical origins, recent progress, and future outlook, Applied Mechanics Reviews 66 (4) (2014) 040802. doi:10.1115/1.4026911.

[2] S. Babaee, N. Viard, P. Wang, N. X. Fang, K. Bertoldi, Harnessing Deformation to Switch on and off the Propagation of Sound, Advanced Materials 28 (8) (2016) 1631–1635. doi:10.1002/adma.201504469.

[3] O. R. Bilal, A. Foehr, C. Daraio, Reprogrammable Phononic Metasurfaces, Advanced Materials 29 (39) (2017). doi:10.1002/adma.201700628.

[4] Z. Wu, Y. Zheng, K. W. Wang, Metastable modular metastructures for on-demand reconfiguration of band structures and nonreciprocal wave propagation, Physical Review E 97 (2) (aug 2018). doi:10.1103/PhysRevE.97.022209.

[5] Z. Liu, X. Zhang, Y. Mao, Y. Y. Zhu, Z. Yang, C. T. Chan, P. Sheng, Locally resonant sonic materials, Science 289 (5485) (2000) 1734–1736. doi:10.1126/science.289.5485.1734.

[6] T. Frenzel, J. David Brehm, T. Bückmann, R. Schittny, M. Kadic, M. Wegener, Three-dimensional labyrinthine acoustic metamaterials, Applied Physics Letters 103 (6) (2013) 61907. doi:10.1063/1.4817934.

[7] X. Zheng, H. Lee, T. H. Weisgraber, M. Shusteff, J. DeOtte, E. B. Duoss, J. D. Kuntz, M. M. Biener, Q. Ge, J. A. Jackson, S. O. Kucheyev, N. X. Fang, C. M. Spadaccini, Ultralight, ultrastiff mechanical metamaterials, Science 344 (6190) (2014) 1373–1377.

[8] K. Bertoldi, V. Vitelli, J. Christensen, M. V. Hecke, Flexible mechanical metamaterials, Nature Reviews Materials 2 (10 2017). doi:10.1038/natrevmats.2017.66.

[9] B. Haghpanah, H. Ebrahimi, D. Mousanezhad, J. Hopkins, A. Vaziri, Programmable elastic metamaterials, Advanced Engineering Materials 18 (2016) 643–649. doi:10.1002/adem.201500295.

[10] A. Farzaneh, N. Pawar, C. M. Portela, J. B. Hopkins, Sequential metamaterials with alternating poisson's ratios, Nature Communications 13 (12 2022). doi:10.1038/s41467-022-28696-9.

[11] Q. Wang, J. A. Jackson, Q. Ge, J. B. Hopkins, C. M. Spadaccini, N. X. Fang, Lightweight mechanical metamaterials with tunable negative thermal expansion, Physical Review Letters 117 (10 2016). doi:10.1103/PhysRevLett.117.175901.

[12] J. I. Lipton, R. MacCurdy, Z. Manchester, L. Chin, D. Cellucci, D. Rus, Handedness in shearing auxetics creates rigid and compliant structures, Science 360 (6389) (2018) 632–635. doi:10.1126/science.aar4586.

[13] J. T. B. Overvelde, J. C. Weaver, C. Hoberman, K. Bertoldi, Rational design of reconfigurable prismatic architected materials, Nature 541 (7637) (2017) 347–352. doi:10.1038/nature20824.

[14] N. Yang, C. W. Chen, J. Yang, J. L. Silverberg, Emergent reconfigurable mechanical metamaterial tessellations with an exponentially large number of discrete configurations, Materials and Design 196 (nov 2020). doi:10.1016/j.matdes.2020.109143.

[15] J. T. Overvelde, T. A. de Jong, Y. Shevchenko, S. A. Becerra, G. M. Whitesides, J. C. Weaver, C. Hoberman, K. Bertoldi, A three-dimensional actuated origami-inspired transformable metamaterial with multiple degrees of freedom, Nature Communications 7 (1) (2016) 10929. doi:10.1038/ncomms10929.

[16] E. T. Filipov, T. Tachi, G. H. Paulino, D. A. Weitz, Origami tubes assembled into stiff, yet reconfigurable structures and metamaterials, Proceedings of the National Academy of Sciences of the United States of America 112 (40) (2015) 12321–12326. doi:10.1073/pnas.1509465112.

[17] H. Yasuda, B. Gopalarethinam, T. Kunimine, T. Tachi, J. Yang, Origami-Based Cellular Structures with In Situ Transition between Collapsible and Load-Bearing Configurations, Advanced Engineering Materials 21 (12) (2019) 1900562.

[18] H. Fang, S.-C. A. Chu, Y. Xia, K.-W. Wang, Programmable Self-Locking Origami Mechanical Metamaterials, Advanced Materials 30 (15) (2018) 1706311. doi:10.1002/adma.201706311.

[19] Z. Liu, H. Fang, J. Xu, K. W. Wang, A novel origami mechanical metamaterial based on Miura-variant designs: exceptional multistability and shape reconfigurability, Smart Materials and Structures 30 (8) (2021) 085029. doi:10.1088/1361-665X/AC0D0F.

[20] K. Miura, H. Furuya, K. Suzuki, Variable geometry truss and its application to deployable truss and space crane arm, Acta Astronautica 12 (1985) 599–607. doi:10.1016/0094-5765(85)90131-6.

[21] Y. Tsuda, O. Mori, R. Funase, H. Sawada, T. Yamamoto, T. Saiki, T. Endo, K. Yonekura, H. Hoshino, J. Kawaguchi, Achievement of ikaros-japanese deep space solar sail demonstration mission, Acta Astronautica 82 (2013) 183–188. doi:10.1016/j.actaastro.2012.03.032.

[22] M. Arya, D. Webb, S. C. Bradford, L. Adams, V. Ćormarković, G. Wang, M. Mobrem, K. Neff, N. Beidleman, J. D. Stienmier, G. Freebury, K. Medina, D. Hepper, D. Turse, G. Antoun, C. Rupp, L. Hoffman, Origami-inspired optical shield for a starshade inner disk testbed: Design, fabrication, and analysis, AIAA Scitech 2021 Forum (2021) 1–16doi:10.2514/6.2021-0904.

[23] K. Kuribayashi, K. Tsuchiya, Z. You, D. Tomus, M. Umemoto, T. Ito, M. Sasaki, Self-deployable origami stent grafts as a biomedical application of ni-rich tini shape memory alloy foil, Materials Science and Engineering: A 419 (1) (2006) 131–137. doi:https://doi.org/10.1016/j.msea.2005.12.016.

[24] Z. Song, T. Ma, R. Tang, Q. Cheng, X. Wang, D. Krishnaraju, R. Panat, C. Chan, H. Yu, H. Jiang, Origami lithium-ion batteries, Nature communications 5, funding Information: The work was supported by seed funding from the Fulton Schools of Engineering at Arizona State University. H.J. acknowledges the support from NSF CMMI-1067947 and CMMI-1162619. (Jan. 2014). doi:10.1038/ncomms4140.

[25] T. Tachi, Introduction to Structural Origami, Journal of the International Association for Shell and Spatial Structures 60 (1) (2019) 7–18. doi:10.20898/j.iass.2019.199.004.

[26] L. R. Meza, A. J. Zelhofer, N. Clarke, A. J. Mateos, D. M. Kochmann, J. R. Greer, Resilient 3D hierarchical architected metamaterials, Proceedings of the National Academy of Sciences of the United States of America 112 (37) (2015) 11502–11507. doi:10.1073/pnas.1509120112.

[27] S. Janbaz, N. Noordzij, D. S. Widyaratih, C. W. Hagen, L. E. Fratila-Apachitei, A. A. Zadpoor, Origami lattices with free-form surface ornaments, Science Advances 3 (11) (2017). doi:10.1126/sciadv.aao1595.

[28] D. Melancon, B. Gorissen, C. J. García-Mora, C. Hoberman, K. Bertoldi, Multistable inflatable origami structures at the metre scale, Nature 592 (7855) (2021) 545–550. doi:10.1038/s41586-021-03407-4.

[29] T. Tachi, Designing freeform origami tessellations by generalizing resch's patterns, Journal of Mechanical Design, Transactions of the ASME 135 (11) (2013) 1–10. doi:10.1115/1.4025389.

[30] Y. Yu, Y. Chen, G. Paulino, Programming curvatures by unfolding of the triangular resch pattern, International Journal of Mechanical Sciences 238 (2022) 107861. doi:10.1016/j.ijmecsci.2022.107861.

[31] J. L. Silverberg, A. A. Evans, L. McLeod, R. C. Hayward, T. Hull, C. D. Santangelo, I. Cohen, Using origami design principles to fold reprogrammable mechanical metamaterials, Science 345 (6197) (2014) 647–650. doi:10.1126/science.1252876.

[32] E. T. Filipov, G. H. Paulino, T. Tachi, Origami tubes with reconfigurable polygonal cross-sections, Proceedings of the Royal Society A: Mathematical, Physical and Engineering Sciences 472 (2016). doi:10.1098/rspa.2015.0607.

[33] M. Schenk, S. D. Guest, Geometry of Miura-folded metamaterials, Proceedings of the National Academy of Sciences of the United States of America 110 (9) (2013) 3276–3281. doi:10.1073/pnas.1217998110.

[34] K. Yamaguchi, Y. Miyazawa, H. Yasuda, Y. Song, S. Shimokawa, U. Gandhi, J. Yang, Post-fabrication tuning of origami-inspired mechanical metamaterials based on tachimiura polyhedron, Materials & Design 233 (2023) 112170. doi:10.1016/j.matdes.2023.112170.

[35] D. Rus, M. T. Tolley, Design, fabrication and control of origami robots, Nature Reviews Materials 3 (6) (2018) 101–112. doi:10.1038/s41578-018-0009-8.

[36] E. Hawkes, B. An, N. M. Benbernou, H. Tanaka, S. Kim, E. D. Demaine, D. Rus, R. J. Wood, R. J. W. Designed, Programmable matter by folding, PNAS 107 (2010) 12441–12445. doi:10.1073/pnas.0914069107/-/DCSupplemental.

[37] S. Wu, Q. Ze, J. Dai, N. Udipi, G. H. Paulino, R. Zhao, Stretchable origami robotic arm with omnidirectional bending and twisting, Proceedings of the National Academy of Sciences of the United States of America 118 (36) (2021).

[38] S. Miyashita, S. Guitron, K. Yoshida, S. Li, D. D. Damian, D. Rus, Ingestible, controllable, and degradable origami robot for patching stomach wounds, in: 2016 IEEE International Conference on Robotics and Automation (ICRA), 2016, pp. 909–916. doi:10.1109/ICRA.2016.7487222.

[39] S. Miyashita, S. Guitron, S. Li, D. Rus, Robotic metamorphosis by origami exoskeletons, Sci. Robot 2 (2017) 27. doi:https://doi.org/10.1126/scirobotics.aao4369.

[40] W. Yan, S. Li, M. Deguchi, Z. Zheng, D. Rus, A. Mehta, Origami-based integration of robots that sense, decide, and respond, Nature Communications 14 (12 2023). doi:10.1038/s41467-023-37158-9.

[41] K. Johnson, V. Arroyos, A. Ferran, R. Villanueva, D. Yin, T. Elberier, A. Aliseda, S. Fuller, V. Iyer, S. Gollakota, Solar-powered shape-changing origami microfliers, Science Robotics 8 (9 2023). doi:10.1126/scirobotics.adg4276.

[42] D. Lamoureux, J. Fillion, S. Ramananarivo, F. P. Gosselin, D. Melancon, Kirigami-inspired parachutes with programmable reconfiguration, Nature 646 (8083) (2025) 88–94. doi:10.1038/s41586-025-09515-9.

[43] T. Tachi, K. Miura, Rigid-foldable cylinders and cells, Journal of the International Association for Shell and Spatial Structures 53 (174) (2012) 217–226.

[44] H. Yasuda, J. Yang, Reentrant Origami-Based Metamaterials with Negative Poisson's Ratio and Bistability, Physical Review Letters 114 (18) (2015) 185502.

[45] M. Mesbahi, M. Egerstedt, Graph Theoretic Methods in Multiagent Networks., Vol. 33 of Princeton Series in Applied Mathematics, Princeton University Press / DeGruyter, 2010.

[46] N. Deo, Graph Theory with Applications to Engineering and Computer Science (Prentice Hall Series in Automatic Computation), Prentice-Hall, Inc., USA, 1974.

[47] A. A. Canutescu, A. A. Shelenkov, R. L. Dunbrack, A graph-theory algorithm for rapid protein side-chain prediction, Protein Science 12 (9) (2003) 2001–2014. doi:10.1110/ps.03154503.

[48] K. Xu, W. Hu, J. Leskovec, S. Jegelka, How powerful are graph neural networks?, in: International Conference on Learning Representations, 2019.

[49] J. O'Neil, M. Salviato, J. Yang, Energy absorption behavior of filament wound cfrp origami tubes pre-folded in kresling pattern, Composite Structures 304 (1 2023). doi:10.1016/j.compstruct.2022.116376.

[50] H. Yasuda, K. Yamaguchi, Y. Miyazawa, R. Wiebe, J. R. Raney, J. Yang, Data-driven prediction and analysis of chaotic origami dynamics, Communications Physics 3 (2020) 1–8. doi:10.1038/s42005-020-00431-0.

[51] P. Bhovad, S. Li, Physical reservoir computing with origami and its application to robotic crawling, Scientific Reports 11 (1) (2021) 1–18. doi:10.1038/s41598-021-92257-1.

[52] S. Li, Y. Miyazawa, K. Yamaguchi, P. G. Kevrekidis, J. Yang, Geometry-informed dynamic mode decomposition in kresling origami dynamics, Extreme Mechanics Letters (2023) 102082doi:10.1016/j.eml.2023.102082.

[53] K. Liu, G. H. Paulino, Merlin: A matlab implementation to capture highly nonlinear behavior of non-rigid origami, Proceedings of IASS Annual Symposia 2016 (2016) 1–10.

[54] E. T. Filipov, K. Liu, T. Tachi, M. Schenk, G. H. Paulino, Bar and hinge models for scalable analysis of origami, International Journal of Solids and Structures 124 (2017) 26–45. doi:10.1016/j.ijsolstr.2017.05.028.

[55] S. L. Brunton, J. N. Kutz, Data-Driven Science and Engineering: Machine Learning, Dynamical Systems, and Control, 2nd Edition, Cambridge University Press, 2022. doi:10.1017/9781009089517.

[56] H. M. Kolken, S. Janbaz, S. M. Leeflang, K. Lietaert, H. H. Weinans, A. A. Zadpoor, Rationally designed meta-implants: A combination of auxetic and conventional meta-biomaterials, Materials Horizons 5 (1) (2018) 28–35. doi:10.1039/c7mh00699c.

[57] B. Haghpanah, L. Salari-Sharif, P. Pourrajab, J. Hopkins, L. Valdevit, Multistable Shape-Reconfigurable Architected Materials, Advanced Materials 28 (36) (2016) 7915–7920. doi:10.1002/adma.201601650.

[58] M. Ye, L. Gao, H. Li, A design framework for gradually stiffer mechanical metamaterial induced by negative Poisson's ratio property, Materials and Design 192 (jul 2020). doi:10.1016/j.matdes.2020.108751.

[59] N. Arkus, V. N. Manoharan, M. P. Brenner, Deriving finite sphere packings, SIAM Journal on Discrete Mathematics 25 (4) (2011) 1860–1901. arXiv:1011.5412, doi:10.1137/100784424.

[60] N. N. Vlassis, R. Ma, W. C. Sun, Geometric deep learning for computational mechanics Part I: Anisotropic Hyperelasticity, Computer Methods in Applied Mechanics and Engineering 371 (2020) 113299. arXiv:2001.04292.

[61] H. Fang, S. Li, M. Thota, K. W. Wang, Origami lattices and folding-induced lattice transformations, Physical Review Research 1 (2) (2019) 023010. doi:10.1103/PhysRevResearch.1.023010.

[62] E. Jin, I. S. Lee, D. Kim, H. Lee, W. D. Jang, M. S. Lah, S. K. Min, W. Choe, Metal-organic framework based on hinged cube tessellation as transformable mechanical metamaterial, Science Advances 5 (5) (2019). doi:10.1126/sciadv.aav4119.

[63] C. Coulais, E. Teomy, K. De Reus, Y. Shokef, M. Van Hecke, Combinatorial design of textured mechanical metamaterials, Nature 535 (7613) (2016) 529–532. arXiv:1608.00625, doi:10.1038/nature18960.

[64] Y. L. He, P. W. Zhang, Z. You, Z. Q. Li, Z. H. Wang, X. F. Shu, Programming mechanical metamaterials using origami tessellations, Composites Science and Technology 189 (mar 2020). doi:10.1016/j.compscitech.2020.108015.

[65] A. A. Evans, J. L. Silverberg, C. D. Santangelo, Lattice mechanics of origami tessellations, Physical Review E 92 (2015) 13205. doi:10.1103/PhysRevE.92.013205.

[66] K. Yamaguchi, H. Yasuda, K. Tsujikawa, T. Kunimine, J. Yang, Graph-theoretic estimation of reconfigurability in origami-based metamaterials, Materials & Design 213 (2021) 110343. doi:10.1016/j.matdes.2021.110343.

[67] Y. Miyazawa, H. Yasuda, H. Kim, J. H. Lynch, K. Tsujikawa, T. Kunimine, J. R. Raney, J. Yang, Heterogeneous origami-architected materials with variable stiffness, Communications Materials 2021 2:1 2 (1) (2021) 1–7. doi:10.1038/s43246-021-00212-4.

[68] S. Tomita, K. Shimanuki, H. Nishigaki, S. Oyama, T. Sasagawa, D. Murai, K. Umemoto, Origami-inspired metamaterials with switchable energy absorption based on bifurcated motions of a tachi-miura polyhedron, Materials and Design 225 (1 2023). doi:10.1016/j.matdes.2022.111497.

[69] M. F. Ashby, Materials Selection in Mechanical Design, Elsevier Science, 2016.

[70] B. Han, K. Qin, B. Yu, B. Wang, Q. Zhang, T. J. Lu, Honeycomb-corrugation hybrid as a novel sandwich core for significantly enhanced compressive performance, Materials and Design 93 (2016) 271–282. doi:10.1016/j.matdes.2015.12.158.

[71] D. Naritomi, N. Hosoya, G. Ando, S. Maeda, H. Shigemune, Creation of origami-inspired honeycomb structure using self-folding paper, Materials & Design 223 (2022) 111146. doi:10.1016/J.MATDES.2022.111146.

[72] R. Ma, M. Li, Y. Xu, M. Meloni, J. Feng, J. Cai, Thin-Walled Structures Geometry design and in-plane compression performance of novel origami honeycomb material,

Thin-Walled Structures 181 (September) (2022) 110111. doi:10.1016/j.tws.2022.110111.

[73] M. T. Tolley, S. M. Felton, S. Miyashita, D. Aukes, D. Rus, R. J. Wood, Self-folding origami: Shape memory composites activated by uniform heating, Smart Materials and Structures 23 (9) (2014). doi:10.1088/0964-1726/23/9/094006.

[74] B. Sargent, N. Brown, B. D. Jensen, S. P. Magleby, W. G. Pitt, L. L. Howell, Heat set creases in polyethylene terephthalate (PET) sheets to enable origami-based applications, Smart Materials and Structures 28 (11) (2019). doi:10.1088/1361-665X/ab49df.

[75] M. A. Bessa, R. Bostanabad, Z. Liu, A. Hu, D. W. Apley, C. Brinson, W. Chen, W. K. Liu, A framework for data-driven analysis of materials under uncertainty: Countering the curse of dimensionality, Computer Methods in Applied Mechanics and Engineering 320 (2017) 633–667. doi:10.1016/j.cma.2017.03.037.

[76] M. A. Bessa, P. Glowacki, M. Houlder, Bayesian machine learning in metamaterial design: Fragile becomes supercompressible, Advanced Materials 31 (2019) 1904845. doi:10.1002/adma.201904845.

[77] K. Liu, G. H. Paulino, Nonlinear mechanics of non-rigid origami: An efficient computational approach, Proceedings of the Royal Society A: Mathematical, Physical and Engineering Sciences 473 (2017). doi:10.1098/rspa.2017.0348.

[78] S. Dong, X. Zhao, Y. Yu, Dynamic unfolding process of origami tessellations, International Journal of Solids and Structures 226-227 (2021). doi:10.1016/j.ijsolstr.2021.111075.

[79] K. Liu, G. H. Paulino, Highly efficient nonlinear structural analysis of origami assemblages using the merlin2 software, in: Origami 7, 2018, pp. 1167–1182.

[80] V. Tzoumas, M. A. Rahimian, G. J. Pappas, A. Jadbabaie, Minimal actuator placement with bounds on control effort, IEEE Transactions on Control of Network Systems 3 (2016) 67–78. doi:10.1109/TCNS.2015.2444031.

[81] J. P. Hespanha, Linear systems theory, 2nd Edition, Princeton University Press, Princeton, NJ, 2018.

[82] H. L. Trentelman, A. A. Stoorvogel, M. Hautus, Control theory for linear systems, Communications and Control Engineering, Springer, London, England, 2012.

[83] R. Gupta, W. Zhao, R. K. Kapania, Controllability gramian as control design objective in aircraft structural design optimization, AIAA Journal 58 (2020) 3199–3220. doi:10.2514/1.J059102.

[84] S. Alizadeh, M. Pósfai, A. Ghasemi, Input node placement restricting the longest control chain in controllability of complex networks, Scientific Reports 13 (1) (2023) 3752. doi:10.1038/s41598-023-30810-w.

[85] J. O. Jacobsen, G. Chen, L. L. Howell, S. P. Magleby, Lamina emergent torsional (let) joint, Mechanism and Machine Theory 44 (2009) 2098–2109. doi:10.1016/j.mechmachtheory.2009.05.015.

[86] G. Chen, S. P. Magleby, L. L. Howell, Membrane-enhanced lamina emergent torsional joints for surrogate folds, Journal of Mechanical Design 140 (6 2018). doi:10.1115/1.4039852.

[87] Y. Miyazawa, H. Yasuda, J. Yang, Design of compliant mechanisms for origami metamaterials, Acta Mechanica Sinica/Lixue Xuebao 39 (7 2023). doi:10.1007/s10409-023-23169-x.

[88] K. Yamaguchi, S. Jeong, Y. Miyazawa, Y. B. Oh, R. Dai, M. Mesbahi, J. Yang, Controllability analysis of origami dynamics via state-space modeling, Materials & Design (2025) 114771doi:10.1016/j.matdes.2025.114771.

[89] K. Liu, R. Sun, C. Daraio, Growth rules for irregular architected materials with programmable properties, Science 377 (2022) 975–981. doi:10.1126/science.abn1459.